Folia Histochemica et Cytobiologica

VM
VIA MEDICA

Folia Histochemica et Cytobiologica

Official Journal of the Polish Society for Histochemistry and Cytochemistry

POLISH SOCIETY FOR HISTOCHEMISTRY AND CYTOCHEMISTRY STATEMENT OF FOLIA HISTOCHEMICA ET CYTOBIOLOGICA EDITORIAL POLICY

Folia Histochemica et Cytobiologica is an international, English-language journal devoted to the rapidly developing fields of histochemistry, cytochemistry, cell and tissue biology.

The Folia Histochemica et Cytobiologica publishes papers that meet the needs and intellectual interests of medical professionals, basic scientists, college and university teachers and students. Prospective authors should read most recent issues of FHC to determine the appropriateness of a possible contribution. However, such an examination does not provide an infallible guide because editorial policy is always under review. Technical correctness is necessary, but it is not the only condition for acceptance. Clarity of exposition and potential interest of the readers are important considerations; it is the reader, not the author, who must receive the benefit of the doubt.

Folia Histochemica et Cytobiologica publishes review articles, original articles, short communications and proceedings of scientific congresses/symposia. Fields of particular interests include development and application of modern techniques in histochemistry and cell biology, cell biology and pathology, cell-microenvironment interactions, tissue organization and pathology.

Manuscripts announcing new theoretical or experimental results, or manuscripts questioning well-established and successful theories, are highly desirable and are a subject for evaluation by specialists. Manuscripts describing original research that clarifies past misunderstandings or allows a broader view of a subject are acceptable. Manuscripts that demonstrate new relations between apparently unrelated areas of fields of interests are appropriate. Manuscripts that show new ways of understanding, demonstrating, or deriving familiar results are also acceptable. Such manuscripts must provide some original cytobiological insight and not just a clever derivation.

Regularly, review or tutorial articles are published, often of a length greater than that of the average article. Most of these articles are a subject of a review; authors planning such articles are asked to consult with the editors at an early stage.

Most readers of a particular article will be specialists in the subject matter presented; the context within which the paper is presented should be established in the order given in Instructions for Authors. Manuscripts must be technically correct and must take proper cognizance of previous work on the same subject regardless of where it may have appeared. Such referencing is especially important for reminders of once well known ideas, proofs, or techniques that may have again become useful to readers. It is the responsibility of the author to provide adequate references; editors and referees will not do the literature search that should have been done by the authors. The references are a matter of review though.

Contributions considered include: Regular Articles (Papers), Short Communications, Review Articles, Conference Proceeding, Book Reviews and Technical Notes, which describe new laboratory methods or substantial improvements of the existing techniques. Regular articles should be about five journal pages or less in length. Short communications are usually confined to the discussion of a single concept and should be about two journal pages in length. Review articles are confined to a broad discussion and should contain the most recent knowledge about the subject.

Instructions concerning the preparation of manuscripts are given in the Information for Authors. Care in following those instructions will permit editors and referees to devote more time to thoughtful evaluation of contributions and will ultimately lead to a better, more interesting Journal.

Copying information, in part or in whole by any means is prohibited without a written permission from the owner.

Illustration on the cover: *Macrophages in the lidney of lupus-prone NZB/W mouse were identified by F4/80 immunohistochemical staining* (see: Yaling Xu and Han Li, pp. 110–121).

23-0690.002.001

Folia Histochemica et Cytobiologica

Official Journal of the Polish Society for Histochemistry and Cytochemistry

ORIGINAL PAPER

VM
VIA MEDICA

Digital morphology network for effective teaching of cytology, histology and histopathology for medical and biology curriculum. VM3.0 Erasmus+ project

Cornelia Amalinei[1] , Andrei Daniel Timofte[1], Irina Draga Căruntu[1] ,
Piotr M. Wierzbicki[2], Michał A. Żmijewski[2], Spiros Sirmakessis[3], Jose L. Girela[4],
Noemí Martínez-Ruiz[4], M. Flores Vizcaya-Moreno[4], Rosa M. Pérez-Cañaveras[4],
Zdravka Harizanova[5], Ferihan Popova[5], Cintia Colibaba[6], Zbigniew Kmieć[2]

[1]Department of Morphofunctional Sciences I — Histology, Grigore T. Popa University of Medicine and Pharmacy, Iași, Romania

[2]Department of Histology, Medical University of Gdansk, Gdansk, Poland

[3]Electrical and Computer Engineering Department, University of Peloponnese, Patras, Greece

[4]Department of Biotechnology and Department of Nursing, University of Alicante, Alicante, Spain

[5]Department of Anatomy, Histology and Embryology, Faculty of Medicine, Medical University of Plovdiv, Plovdiv, Bulgaria

[6]Iași University of Life Sciences and Fundatia EuroEd, Romania

Abstract

Introduction. Digital microscopy transformation, the basis for the virtual microscopy applications, is a challenge but also a requirement in modern Medical Education. This paper presents the scope, background, methods, and results of the project "Digital Transformation of Histology and Histopathology by Virtual Microscopy (VM) for an Innovative Medical School Curriculum", VM3.0, funded by the European Union under the Erasmus+ framework (ref.no.2022-1-RO01-KA220-HED-000089017). The project was initiated at Grigore T. Popa University of Medicine and Pharmacy, Iași, Romania, with the support of Euroed Foundation, Iași, and cooperation of University partners from Gdansk (Poland), Plovdiv (Bulgaria), Alicante (Spain), and Patras (Greece) aimed to implement digital histology and histopathology teaching in a common network.

Materials and methods. The backbone of the project was the development of a Digital Slide Platform based on the scans of histological slides collected from all the partners of the participating universities and the creation of a simple and fast digital/internet communication tool that could be used to improve histology and histopathology teaching of medical and natural sciences students. The construction of a Virtual Microscopy Library (VML) has been based on the acquisition of whole scans of high-quality histological slides stained by hematoxylin and eosin (H&E) and other classical staining methods and description of various organs' details in English as well as respective languages of the project's partners. The VML can be used for different approches, both for students' instruction in classes as well as for individual students' work and self-testing. Universities from other countries could use the modal structure of the developed VML system on the condition that more slides are provided and the implementation of national language(s) is implemented.

Correspondence address:

Prof. Cornelia Amalinei, MD, PhD.
Department of Morphofunctional Sciences I — Histology
Grigore T. Popa University of Medicine and Pharmacy
16 Universitatii Street, Iași 700115, Romania
e-mail: cornelia.amalinei@umfiasi.ro, tel. +40740072376

Conclusions. The combined efforts of all university partners allowed to establish the dynamic low-cost virtual microscopy educational system. The VM system could help unify the standards of cytology, histology, and histopathology teaching in a quest for the digital transformation of the European educational system. *(Folia Histochem Cytobiol 2024, Vol. 62, No. 2, 61–67)*

Keywords: virtual microscopy; histology; slide library; teaching; self-testing; files-sharing platform; histopathology

INTRODUCTION

The role of histology and histopathology in medical studies

Histology is a core discipline in medical studies. It is present in the structure of the degrees in medicine all over Europe and in the rest of the world as a basic subject to be taken in the first or second year of the medical curriculum. Histology allows medical students to study the microscopic structure of tissues and organs. It provides a foundation for understanding the normal organization and function of cells, tissues, and organs in the human body. This knowledge is essential for accurately diagnosing diseases and interpreting clinical findings. It helps students correlate the anatomical features they learn in gross anatomy with the cellular composition and organization of tissues. Moreover, histology serves as a basis for research in various medical fields. It enables scientists to investigate the cellular and molecular mechanisms of underlying diseases, develop new treatment modalities, and advance medical knowledge. Histological techniques, including immunohistochemistry and molecular histology, are vital tools in biomedical research.

Regarding histopathology, it is usually a mandatory subject on the third or fourth year of the medical studies. Histopathology is instrumental in recognizing and diagnosing various diseases. By studying abnormal tissue structures, such as cellular changes, inflammation, or tumor formation, medical students can identify pathological conditions and understand the underlying mechanisms. This knowledge is crucial for diagnosing diseases and planning appropriate treatment strategies.

Virtual microscopy in histology and histopathology teaching

Virtual microscopy in histology teaching refers to the use of digital technology to replicate the experience obtained by means of a traditional microscope for educational purposes. It involves the acquisition of high-resolution images of histological slides and making them accessible by the use of a computer or other digital devices.

With virtual microscopy, students can view and explore histological slides at their convenience without the need for physical microscopes or glass slides. These digital slides can be accessed *via* specialized software or online platforms designed for histology education.

Virtual microscopy offers specific benefits in histology teaching, with several advantages listed below.

- **Accessibility.** Virtual microscopy allows students to access a wide range of histological slides from anywhere and at any time, as long as they have an internet connection. It eliminates the need for physical slides and microscopes, making it more convenient for both students and educators.
- **Enhanced learning experience.** Digital slides offer high-resolution images that can be zoomed in or out, providing students with detailed views of cellular structures. This enhances their ability to identify and understand histological features, improving their overall learning experience.
- **Interactivity.** Virtual microscopy platforms often provide interactive features, such as annotations, labels, and pointers that help students focus on specific structures or areas of interest. They can also include additional educational resources like audio/video explanations or quizzes to further engage students in the learning process.
- **Collaboration.** Digital slides can be easily shared and accessed by multiple students simultaneously. This allows for collaborative learning and discussion, as students can annotate slides, share their observations, and engage in virtual discussions with peers and instructors.
- **Preservation of slides.** Physical histological slides are prone to damage, loss, or deterioration over time. Virtual microscopy eliminates these concerns by digitizing the slides, ensuring their long-term preservation and availability for future reference.

Overall, VM in histology teaching offers a versatile and efficient way to engage students in the study of cellular structures and tissue morphology. It provides an interactive and accessible platform that enhances learning, collaboration, and the overall educational experience in the field of histology.

Virtual microscopy tools

The key to a better educational process in modern times is always to embrace new technologies as educational tools. Virtual microscopy is one such advanced and innovative educational tool, particularly in teaching.

The concept of virtual microscopy emerged relatively recently, in 1997, when it was first described by the Computer Science Department at the University of Maryland and the Pathology Department at Johns Hopkins Hospital in Baltimore, Maryland [1]. Since then, a wide array of systems has been developed, and they can be broadly categorized into two groups: monitored microscopes and scanners. The partners of the VM3.0 project utilize both, with a particular focus on digital slide scanners.

The necessity for developing a European digital virtual microscopy network to improve histology and histopathology teaching for medical and health sciences curricula

In the context of worldwide digitalization, the universities participating in the European Union (EU) Erasmus+ project "Digital Transformation of Histology and Histopathology by Virtual Microscopy (VM) for an Innovative Medical School Curriculum", VM3.0, funded by the European Union under the Erasmus+ framework (ref.no.2022-1-RO01-KA220-HED-000089017) realized that the development of a Virtual Microscopy Platform would be a helpful element to improve the learning process for histology students. The development of a European digital microscopy network, with the participation of all higher education institutions from the involved five countries, is necessary to revolutionize the European medical curricula, leading to digital transformation through the development of digital readiness, resilience, and capacity. The use of VM library platforms may increase the undergraduate and postgraduate students' vocational skills for new, modern medicine and health sciences domains. Moreover, the digitalization of microscopy teaching addresses the students' interest in new technologies and methods. Furthermore, VM libraries may be used as alternative or additional didactic tools, complementary to traditional microscopy teaching. The VM3.0 Erasmus+ project has been actually developed to establish a dynamic VM educational system in response to the increasing pressure for digital transformation of the educational systems of the participating universities and countries.

The partners of the VM3.0 Erasmus+ project

The University of Medicine and Pharmacy "Grigore T. Popa", (UMFIASI), located in Iași, Romania (https://www.umfiasi.ro/en), is a student-centered university that provides high quality education, develops high-class research that supports learning, and keeps strong international contacts. UMFIASI is the second oldest and largest public medical university in Romania with four faculties, over 926 academic staff and more than 9,900 students. Research activities are carried out in all university departments, financial support being mostly provided through grants or research contracts. The university operates with two centers of excellence, eight research centers, and two research platforms.

Since 2009, the University has implemented 30 national and European projects apart from being a partner in the Erasmus mobility programs, having bilateral agreements with many European universities.

The Medical University of Gdańsk, (MUG), (https://mug.edu.pl) is the largest medical university in northern Poland. The MUG was awarded an eighth place in the prestigious national Excellence Initiative — Research University competition of the best 10 Polish universities. More than 6000 undergraduate and postgraduate students at four faculties (Medicine, Pharmacy, Public Health, and Biotechnology, the last one together with the University of Gdańsk) are being taught by 1,216 full-employed academic staff. MUG also offers programs in English such as Premedical Course, Medicine Doctor, Pharmacy and Nursing. International students constitute more than 15% of the MUG's students and represent more than half of all international students in Gdańsk.

MUG has participated in Erasmus+, Key Action 2 project during 2014–2020 (project "CLILMED") and also in Erasmus Mundus Joint Masters project in current EU Program 2021–2027 (Project "Sustainability, drug discovery, Erasmus Mundus Joint Master — S-DISCO"), and, currently, in the VM3.0 Erasmus+ project that is subject of this special article.

The Medical University — Plovdiv, (MUP), (https://mu-plovdiv.bg/en) provides training of students in Medicine, Dental Medicine, Pharmacy, and Public Health as well as postgraduate training of PhD students and specializing medical professionals in Medical College of the University. MUP provides high quality education for almost 6,000 students from all over Europe, with international students comprising 2/3 of all students. The staff of MUP consists of 865 academics including 205 professors and associate professors. The study curricula are closely connected with the introduction of e-learning and interactive methods in the training process.

The Medical University Plovdiv has been awarded first place in the category "medicine" among the medical universities in Bulgaria twice and took second place in the top Research Universities in Bulgaria. Clinical training is conducted in six university hospitals. Medical Simulation Training Center presents the highest state-of-the-art medical training center recognized by

American College of Surgeons as a "Comprehensive Education Institute". MU-Plovdiv is a member of the European University Association with more than 150 academic bilateral and international agreements with universities from both European Union and non-EU countries. The MU-Plovdiv is certified as meeting the requirements of ISO9001:2015 in educational activities.

The University of Alicante, (UA), (https://www.ua.es/en/index.html) was created in 1979. Today, it educates and trains more than 36,000 students, including 3000 international students, and offers more than 80 undergraduate and 96 postgraduate programs, making it one of the fastest-growing universities in Spain. The UA houses 227 research groups and employs over 2,400 academic staff.

The UA makes an important commitment to using new technologies in teaching-learning processes. Specifically, an effort has been made to bring the digital, online and virtual approach to different educational methods, which allows a more efficient use of available resources while reducing barriers to access higher education. In this regard, transnational partnership in the VM3.0 Erasmus+ program provided an opportunity to standardize the curricula in histology and histopathology.

The University of Alicante is firmly interlinked with its socio-economic environment and is considered a point of reference for many companies, providing to them technical assistance, student training programs, and continuous post-graduation education. The UA participates, as a partner or coordinator, in a large number of research cooperation projects from different funding programs.

The UA has been included in many programs as a strategic and core partner. Its Faculty of Health Sciences, especially well-known in Spain for its Nursing Department, has been evaluated as one of the most productive faculties regarding healthcare research in Spain, being always in the top three faculty rankings in the Spanish Education Quality assessment program.

The University of Peloponnese, (UP), (https://uop.gr/en) was established in 2000 and accepted its first students in 2002. The University of Peloponnese central premises are located in Tripolis, while schools and departments operate in five other cities (Corinth, Nafplion, Sparti, Kalamata, and Patra) throughout the Peloponnese and Western Greece Region. Altogether approximately 20,000 students study in five major schools.

The Department of Electrical and Computer Engineering (ECE) belongs to the School of Engineering based in Patra. The curriculum offers a basic education of six academic semesters, followed by four academic semesters, in which students specialize in four Electrical and Computer Engineering programs. In the second cycle of studies, ECE offers a Postgraduate Program entitled "Smart Information and Communication Technologies and Services". ECE is strongly involved in research and innovation and actively participates in national and international projects (funding from Horizon 2020, Erasmus+, and others). ECE is staffed by thirty members of teaching research staff and six members of technical laboratory personnel on the permanent employment basis. ECE makes a special effort to warrant the European/international scientific and/or professional perspective for the graduates, through the implementation of the ECTS score system, the participation in Erasmus+ programs, and other forms of academic and research exchanges through bilateral agreements with countries that excel in engineering studies.

EuroEd Foundation (https://euroed.ro) is a non-profit organization located in Iași, Romania, that commenced its activity in 1992.

EuroEd's relevant experience lies with coordinating and participating in EU funded projects, as well as in strategies and methodologies of co-operation at local, regional, national and trans-national levels. From 1998, EuroEd Foundation coordinated and implemented over 100 national and international educational projects in various fields, including medicine. EuroEd projects have been awarded European distinctions of the highest level, such as 10 international awards in the last five years for the quality of its projects: eight European Label Awards and a Worldaware distinction.

EuroEd has also gained experience from the implementation of related projects. They included VOICE — vocational education and training for speech and language therapists and parents for rehabilitation of children with cochlear implant (VOICE) how to speak, Tiramisu — First Aid Improve Survival, HOPE — How Oncogenetics Predicts & Educates, ZoonosesOnlineEducation, online courses with videos for the field of veterinary communication dealing with prevention, diagnosis and treatment of diseases transferable from animals to humans, and Palliative Care MOOC — Massive open online courses with videos for palliative clinical communication.

Aims of the VM3.0 Erasmus+ project

Light microscopy sharing examination, in which the educator stands close by the student and alternatively examines the slides, using the same microscope to analyse each tissue/cell/organ, has represented traditional microscopy education. This method has been challenged during the COVID-19 pandemic and has forced innovation as to continue teaching

microscopy. Consequently, teaching *via* VM seemed an optimal alternative for histology and histopathology education. Whole Slide Imaging (WSI) has emerged as the digital pathology platform of choice for teaching in recent years, demonstrating its utility in both under-graduate and graduate medical education, primarily by leveraging stored teaching libraries, study slide sets, and individual cases to enhance didactic teaching, to monitor the acquisition of new skills (*e.g.*, staining interpretation), and to assess competences through slide examination/testing. Furthermore, VM software reproduces high-quality images with meticulous clarity and added features that allow students and teachers to highlight, annotate, pan the whole specimen and zoom on the specific structures or details. Thus, VM represents a modern tool with increased quality and utility in microscopy education.

Several medical curricula around the world have adopted the VM to complement the effectiveness of competency-based education in medical education. Unfortunately, very few VM teaching possibilities are available in Europe. Therefore, one of the basic aims of the VM3.0 project was to improve students' skills in the acquisition and interpretation of the normal and pathological structures in microscopic slides prepared by the use of the paraffin technique and stained by H&E method. Moreover, a selection of slides stained by other methods was planned to be included in the slides' set to demonstrate to the students the power of microscopy for further differentiating of the cellular and tissue structures.

Another further aim was to prepare a short description of each of the slides in English and the language of the participating universities' to create a basis for common curricula for teaching histology and histopathology. Moreover, a practical guide for students and teachers had to be set up to explain the optimal options for using the VM system.

An important task of the VM3.0 project was to create a fast and low-cost online system for sharing the scanned microscopic slides stored on the VM library platform in a safe but easily accessible way.

Finally, the creation of the VM library is expected to increase the students' understanding of the morphological structures by introducing them to the scans not only during the didactic process at the university but also enable self-learning through online access to the scan library.

Thus, the general didactic VM3.0 project's aim was the improvement in the understanding of microscopic structures as a result of the digital transformation of traditional methods of teaching and learning of histology and histopathology.

MATERIALS AND METHODS

Selection of the microscopic slides

Researchers from participating universities (apart from the University of Peloponnese and EuroEd) had selected more than 250 good-quality slides to be scanned for the preparation of the virtual library. It was assumed that the collection should contain slides representing normal tissues and organs stained mainly by H&E method, as well as approximately 40 slides showing pathological specimens. To ensure technical homogeneity of scanning, the procedure was performed mainly by one person (A.D.T.) at the Departments of Histology and Histopathology of the University of Medicine and Pharmacy "Grigore T. Popa" (Iași, Romania).

The Aperio AT2 Slide Scanner (Leica Biosystems) was used with objective magnification of ×20 and digital scanned slides viewing was accomplished by Aperio ImageScope free software (https://aperio-ima-gescope.software.informer.com). [2, 3].

Strategy for description of slides

It had been decided that, for students' use, each slide should be characterized in a concise way to avoid repetition of exhaustive slides' descriptions present in many histological atlases. Each slide was also associated with three to five keywords along with a specific hyperlink. Additionally, several self-testing multiple--choice questions included into each teaching module may enable students self-learning and self-assessment.

Preparation of practical guide to use the VM system

In order to help users to navigate and use effectively the VM system, a practical guide was proposed. This guide is aimed to contain short videos that offer a comprehensive overview of accessing the system, navigating the interface, using the slide library (searching, filtering results), viewing the slides (opening, panning and zooming), making and managing annotations.

Setting up online network to access the VM slide library from the digital systems of the participating universities
General description of the applied methods

To ensure optimal performance and reliability, the partners at the University of Peloponnese were granted access (S.S.H. with root permissions) to a system hosted by the coordinating partner (UMFIASI) that meets the following specifications: operating system — Linux Debian 12 "bookworm" or Ubuntu; at least 8 GB of RAM, a storing capacity of at least 2 TB;

internet connection. The UP partners remotely installed a range of software and extensions essential to support the application, such as PHP 8.2, Composer, Node.js, MariaDB, Apache2, and also libraries and tools necessary for high-performance image processing tasks, such as libvips42 and libvips-tools.

Setting up this server configuration allowed the establishment of an online network that provided efficient access to the VM slide library from the digital systems of all participating universities.

The procedure of uploading the collection of scanned slides was performed by the same person responsible for the digital scanning process (A.D.T.), ensuring the correct distribution of the digital slide files in the virtual library according to the established curricula.

For each slide, the description with the keywords was uploaded, first in English, verifying the correspondence between the keywords and the fields on the virtual slide.

RESULTS

The preliminary results consisted of an easy, online-accessible digital educational platform designed to assist students and young pathologists in understanding the science of normal and pathological tissue structure and function at the microscopic level.

The virtual platform included:
- a user-friendly interface with a login access menu;
- a search functionality allowing users to quickly find specific slides, topics, or keywords;
- an extensive slide library encompassing 20 teaching modules (sections) with digital slides, providing a wide range of examples for study;
- a tutorial part with step-by-step video tutorials covering instructions for the effective use of the platform;
- detailed and comprehensive descriptions for the collection of slides, including keywords representing histological or histopathological diagnostic criteria;
- slide annotations software module offering the possibility for the user to save his own annotations for the slides;
- a quiz and assessment part composed of multiple answer questions to test users' understanding of the material.

The login access menu (Fig. 1) provides access to the platform for teachers, medical students, and training pathologists using a username and a password, the accessibility being limited to each category as follows: teaching staff is permitted to access, edit, modify, and save different descriptions and annotations visible to every user, whereas student accounts have limited
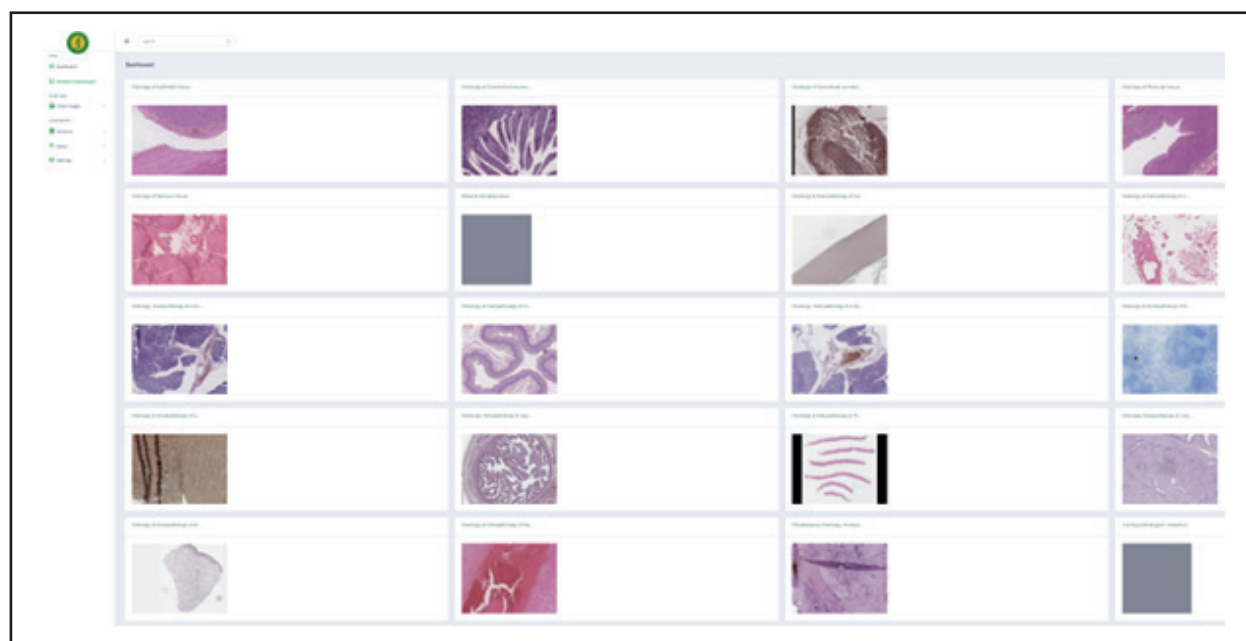
Figure 1. The opening screen of the VM3 platform. After logging in, a screen with a navigation menu is displayed on the left side with the following items: Dashboard — a general interface for the teacher/administrator, containing general data on the number and kinds of users and statistics, and Student's dashboard — a screen for the student/end user. Below are the drop-down menus (Slide images, Sections, Users, Settings). The central section contains photomicrographs of slides with their names. Top right — shortcuts: language selection, light/night mode, full screen, and user shortcut (name/login).

access, simply viewing the slides, making personal annotations, taking notes, and highlighting areas of interest, viewable only under their account.

Using the dashboard menu button, the user can access the virtual slide library, select a slide of interest, navigate on it, and create, save, and share annotations *via* email. The annotation section uses tool buttons to allow the user to highlight areas, to draw different shapes and to add personal notes.

The following Figures will present screenshots that correspond to the subsequent steps in studying slides related to the specific teaching module (section).

The next logical step in the student's work will be a selection of a specific slide from the collection of 298 currently available scanned slides. The screenshot shown in Figure 2 presents a way of finding the slide indicated by the educator by using the "Filter" option. Only the option "View" is accessible to the students, whereas the options "Edit" and "Delete" are available for teachers only, *e.g.,* to correct/add the slide's description or to substitute it with a new, better scanned slide.

The viewing section of the slide is presented in Figure 3. The screenshot demonstrates that the VM3.0 system's options allow smooth panning and zooming, with the possibility of viewing only a full screen by hiding the adjacent slide description.

Types and number of the selected and scanned microscopic slides

The scanned microscopic slides were ordered and classified into respective teaching modules (sections) that correspond to the typical histological classification of tissues and organs. They have been listed in Table 1. The number of slides required in the curriculum were different according to the modules, as shown in Table 1.

An important part of the VM3.0 platform consists of the teaching module associated with each of the histological slides. It includes a concise description of slide's characteristics features with keywords, and hyperlinks to the images that present those features (Table 2). The latter feature represents the basic core of the system since it enables and efficient and fast online connection with the image database.

DISCUSSION

Challenges of medical education in 21st century

Digital histology and pathology implementation in medical education have opened the perspectives for a significant shift in the design of the medical curriculum. Light microscopy sharing examination, in which the teacher stands close to the student and alternatively examines the slides, using the same
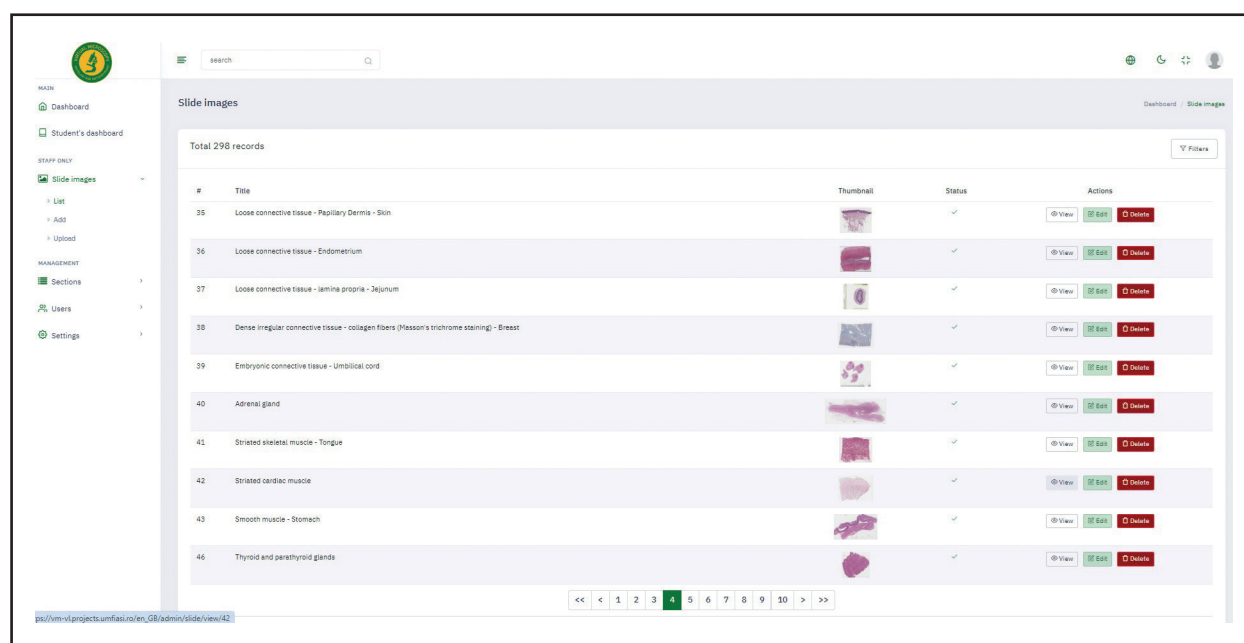
Figure 2. Selecting a histological slide on the VM3 platform. From the "Slide images" drop-down panel on the left side of the screen, the student can select the appropriate slide. The educator/admin can edit (adding, deleting, editing names and descriptions) slides. The main panel contains the slide number, its name, thumbnail, and the option to view it in the same or new window. There are shortcuts for editing (editing, deleting) slides for the educator/admin. There is a filter option at the top allowing you to search the platform by slide or section name.
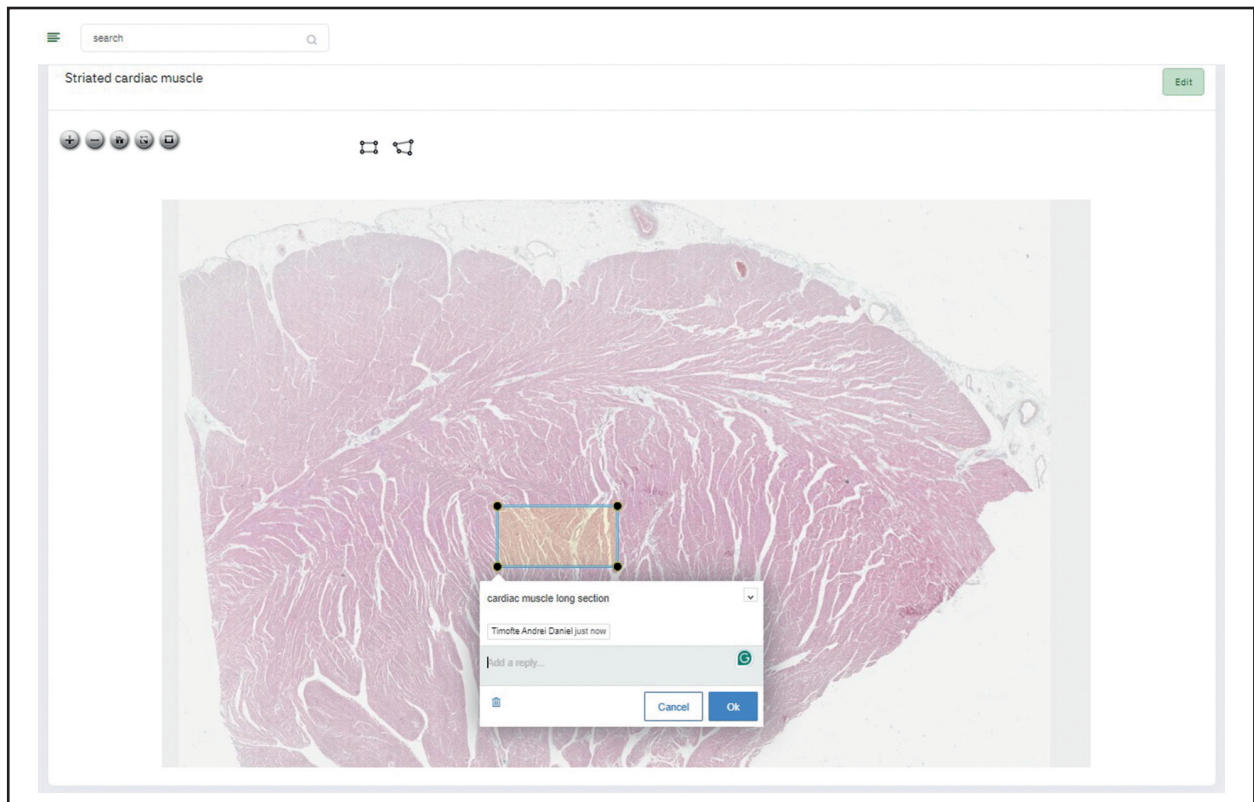
Figure 3. Studying slide image. After selecting the "View" option for a given slide, here, cardiac muscle, a scanned image of the stained histological section appears at the lowest magnification. At the top, there are shortcuts for actions (zoom in, zoom out, home, full screen, and take a screenshot) of the currently viewed part of the slide with an important option of direct saving to the default directory in .png format. Next to the shortcuts, there is an option to outline details in the form of a rectangle or any other shape. Once applied, the user can place a description in this field, which will appear on the screen after clicking on it. As a result, the introduced outline details are saved and stored on the dedicated server so that they can be checked online by teachers.

microscope in order to analyse each tissue/cell/organ, along with tandem microscopic review or "double--scoping" of histology and pathology slides have represented traditional way of microscopy education. However, these methods require a close proximity of educator and students and/or the use of a double- or multi-headed optical light microscope which is not amenable to physical distancing.

Alternatively, a shift toward teaching *via* VM provides a readily available, physically distanced, and cost-conscious alternative for histology and histopathology education. The use of VM has been already demonstrated to enhance student learning and overall performance in a more clinically oriented and dynamic learning environment, being highly accepted and adopted by several medical schools across the globe. Thus, VM can also provide a modality that helps to bridge the gap for students with inadequate clinical exposure.

Digital microscopy also facilitates the integration of advanced image analysis tools. These tools can automatically identify and quantify cellular structures, aiding in more precise and efficient learning and

diagnoses. The ability to annotate slides and share these annotations with peers and instructors promotes better communication and collaborative learning. Additionally, digital storage of slides mitigates the risk of physical degradation over time, preserving valuable specimens indefinitely.

Several Medical Programs around the world have adopted the VM to compliment the effectiveness of competency-based education in medical education. Digital pathology has paved a path to address some of the core competencies and collaborative models in various education and post-graduation programs. Therefore, it is imperative that medical students become familiar and proficient in the VM system applications. Through survey data, the immediate needs of our project have been measured. Existing technology may not be initially optimized for a dynamic virtual experience, resulting in lag time with image movement, problems of focusing, image quality issues, and a narrower field of view; however, these technological barriers can be overcome through hardware and software optimization.

Table 1. The teaching modules of the VM3.0 project's library

Number	Name of teaching module (section)	No. of slides	Number	Name of teaching module (section)	No. of slides
1	Histology of epithelial tissue	29	12	Histology & histopathology of respiratory system	20
2	Histology of connective tissue proper	9	13	Histology & histopathology of urinary system	22
3	Histology of specialized connective tissue	5	14	Histology, histopathology & cytology of female reproductive system	34
4	Histology of muscle tissue	3	15	Histology & histopathology of male reproductive system	13
5	Histology of nervous tissue	2	16	Histology, histopathology & cytology of mammary glands	5
6	Blood & hematopoiesis	2	17	Histology & histopathology of integumentary system	13
7	Histology & histopathology of cardiovascular system	17	18	Histology & histopathology of the nervous system	14
8	Histology & histopathology of immune system	12	19	Miscellaneous histology, histopathology & cytology	5
9	Histology, histopathology & cytology of endocrine system	11	20	Training pathologists' collection	29
10	Histology & histopathology of the oral cavity and digestive tract	25			
11	Histology, histopathology & cytology of glands associated to the oral cavity and digestive tract	29			

Table 2. Example of histology and histopathology slide descriptions on the VM3.0 platform with hyperlinks

Section	Title & slide number	Description	Keywords	Hyperlink to VM3.0 platform
Histology of Muscular Tissue	Striated cardiac muscle, #42	The slide shows a heart section, containing striated cardiac muscle (myocardium), which is composed of branching cardiac muscle cells (cardiomyocytes) with a single centrally placed nucleus for each muscle cell. Each cell end is connected with the ending of an adjacent cardiomyocyte *via* specialized junctions called intercalated disks. They are usually unstained but occasionally appear as thin, dark lines between adjacent cells. Yellow-brown granules of lipofuscin pigment are visualized near the nucleus of some cells.	cardiac myocyte	https://vm-vl.projects.umfiasi.ro/en_GB/app/viewer/42#zoom=38.33759992447474&x=0.42766746903592456&y=0.3344392700574031
			nucleus	https://vm-vl.projects.umfiasi.ro/en_GB/app/viewer/42#zoom=150.91090225563912&x=0.5071168587516031&y=0.13726224150709515
			intercalated disks	https://vm-vl.projects.umfiasi.ro/en_GB/admin/slide/view/42#zoom=75.40820288040075&x=0.5888613961454934&y=0.2782052160790237
			lipofuscin pigment	https://vm-vl.projects.umfiasi.ro/en_GB/app/viewer/42#zoom=150.91090225563912&x=0.5368358999042452&y=0.18239768625390837
			cardiac myocyte	https://vm-vl.projects.umfiasi.ro/en_GB/app/viewer/42#zoom=38.33759992447474&x=0.42766746903592456&y=0.3344392700574031
			nucleus	https://vm-vl.projects.umfiasi.ro/en_GB/app/viewer/42#zoom=150.91090225563912&x=0.5071168587516031&y=0.13726224150709515
Histology, Histopathology & Cytology of Mammary glands	Breast ductal carcinoma, #183	The slide shows breast fibro-adipose tissue containing infiltrative solid nests, cords, or individual tumor cells with moderately enlarged nuclei, with conspicuous nucleoli, eosinophilic cytoplasm, and variable mitoses that compress the prominent desmoplastic stroma. A focus on ductal carcinoma in situ (DCIS) is observed.	infiltrative solid nests	https://vm-vl.projects.umfiasi.ro/en_GB/admin/slide/view/183#zoom=16.07510288065844&x=0.3232073308842591&y=0.41221007964595435
			moderately enlarged nuclei	https://vm-vl.projects.umfiasi.ro/en_GB/admin/slide/view/183#zoom=46.29629629629631&x=0.31692180010959287&y=0.4320062549453528
			desmoplastic stroma	https://vm-vl.projects.umfiasi.ro/en_GB/admin/slide/view/183#zoom=12.920446631187666&x=0.27319972201033654&y=0.5019024278061817
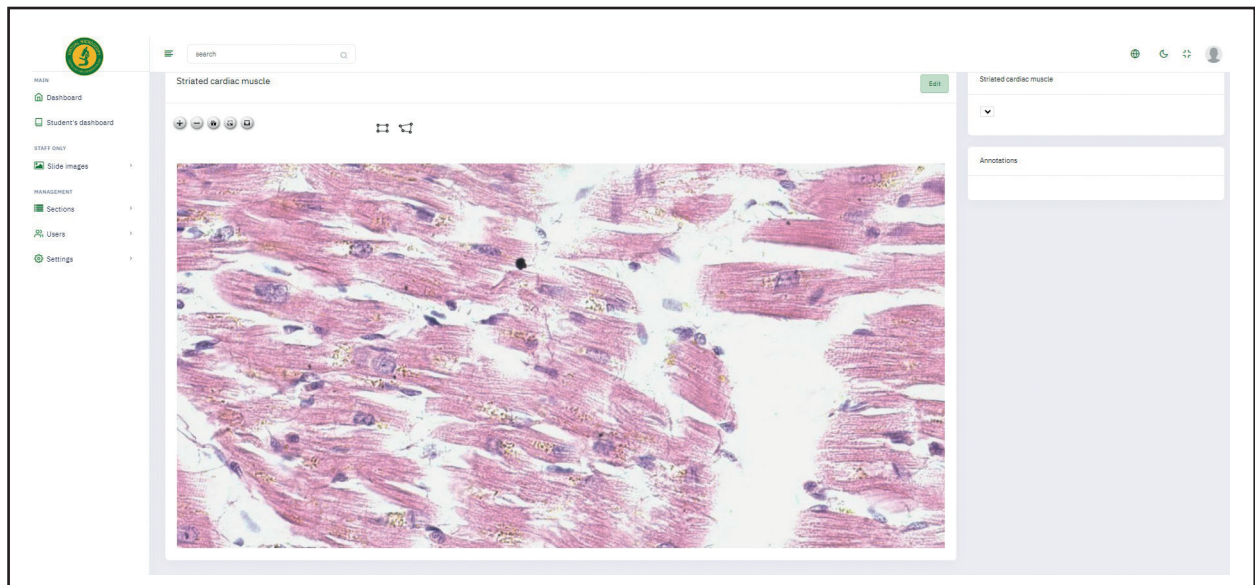
Figure 4. Keywords directly link the specific details of the slide to the corresponding images. This image appears when the user clicks on a hyperlink placed in the slide's characteristics as shown in Table 2 (here, the "intercalated disk" hyperlink from Table 2 https://vm-vl.projects.umfiasi.ro/en_GB/app/viewer/42#zoom=125.7590852130326&x=0.51709664185093&y=0.1801713049046873). The image is centered on the appropriate detail (at the magnification appropriate for the specific detail/area of the slide), without marking by other methods. The image can also be obtained manually by using the zoom-in shortcut or using the mouse wheel.

Mapping research

In the first stage of the project, Mapping research on the current situation of the use of VM in the partner countries was performed. Extensive literature research was conducted as well as contacting 35 histology experts and asking them to complete a questionnaire. Figure 5 shows the increasing interest in the field of VM applied to histology and histopathology teaching.

Regarding the available publications, using the combination of keywords ("virtual" and "microscope" or "microscopy" and "histology"), the authors found 521 papers. After reviewing the list of publications, we selected those that were more closely related to the exact purpose of the project. As a result, Table 3 shows the main characteristics of the 47 articles selected at this stage of the mapping research [4–50].

We found a scarcity of publications related to the use of VM in histology education in international journals. From those published, the main conclusion is that there are no differences in the achievement of learning objectives between students taught histology using VM and those taught using traditional light microscopy in-class approach.

Supplementary Table 1 shows the country distribution of the experts. We asked them to answer a questionnaire related to the use of VM in teaching histology and histopathology (Supplementary Figure 1) Generally, in the opinion of the experts, VM seems to be a desirable teaching method, with more advantages rather than disadvantages. Most responders find that it is necessary to include clear instructions on using the VM platform and quizzes/tests to assess the efficacy of the teaching and learning process. There is also a consensus that a combination of VM and traditional microscopy teaching methods should be employed. The Supplementary Figure 1 presents answers to each of the questions.

Apart from the Likert questions, we asked the experts to provide their opinions on the benefits of using VM in histology teaching in an open format. Supplementary Figure 2 shows a word cloud with the most common terms used.

While virtual microscopy offers many benefits in histology education, it is important to consider some of its drawbacks and potential problems:

- **Lack of haptic feedback:** Virtual microscopy cannot replicate the tactile experience of using a physical microscope. The ability to feel and manipulate the slide, adjust focus, and perceive depth through haptic feedback is lost in the digital environment. This tactile feedback can be valuable in developing fine motor skills and spatial understanding, essential in histological analysis.
- **Limited real-time interaction:** Virtual microscopy platforms may have limitations in providing real-time interactions. Students may face delays

Table 3. Bibliographic references used on the mapping research

DOI or bibliographic reference	Publication year	Region (EU and other countries)	Reference
https://doi.org/10.1002/ar.b.10037	2003	USA	4
https://doi.org/10.1002/ar.b.20066	2005	USA	5
https://doi.org/10.1186/1746-1596-3-S1-S10	2008	EU — Czech Republic	6
https://doi.org/10.1016/j.acthis.2008.09.003	2009	Israel	7
https://doi.org/10.1016/j.humpath.2009.04.010	2009	USA	8
https://doi.org/10.1016/j.aanat.2010.01.008	2010	EU — Germany	9
https://doi.org/10.4415/ANN_10_02_07	2010	EU — Italy	10
https://doi.org/10.1186/1746-1596-5-73	2010	EU — Hungary	11
https://doi.org/10.1038/modpathol.2009.190	2010	Canada	12
https://doi.org/10.4415/ANN_10_02_03	2010	EU — Italy	13
https://doi.org/10.1186/1746-1596-6-S1-S13	2011	EU — Poland*	14
https://doi.org/10.5858/135.2.211	2011	USA	15
https://doi.org/10.1186/1472-6920-11-4	2011	USA	16
https://doi.org/10.1002/ase.262.	2011	USA	17
https://sciendo.com/pdf/10.2478/v10052-011-0003-4	2011	EU — Poland*	18
https://doi.org/10.1111/j.1600-0463.2011.02869	2012	UK — Northern Ireland	19
https://doi.org/10.1002/ase.1350	2013	USA	20
https://doi.org/10.1002/ase.1353	2013	EU — Belgium	21
https://doi.org/10.1186/s13000-014-0208-6	2014	EU — Poland*	22
http://dx.doi.org/10.1016/j.humpath.2014.06.007	2014	USA	23
http://hdl.handle.net/10045/49169	2015	EU — Spain*	24
http://drj.mui.ac.ir/index.php/drj/article/view/1870	2017	India	25
https://doi.org/10.1002/ase.1844	2018	Canada	26
https://doi.org/10.1097/JPA.0000000000000198	2018	USA	27
https://doi.org/10.21815/JDE.018.084	2018	Brazil	28
https://doi.org/10.1002/ase.1774	2018	USA	29
https://doi.org/10.1111/eje.12410	2018	EU — Czech Republic & Austria	30
https://doi.org/10.21315/eimj2019.11.4.5	2019	Malaysia	31
https://doi.org/10.1002/ase.1940	2019	Taiwan	32
https://doi.org/10.1109/ISETC50328.2020.9301150	2020	EU — Romania*	33
https://doi.org/10.1109/ISETC50328.2020.9301122	2020	EU — Romania*	34
https://doi.org/10.1109/EHB50910.2020.9280225	2020	EU — Romania*	35
https://doi.org/10.32015/JIBM/2020-12-1-8	2020	EU — Romania*	36
https://doi.org/10.4103/JMAU.JMAU_67_20	2020	Saudi Arabia & Egypt	37
https://doi.org/10.1016/j.jds.2021.03.011	2021	Taiwan	38
https://doi.org/10.1111/ahe.12765	2021	EU — Czech Republic & Austria	39

Table 3. (cont.) Bibliographic references used on the mapping research

DOI or bibliographic reference	Publication year	Region (EU and other countries)	Reference
https://doi.org/10.1002/ase.2072	2021	Brazil	40
https://doi.org/10.1002/ase.2038	2021	Australia	41
https://doi.org/10.18295/squmj.4.2021.009	2021	United Arab Emirates	42
https://doi.org/10.1177/23742895211006819	2021	USA	43
https://doi.org/10.21315/eimj2021.13.4.4	2021	Malaysia	44
https://doi.org/10.34808/x55q-sz53_dyr_roz3	2022	EU — Poland*	45
https://doi.org/10.1002/ase.2239	2022	USA	46
https://doi.org/10.1016/j.acpath.2022.100059	2022	USA	47
https://doi.org/10.1016/j.jds.2022.04.008	2022	Taiwan	48
https://doi.org/10.1016/j.mjafi.2022.02.002	2022	India	49
https://doi.org/10.3390/diagnostics13030558	2023	Commonwealth of Nations (Grenada, Cayman Islands, UK, Australia & India)	50

*Country of a VM3.0 partner
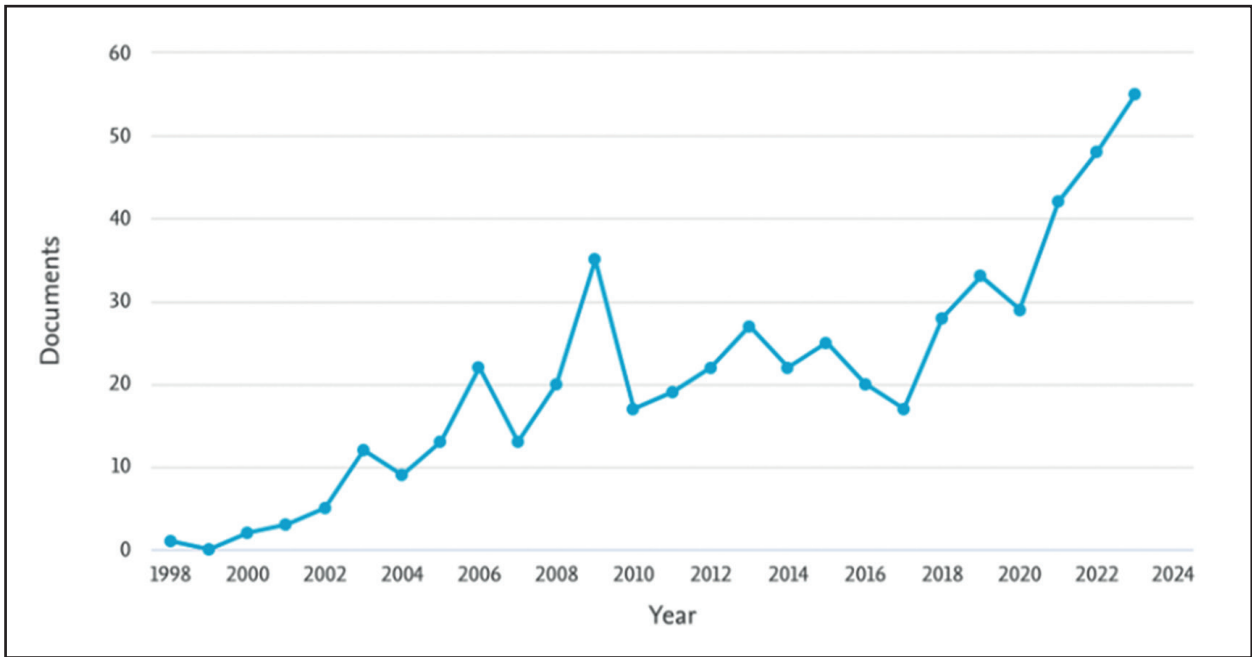
Figure 5. Number of publications per year related to the use of VM in teaching histology after a search on SCOPUS with the keyword's combination: "virtual" and "microscope" or "microscopy" and "histology".

or difficulties in navigating the digital slides, adjusting magnification, or accessing specific regions of interest. This can affect the flow of the learning process and hinder the spontaneous exploration of histological features.

• **Technical requirements and access:** Virtual microscopy relies on computer technology and internet connectivity. Access to suitable devices, software, and a stable internet connection may pose challenges for some students, especially those from economically disadvantaged backgrounds or regions with limited infrastructure. Technical issues or compatibility problems with different operating systems or devices can also hinder the learning experience.

- **Loss of whole slide context:** Virtual microscopy often involves viewing high-resolution images of individual fields or regions of a histological slide. This approach may limit the ability to appreciate the entire context of the tissue sample. Students may miss the overall architecture and relationships between different regions of the slide, which can be crucial in understanding tissue organization and identifying abnormal features.
- **Lack of physical slide examination:** Virtual microscopy eliminates the opportunity to examine physical slides under different lighting conditions, which can provide valuable information about the staining quality and structural characteristics. Observing slides under different light sources, such as polarized light or phase contrast, may reveal additional details that are not easily replicated in the digital format.
- **Loss of authenticity:** Virtual slides may not capture the exact appearance of the original histological samples due to variations in image quality, colour representation, or resolution. This loss of authenticity may impact the accuracy and realism of the learning experience, especially when it comes to subtle histological features or artifacts that are challenging to digitally replicate.

Despite these drawbacks, virtual microscopy remains a valuable tool in histology education, particularly when used in conjunction with traditional microscopy. Combining virtual microscopy with hands-on laboratory experiences can help mitigate some of these limitations and provide a more comprehensive learning environment.

Future development plans

In future, the VM3.0 system will include a tool called "Microscopic image description cassette" containing slide-specific keywords. This cassette will be available by a specific link.

The VM3.0 platform development will include a quiz section based on a collection of multiple-choice questions, three for each virtual slide section, comprising around 60 questions. The student can generate a test of ten questions from a specific module or from different selected modules, save the results, and thus, he will have his own statistics about his knowledge of histology or histopathology.

CONCLUSIONS

In summary, the cooperation of six European universities in the development of an innovative the VM3.0 project under the frames of the European Union Erasmus+ program resulted in the creation of a fast, and low-cost international online platform that will increase effectiveness of teaching/learning histology and histopathology, light microscopy-based sciences that are indispensable in the medical sciences studies curricula.

Article information and declarations

Data availability statement
Data presented are original and available upon reasonable request.

Ethics statement
The data comply to the Ethics regulations.

Author contributions
All authors contributed to the article and agreed on the submitted form.

Conflict of interest
There is no conflict of interest.

Supplementary material
Supplementary materials are available on Journal's website.

REFERENCES

1. Sergi CM. Digital pathology: the time is now to bridge the gap between medicine and technological singularity. In: Cvetković D. ed. Interactive multimedia — multimedia production and digital storytelling. IntechOpen, [online] 2019.
2. From Garage to State-of-the-Art Facility, Leica Biosystems Aperio Pioneers Digital Pathology. https://northcountydailystar.com/from-garage-to-state-of-the-art-facility-leica-biosystems-aperio-pioneers-digital-pathology/ (1.10.2023).
3. Aperio ImageScope — Pathology Slide Viewing Software. https://www.leicabiosystems.com/digital-pathology/manage/aperio-imagescope/ (1.10.2023).
4. Blake CA, Lavoie HA, Millette CF. Teaching medical histology at the University of South Carolina School of Medicine: transition to virtual slides and virtual microscopes. Anat Rec B New Anat. 2003; 275(1): 196–206, doi: 10.1002/ar.b.10037, indexed in Pubmed: 14628320.
5. Krippendorf BB, Lough J. Complete and rapid switch from light microscopy to virtual microscopy for teaching medical histology. Anat Rec B New Anat. 2005; 285(1): 19–25, doi: 10.1002/ar.b.20066, indexed in Pubmed: 16032757.
6. Feit J, Matyska L, Ulman V, et al. Virtual microscope interface to high resolution histological images. Diagn Pathol. 2008; 3 Suppl

1(Suppl 1): S10, doi: 10.1186/1746-1596-3-S1-S10, indexed in Pubmed: 18673498.

7. Coleman R. Can histology and pathology be taught without microscopes? The advantages and disadvantages of virtual histology. Acta Histochem. 2009; 111(1): 1–4, doi: 10.1016/j.acthis.2008.09.003, indexed in Pubmed: 19004481.

8. Dee FR. Virtual microscopy in pathology education. Hum Pathol. 2009; 40(8): 1112–1121, doi: 10.1016/j.humpath.2009.04.010, indexed in Pubmed: 19540551.

9. Merk M, Knuechel R, Perez-Bouza A. Web-based virtual microscopy at the RWTH Aachen University: didactic concept, methods and analysis of acceptance by the students. Ann Anat. 2010; 192(6): 383–387, doi: 10.1016/j.aanat.2010.01.008, indexed in Pubmed: 20363112.

10. Bondi A, Pierotti P, Crucitti P, et al. The virtual slide in the promotion of cytologic and hystologic quality in oncologic screenings. Ann Ist Super Sanita. 2010; 46(2): 144–150, doi: 10.4415/ANN_10_02_07, indexed in Pubmed: 20567065.

11. Fónyad L, Gerely L, Cserneky M, et al. Shifting gears higher — digital slides in graduate education — 4 years experience at Semmelweis University. Diagn Pathol. 2010; 5: 73, doi: 10.1186/1746-1596-5-73, indexed in Pubmed: 21092205.

12. Gabril MY, Yousef GM. Informatics for practicing anatomical pathologists: marking a new era in pathology practice. Mod Pathol. 2010; 23(3): 349–358, doi: 10.1038/modpathol.2009.190, indexed in Pubmed: 20081805.

13. Giansanti D, Grigioni M, D'Avenio G, et al. Virtual microscopy and digital cytology: state of the art. Ann Ist Super Sanita. 2010; 46(2): 115–122, doi: 10.4415/ANN_10_02_03, indexed in Pubmed: 20567061.

14. Szymas J, Lundin M. Five years of experience teaching pathology to dental students using the WebMicroscope. Diagn Pathol. 2011; 6 Suppl 1(Suppl 1): S13, doi: 10.1186/1746-1596-6-S1-S13, indexed in Pubmed: 21489183.

15. Hitchcock CL. The future of telepathology for the developing world. Arch Pathol Lab Med. 2011; 135(2): 211–214, doi: 10.5858/135.2.211, indexed in Pubmed: 21284440.

16. Triola MM, Holloway WJ. Enhanced virtual microscopy for collaborative education. BMC Med Educ. 2011; 11: 4, doi: 10.1186/1472-6920-11-4, indexed in Pubmed: 21269474.

17. Collier L, Dunham S, Braun MW, et al. Optical versus virtual: teaching assistant perceptions of the use of virtual microscopy in an undergraduate human anatomy course. Anat Sci Educ. 2012; 5(1): 10–19, doi: 10.1002/ase.262, indexed in Pubmed: 22069298.

18. Filipiak K, Malińska A, Krupa D, et al. Innovative methods of archiving, presentation and providing access to histological sections. Med J Cell Biol. 2011; 3(3): 41–53, doi: 10.2478/v10052-011-0003-4.

19. Hamilton PW, Wang Y, McCullough SJ. Virtual microscopy and digital pathology in training and education. APMIS. 2012; 120(4): 305–315, doi: 10.1111/j.1600-0463.2011.02869.x, indexed in Pubmed: 22429213.

20. Mione S, Valcke M, Cornelissen M. Evaluation of virtual microscopy in medical histology teaching. Anat Sci Educ. 2013; 6(5): 307–315, doi: 10.1002/ase.1353, indexed in Pubmed: 23463716.

21. Khalil MK, Kirkley DL, Kibble JD. Development and evaluation of an interactive electronic laboratory manual for cooperative learning of medical histology. Anat Sci Educ. 2013; 6(5): 342–350, doi: 10.1002/ase.1350, indexed in Pubmed: 23408507.

22. Walkowski S, Lundin M, Szymas J, et al. Students' performance during practical examination on whole slide images using view path tracking. Diagn Pathol. 2014; 9: 208, doi: 10.1186/s13000-014-0208-6, indexed in Pubmed: 25358824.

23. Craig FE, McGee JB, Mahoney JF, et al. The Virtual Pathology Instructor: a medical student teaching tool developed using patient simulator software. Hum Pathol. 2014; 45(10): 1985–1994, doi: 10.1016/j.humpath.2014.06.007, indexed in Pubmed: 25090919.

24. de Juan Herrero J, Girela HL, Pérez-Cañaveras RM, de Juan A. XIII Jornadas de Redes de Investigación en Docencia Universitaria [Recurso electrónico]: Nuevas estrategias organizativas y metodológicas en la formación universitaria para responder a la necesidad de adaptación y cambio. Universidad de Alicante, Alicante 2015.

25. Hande A, Lohe V, Chaudhary M, et al. Impact of virtual microscopy with conventional microscopy on student learning in dental histology. Dent Res J. 2017; 14(2): 111, doi: 10.4103/1735-3327.205788.

26. Kuo KH, Leo JM. Optical versus virtual microscope for medical education: a systematic review. Anat Sci Educ. 2019; 12(6): 678–685, doi: 10.1002/ase.1844, indexed in Pubmed: 30414261.

27. Lee LMJ, Goldman HM, Hortsch M. The virtual microscopy database — sharing digital microscope images for research and education. Anat Sci Educ. 2018; 11(5): 510–515, doi: 10.1002/ase.1774, indexed in Pubmed: 29444388.

28. McDaniel MJ, Russell GB, Crandall SJ. Innovative strategies for clinical microscopy instruction: virtual versus light microscopy. J Physician Assist Educ. 2018; 29(2): 109–114, doi: 10.1097/JPA.0000000000000198, indexed in Pubmed: 29697587.

29. Fernandes CIR, Bonan RF, Bonan PRF, et al. Dental students' perceptions and performance in use of conventional and virtual microscopy in oral pathology. J Dent Educ. 2018; 82(8): 883–890, doi: 10.21815/JDE.018.084, indexed in Pubmed: 30068778.

30. Tauber Z, Cizkova K, Lichnovska R, et al. Evaluation of the effectiveness of the presentation of virtual histology slides by students during classes. Are there any differences in approach between dentistry and general medicine students? Eur J Dent Educ. 2019; 23(2): 119–126, doi: 10.1111/eje.12410, indexed in Pubmed: 30582772.

31. Simok A, Hadie@Haji S, Manan@Sulong HA, et al. The impact of virtual microscopy on medical students' intrinsic motivation. Educ Med J. 2019; 14(4): 47–59, doi: 10.21315/eimj2019.11.4.5.

32. Lee BC, Hsieh ST, Chang YL, et al. A web-based virtual microscopy platform for improving academic performance in histology and pathology laboratory courses: a pilot study. Anat Sci Educ. 2020; 13(6): 743–758, doi: 10.1002/ase.1940, indexed in Pubmed: 31883209.

33. Cosnita R, Cimpean AM, Raica M. Online versus on-site e-assessment in medical education: are we ready for the change? ISETC. 2020, doi: 10.1109/isetc50328.2020.9301150.

34. Cimpean A, Cosnita RM, Raica M. To "paint" with human tissues and modern technology: this is art in histology gamification. ISETC. 2020, doi: 10.1109/isetc50328.2020.9301122.

35. Cosnita R, Cimpean A, Maerz R, et al. Opening the door through the e-learning and eassessment for preclinical medical education in romania: academic, social and psychological impact. 2020 International Conference on e-Health and Bioengineering (EHB). 2020, doi: 10.1109/ehb50910.2020.9280225.

36. Cosnita R, Cimpean A, Raica M. E-Learning and e-assessement: two big challenges of medical education management in romania. J Innov Bus Manag. 2020; 12(1): 61–71, doi: 10.32015/jibm/2020-12-1-8.

37. Amer MG, Nemenqani DM. Successful use of virtual microscopy in the assessment of practical histology during pandemic COVID-19: a descriptive study. J Microsc Ultrastruct. 2020; 8(4): 156–161, doi: 10.4103/JMAU.JMAU_67_20, indexed in Pubmed: 33623740.

38. Chang JYF, Lin TC, Wang LH, et al. Comparison of virtual microscopy and real microscopy for learning oral pathology laboratory course among dental students. J Dent Sci. 2021; 16(3): 840–845, doi: 10.1016/j.jds.2021.03.011, indexed in Pubmed: 34141097.

39. Kolinko Y, Malečková A, Kochová P, et al. Using virtual microscopy for the development of sampling strategies in quantitative histology and design-based stereology. Anat Histol Embryol. 2022; 51(1): 3–22, doi: 10.1111/ahe.12765, indexed in Pubmed: 34806204.

40. Somera Dos Santos F, Osako MK, Perdoná Gd, et al. Virtual microscopy as a learning tool in brazilian medical education. Anat Sci Educ. 2021; 14(4): 408–416, doi: 10.1002/ase.2072, indexed in Pubmed: 33720510.

41. Caruso MC. Virtual microscopy and other technologies for teaching histology during COVID-19. Anat Sci Educ. 2021; 14(1): 19–21, doi: 10.1002/ase.2038, indexed in Pubmed: 33283455.

42. Lakhtakia R. Virtual microscopy in undergraduate pathology education: an early transformative experience in clinical reasoning. Sultan Qaboos Univ Med J. 2021; 21(3): 428–435, doi: 10.18295/squmj.4.2021.009, indexed in Pubmed: 34522409.

43. Christian RJ, VanSandt M. Using dynamic virtual microscopy to train pathology residents during the pandemic: perspectives on pathology education in the age of COVID-19. Acad Pathol. 2021; 8: 23742895211006819, doi: 10.1177/23742895211006819, indexed in Pubmed: 33884292.

44. Simok AA, Kasim F, Hadie S, et al. Knowledge acquisition and satisfaction of virtual microscopy usage among medical students of universiti sains malaysia. Educ Med J. 2021; 13(4): 43–55, doi: 10.21315/eimj2021.13.4.4.

45. Skokowski J, Bolcewicz M, Jendernalik K. et al. The digital tissue and cell atlas and the virtual microscope. Politechnika Gdańska, Gdańsk 2022: 61–69.

46. Hortsch M. The Michigan Histology website as an example of a free anatomical resource serving learners and educators worldwide. Anat Sci Educ. 2023; 16(3): 363–371, doi: 10.1002/ase.2239, indexed in Pubmed: 36453096.

47. Birkness-Gartman JE, White MJ, Salimian KJ, et al. Web-based pathology modules with virtual slides are effective for teaching introductory gastrointestinal pathology concepts. Acad Pathol. 2022; 9(1): 100059, doi: 10.1016/j.acpath.2022.100059, indexed in Pubmed: 36451746.

48. Wu YH, Chiang CP. Comparison of virtual microscopy and real microscopy for learning oral histology laboratory course among dental students. J Dent Sci. 2022; 17(3): 1201–1205, doi: 10.1016/j.jds.2022.04.008, indexed in Pubmed: 35784135.

49. Francis DV, Charles AS, Jacob TM, et al. Virtual microscopy as a teaching-learning tool for histology in a competency-based medical curriculum. Med J Armed Forces India. 2023; 79(Suppl 1): S156–S164, doi: 10.1016/j.mjafi.2022.02.002, indexed in Pubmed: 38144628.

50. Maity S, Nauhria S, Nayak N, et al. Virtual versus light microscopy usage among students: a systematic review and meta-analytic evidence in medical education. Diagnostics (Basel). 2023; 13(3), doi: 10.3390/diagnostics13030558, indexed in Pubmed: 36766660.

ORIGINAL PAPER

VM
VIA MEDICA

Mitofusin 2 inhibits high glucose-induced apoptosis of human lens epithelial cells *via* modulating mitochondrial function and autophagy

Yuan-Yi Guo[1], Jiang-Yue Zhao[2], Han-Rong Li[2], Zhuo Guo[2], Hao-Yue Shen[2]

[1]Department of Ophthalmology, the Fourth People's Hospital of Shenyang, Shenyang, Liaoning Province, People's Republic of China

[2]Department of Ophthalmology, the Fourth Affiliated Hospital of China Medical University, Shenyang, Liaoning Province, People's Republic of China

Abstract

Introduction. Diabetic cataract (DC) is a common ocular complication of diabetes. Mitofusin 2 (MFN2), a mitochondrial fusion protein, is involved in the pathogenesis of cataract and diabetic complications. However, its role and molecular mechanisms in DC remain unclear.

Materials and methods. DC models in rats were induced by intraperitoneal injection of streptozocin (STZ) for 12 weeks. We measured the body weight of rats, blood glucose concentrations, sorbitol dehydrogenase (SDH) activity and advanced glycation end products (AGE) content in the lenses of rats. MFN2 mRNA and protein expression levels in the lenses were detected by RT-qPCR and western blot assays. In vitro, human lens epithelial (HLE) B3 cells were treated for 48 h with 25 mM glucose (high glucose, HG) to induce cell damage. To determine the role of MFN2 in HG-induced cell damage, HLE-B3 cells were transfected with lentivirus loaded with MFN2 overexpression plasmid or short hairpin RNA (shRNA) to overexpress or knock down MFN2 expression, followed by HG exposure. Cell viability was assessed by CCK-8 assay. Flow cytometry was used to detect cell apoptosis and reactive oxygen species (ROS) level. JC-1 staining showed the changes in mitochondrial membrane potential ($\Delta\psi$m). The mediators related to apoptosis, mitochondrial damage, and autophagy were determined.

Results. STZ-administrated rats showed reduced body weight, increased blood glucose levels, elevated SDH activity and AGE content, suggesting successful establishment of the DC rat model. Interestingly, MFN2 expression was significantly downregulated in DC rat lens and HG-induced HLE-B3 cells. Further analysis showed that under HG conditions, MFN2 overexpression enhanced cell viability and inhibited apoptosis accompanied by decreased Bax, cleaved caspase-9 and increased Bcl-2 expression in HLE-B3 cells. MFN2 overexpression also suppressed the mitochondrial damage elicited by HG as manifested by reduced ROS production, recovered $\Delta\psi$m and increased mitochondrial cytochrome c (Cyto c) level. Moreover, MFN2 overexpression increased LC3BII/LC3BI ratio and Beclin-1 expression, but decreased p62 level, and blocked the phosphorylation of mTOR in HG-treated HLE-B3 cells. In contrast, MFN2 silencing exerted opposite effects.

Conclusions. Presented findings indicate that MFN2 expression may be essential for preventing lens epithelial cell apoptosis during development of diabetic cataract. *(Folia Histochem Cytobiol 2024; 62, 2: 76–86)*

Keywords: MFN2; overexpression; diabetic cataract; mitochondrial membrane potential; autophagy; apoptosis

Correspondence addresses:

Dr. Yuan-Yi Guo
Department of Ophthalmology, the Fourth People's Hospital of Shenyang
No. 20, Huanghe South Street, Shenyang, Liaoning Province, People's Republic of China
e-mail: gyy_91zgsy@163.com

Dr. Jiang-Yue Zhao
Department of Ophthalmology, the Fourth Affiliated Hospital of China Medical University,
No. 4, Chongshan East Road, Shenyang, Liaoning Province, People's Republic of China
e-mail: jyzhao@cmu.edu.cn

Graphical abstract
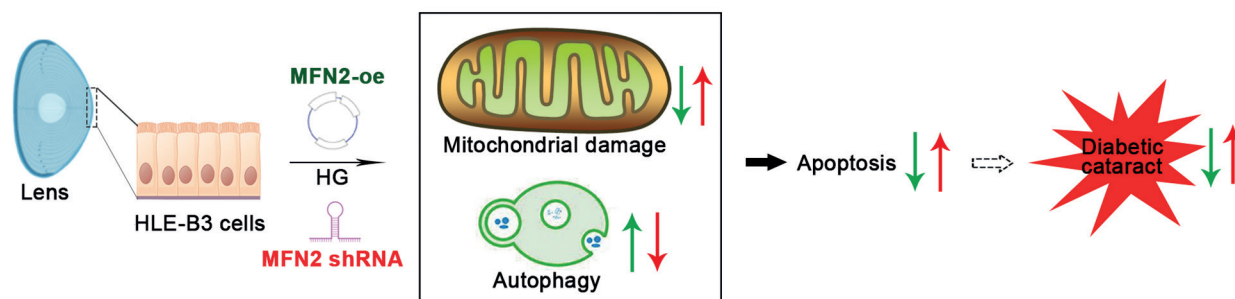
INTRODUCTION

Diabetes mellitus, a metabolic disease characterized by elevated serum/blood glucose concentration, is expected to afflict 629 million people worldwide by the year 2045 [1]. Diabetic cataract (DC) is a common complication of diabetes, generally defined as lens opacity, and is the leading cause of blindness globally [1, 2]. Abundant evidence indicates that patients with diabetes are accompanied by increased incidence and earlier development of cataracts [3, 4]. At present, surgery has been accepted as the best method to treat cataract, but it may develop ocular complications [4, 5]. Lens epithelial cells (LECs), located in the anterior capsule of the lens, are responsible for the differentiation of lens fiber cells and for maintaining the transparency of the lens [6]. LEC apoptosis is the molecular basis of cataractogenesis [7–9], and the injury of which may contribute to the progression of DC. Therefore, inhibition of LEC apoptosis is of great significance in preventing the development of DC.

Mitochondrial fusion, a major process of mitochondrial dynamics, is found to possess a beneficial role in mitochondrial homeostasis [10]. Mitofusin 2 (MFN2), a conserved mitochondrial fusion protein primarily localized in the outer membrane of mitochondria, however, its expression has also been noted in the cytosol [11]. MFN2 has been reported to be implicated in the regulation of the progression of human obesity and type 2 diabetes [12, 13]. MFN2 attenuates kidney lesion [14, 15] and repairs retinal endothelial cell damage in diabetic rats [14–16]. A study of MFN2 conditional knockout in rat embryo revealed that loss of MFN2 function increased apoptosis and mitochondrial impairment in LECs, thereby leading to congenital eye defects including opacified lens [17]. Interestingly, the expression of MFN2 is widely downregulated in the kidney, heart, penile tissue and retina of streptozotocin (STZ)-induced diabetic rats compared to normal rats [18]. Nevertheless, few studies have shown the expression of MFN2 in the lens and its exact role in LEC injury associated with DC.

Herein, we identified downregulated MFN2 in the lens of STZ-induced diabetic rats. Human lens epithelium HLE-B3 cells were incubated in the culture medium containing glucose at a high concentration (high glucose, HG) to induce cell injury. We unraveled the significant role of MFN2 in improving mitochondrial function, reducing apoptosis, and activating autophagy. These findings indicate that targeting MFN2 may be a promising strategy for DC treatment.

MATERIALS AND METHODS

Animal model

The Ethic Committee of the China Medical University (Shenyang, China; No. cmu2022045) approved all animal experiments. Experimental procedures were carried out in accordance with relevant guidelines and regulations. In this study, healthy male SD rats were kept in a temperature- and humidity-controlled room ($22 \pm 1°C$ and 45–55%, respectively) with 12 h/12 h light/dark cycle and given free access to food and water.

One week after adaptation, the rats were intraperitoneally injected with a single dose of STZ (65 mg/kg body weight) dissolved in 0.1 M sodium citrate (pH 4.5). The control rats received the vehicle only. At 72 h after STZ administration, fasting blood glucose levels were measured by a glucometer using blood taken from the tail tips. The rats with blood glucose levels > 16.7 mM were regarded as diabetic and were selected for the following experiments. At 4, 8 and 12 weeks after STZ injection, the body weights of rats were recorded and blood was harvested from the tail tips for blood glucose level measurement. At the

end of week 12, the opacity of the lens was monitored using a slit lamp [19]. Allanimals were euthanized *via* intraperitoneal (*i.p.*) injection of pentobarbital sodium overdose (200 mg/kg), and the eyeballs were excised and photographed. The lenses were then dissected and frozen at –80°C until further analyses.

Biochemical estimations

Lens tissues were immersed in saline (tissue weight (g): saline volume (mL) = 1: 10), homogenized on ice using a glass homogenizer and centrifuged at 4°C for 10 min at 8000×*g*. The supernatant was collected for quantification of protein concentration using a BCA protein quantification kit (Beyotime, Nantong, Jiangsu, China). The activity of sorbitol dehydrogenase (SDH) was estimated in accordance with the protocol of the manufacturer (Nanjing Jiancheng, Nanjing, Jiangsu, China). For measurement of lens advanced glycation end product (AGE) content, the saline was added to the lens tissues as weight (g): volume (mL) = 1: 9, and then the samples were homogenized and centrifuged at 430×*g* for 10 min. After quantification of protein concentration (BCA kit), the AGE content was determined using an AGE detection kit (USCN, Wuhan, Hubei, China) according to the manufacturer's instruction.

Lentivirus

For overexpression, MFN2 CDS (NM_014874.3) was subcloned into a lentiviral vector pLVX-IRES-puro (FENGHUI, China). For MFN2 knockdown, short hairpin RNA (shRNA) targeting MFN2 was inserted into pLVX-shRNA1 vector (FENGHUI, China). The targeting sequence included in the shRNA was 5'-GGACGTCAAAGGTTACCTATC-3'. Lentiviruses were generated in HEK293T cells (Icellbioscience, China) transfected with plasmids pLVX-IRES-puro or pLVX-shRNA1, pSPAX2 (FENGHUI, China) and pMD2.G (FENGHUI, China) by using Lipofectamine 3000 (Invitrogen, USA) in accordance with the recommended protocols. Viral Cell supernatants containing lentiviruses were harvested after 48 h and 72 h of transfection. The transfection efficiency was measured using RT-qPCR and western blotting assays (Suppl. Fig. 1).

Cell culture and treatment

Human lens epithelial (HLE) B3 cells were obtained from American Type Culture Collection (USA) and cultured in Dulbecco's modified Eagles media (DMEM) containing 10% fetal bovine serum. The culture media were placed in an incubator at 37°C and 5% CO_2. After the cells reached 70% confluence, they were subjected to normal glucose (NG) medium (5.5 mmol/L glucose), osmolarity control medium (5.5 mmol/L glucose and 19.5 mmol/L mannitol) or high glucose (HG) medium (25 mmol/L glucose) for 48 h. NG was used as a control. In addition, prior to exposure to HG for 48 h, the cells were transfected with the above recombinant lentiviruses.

Cell counting kit-8 (CCK-8) assay

HLE-B3 cells were seeded in 96-well plates and cultured at 37°C for 48 h. Then, 10 μL CCK-8 solution (Solarbio, Beijing, China) was added to each well, and cells were incubated for another 2 h. After that, the absorbance (optical density) was read at 450 nm with a microplate reader (800TS, Biotek, Winooski, VT, USA).

Reverse transcription quantitative polymerase chain reaction (RT-qPCR) assay

Referring to the manufacturer's instructions, total RNA from lens and HLE-B3 cells was extracted using TRIpure Isolation Reagent (BioTeke, Wuxi, Jiangsu, China) and complementary DNA (cDNA) was generated using BeyoRT II M-MLV reverse transcriptase. Then RT-qPCR reaction was done *via* SYBR Green PCR Master Mix (Solarbio). The cycling parameters were 95.00°C for 5 min and 40 cycles of 95.00°C for 10 s, 60.00°C for 10 s, 72.00°C for 15 s, followed by 72.00°C for 90 s, 40.00°C for 60 s, melting 60°C to 94°C with a 1.0°C increase every 1 s, and 25.00°C for 1–2 min. The primer sequences used were: rat MFN2 forward, 5'-GCCGTCCGTCTCATCAT-3' and reverse, 5'-GGCGGTGCAGTTCATTC-3'; homo MFN2 forward, 5'-CGCAGAAGGCTTTCAAGT-3' and reverse, 5'-ACGCATTTCCTCGCAGTA-3'. The Ct values were recorded and the relative abundance of the products was estimated using the $2^{-\Delta\Delta Ct}$ method [20].

Mitochondrial extraction

Mitochondrial proteins were extracted using a Mitochondria Protein extraction kit (Nanjing Jiancheng). According to the manufacturer's protocols, the cells (5×10^7) were washed with phosphate-buffered saline (PBS) and centrifuged at 800×*g*, and then the cells were suspended in lysing solution for 15 min on ice. After lysing with 30–40 strokes with a homogenizer, cell supernatant was harvested by centrifugation for 5 min (800×*g*) and transferred to a new tube. The reagents were added and the tube was centrifuged for 10 min at 15,000×*g* at 4°C. The mitochondria (precipitate) and cytoplasm (supernatant) fractions were obtained for western blot analysis.

Western blot analysis

Total proteins were produced utilizing RIPA buffer solution (Solarbio), followed by protein concentration detection using BCA quantification kit (Solarbio). Proteins were separated by SDS-PAGE and blotted on PVDF membranes (Millipore, Burlington, MA, USA). Afterwards, the membranes were sealed with 5% (M/V) skim milk, and incubated with primary antibodies (overnight, 4℃) and secondary antibody (1 h, 37℃). The diluted antibodies used in this study contained primary antibodies against MFN2 (abclonal, A19678, 1:1000), Bcl-2 (proteintech, 12789-1-AP, 1:500), Bax (abclonal, A19684, 1:1000), cleaved caspase-9 (cst, #20750, 1:1000), Cyto c (proteintech, 10993-1-AP, 1:500), LC3II/I (abclonal, A5618, 1:1000), Beclin-1 (affinity, AF5128, 1:1000), p62 (abclonal, A19700, 1:1000), phospho (p)-mTOR (affinity, AF3308, 1:500), mTOR (affinity, AF6308, 1:500) and secondary anti-rabbit IgG, HRP-conjugated antibody (Solarbio, 1:3000). The signals were observed *via* an enhanced chemiluminescence method.

Flow cytometry analysis for cell apoptosis

To quantify apoptosis, HLE-B3 cells cultured for 48 h were harvested and incubated in the dark for 10 min with 5 μL AnnexinV-FITC and 10 μL propidium iodide (PI, Biosharp, Hefei, Anhui, China). Then, a flow cytometer (NovoCyte) was applied to analyze the percentage of apoptotic cells.
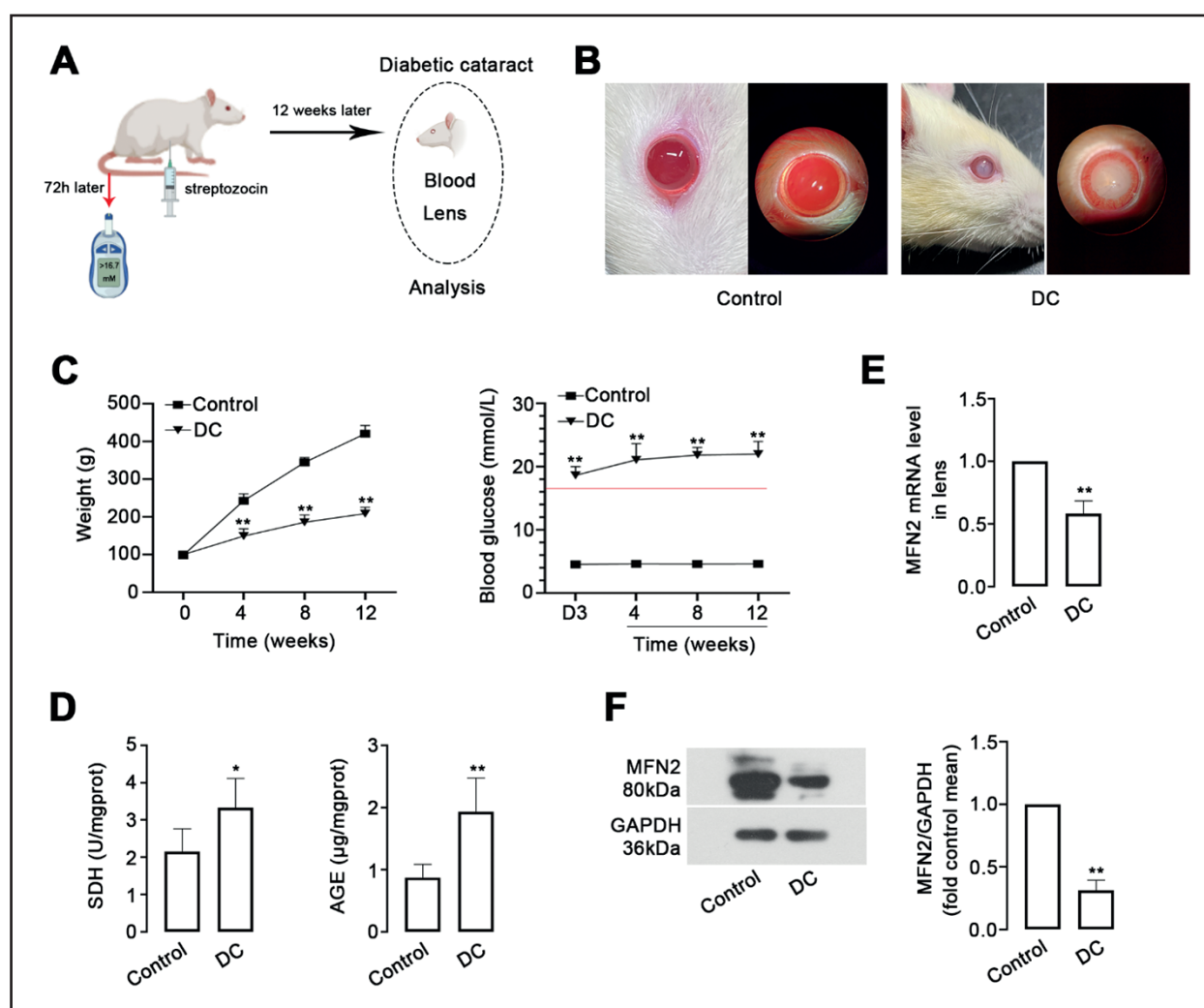
Figure 1. MFN2 is involved in diabetic cataract formation. **A.** Experimental design. Healthy male SD rats were subjected to 65 mg/kg streptozocin (STZ) intraperitoneally. After 72 h, the fasting blood glucose was evaluated. Rats with blood glucose levels greater than 16 mM were selected for further study. **B.** After 12 weeks, representative slit lamp photographs of lens were shown. **C.** The average body weight of diabetic rats and average blood glucose level at different time points after STZ injection. **D.** Changes in SDH activity and AGE levels in lens. **E, F.** MFN2 expression was downregulated in the lens of rats with diabetic cataract as displayed by RT-qPCR and western blot. *P < 0.05, **P < 0.01 *vs.* the control.

Determination of reactive oxygen species (ROS)

Reactive oxygen species (ROS) test kit was purchased from Beyotime (China). After treatment, HLE-B3 cells were incubated with diluted 2',7'-dichlorodihydrofluorescein diacetate (DCFH-DA) reagent (1:1000) at 37°C for 20–30 min. After that, cells were collected by centrifugation for 5 min (160×g) and were resuspended in 500 μL PBS, and then ROS was detected by flow cytometry (20000 gated cells).

Measurement of mitochondrial membrane potential ($\Delta\psi$m)

The alterations of mitochondrial membrane potential ($\Delta\psi$m) were determined by cationic dye JC-1 (Beyotime). Cultured HLE-B3 cells were collected and stained with 1 mL JC-1 staining solution at 37°C for 20 min. After washing twice with 1× JC-1 buffer, the cells were analyzed by flow cytometry (20000 gated cells).
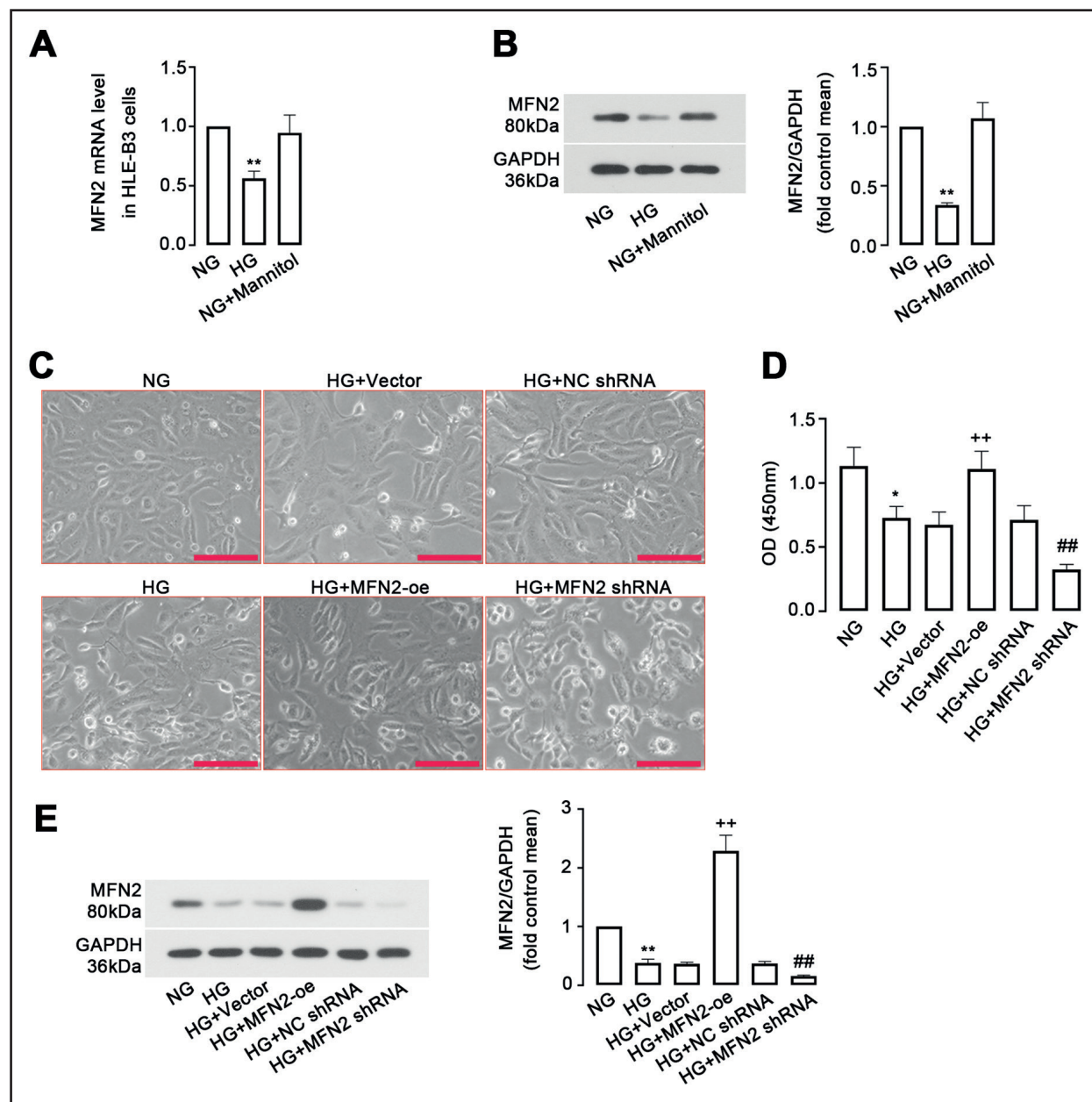
Figure 2. MFN2 expression in high glucose-induced HLE-B3 cells. **A, B.** HLE-B3 cells were treated with high glucose (HG), normal glucose (NG), or mannitol for 48 h, and then MFN2 expression was confirmed by RT-qPCR and western blot assays. **C.** HLE-B3 cells were transfected with lentivirus-mediated MFN2 overexpression vector or shRNA for 48 h, followed by HG or NG treatment for another 48 h. The morphological change of HLE-B3 cells was shown. Black arrows point to individual cells. Scale bar = 200 μm. **D.** CCK-8 assay revealed cell viability in different groups. **E.** The protein level of MFN2 in HLE-B3 cells, as measured by western blot. *P < 0.05, **P < 0.01, *vs.* NG as control; ++P < 0.01, *vs.* HG + Vector as control; ##P < 0.01, *vs.* HG + NC shRNA as control.

Data analysis

Data were expressed as mean ± standard deviation (SD). All statistical analyses were carried out using GraphPad Prism software, version 8.0 (GraphPad Software, Boston, MA, USA). Differences were indicated by independent sample t-test or one-way ANOVA, where appropriate. P values less than 0.05 were taken as statistically significant.

RESULTS

MFN2 expression is downregulated in lens of DC rat

MFN2 has a protective effect against diabetic complications such as diabetic nephropathy; however, there is no data on whether MFN2 is implicated in DC development. In the present study, we established an in vivo rat model of DC via administrating STZ, as exhibited in Fig. 1A. Twelve weeks after STZ injection, the lenses of the rats became turbid compared with the control group (Fig. 1B). Moreover, the body weight of rats was significantly decreased at 4, 8 and 12 weeks after STZ injection. The fasting blood

glucose levels were maintained above 16.7 mmol/L at 72 h after STZ induction, and increased at 4, 8 and 12 weeks after STZ injection (Fig. 1C). Besides, DC rats showed elevated SDH activity and AGE formation in the lens (Fig. 1D). Notably, RT-qPCR and western blot assays confirmed that the mRNA and protein levels of MFN2 in the lens of DC rats were significantly lower than those of control rats (Fig. 1E, F), which indicates that MFN2 may participate in DC progression.

Effect of MFN2 on morphology and viability of HLE-B3 cells

In comparison to NG group, MFN2 expression was downregulated in HLE-B3 cells treated with HG (Fig. 2A, B). To explore the effect of MFN2 on HG-induced cell injury, HLE-B3 cells were transfected with recombinant lentiviruses mediated with MFN2 overexpression plasmid (MFN2-oe) or shRNA, followed by HG induction. Then, morphological changes of HLE-B3 cells in different groups were observed under a light microscope. Under NG
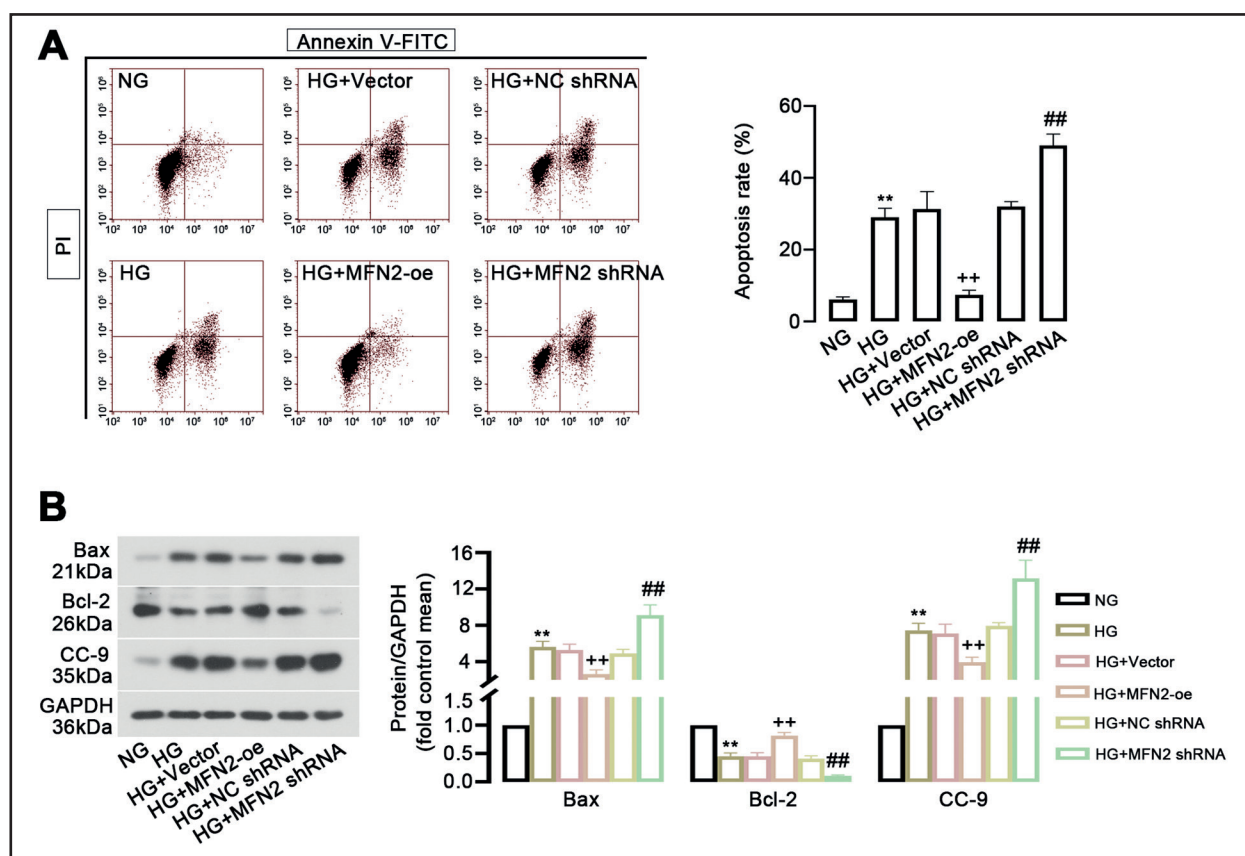
Figure 3. MFN2 regulates HLE-B3 cell apoptosis in response to HG. **A.** Flow cytometry was performed to measure the apoptosis rate of HLE-B3 cells in response to HG. **B.** Western blot characterization of apoptosis-related proteins and quantification. **P < 0.01, *vs.* NG as control; $^{++}$P < 0.01, *vs.* HG + Vector as control; $^{##}$P < 0.01, *vs.* HG + NC shRNA as control.

conditions, HLE-B3 cell morphology was regular. When exposed to HG, the cells showed elongated fiber-like form. Cell morphology turned to regular after MFN2 overexpression plasmid treatment, while cell damage appeared to be aggravated after MFN2 shRNA treatment (Fig. 2C). Besides, cell viability

by CCK-8 assay was decreased after HG exposure. MFN2-oe treatment increased the viability of HLE-B3 cells, but MFN2 shRNA treatment decreased it (Fig. 2D). MFN2 protein level by western blot analysis was significantly upregulated by MFN2-oe treatment, but downregulated by MFN2 shRNA treatment (Fig. 2E).
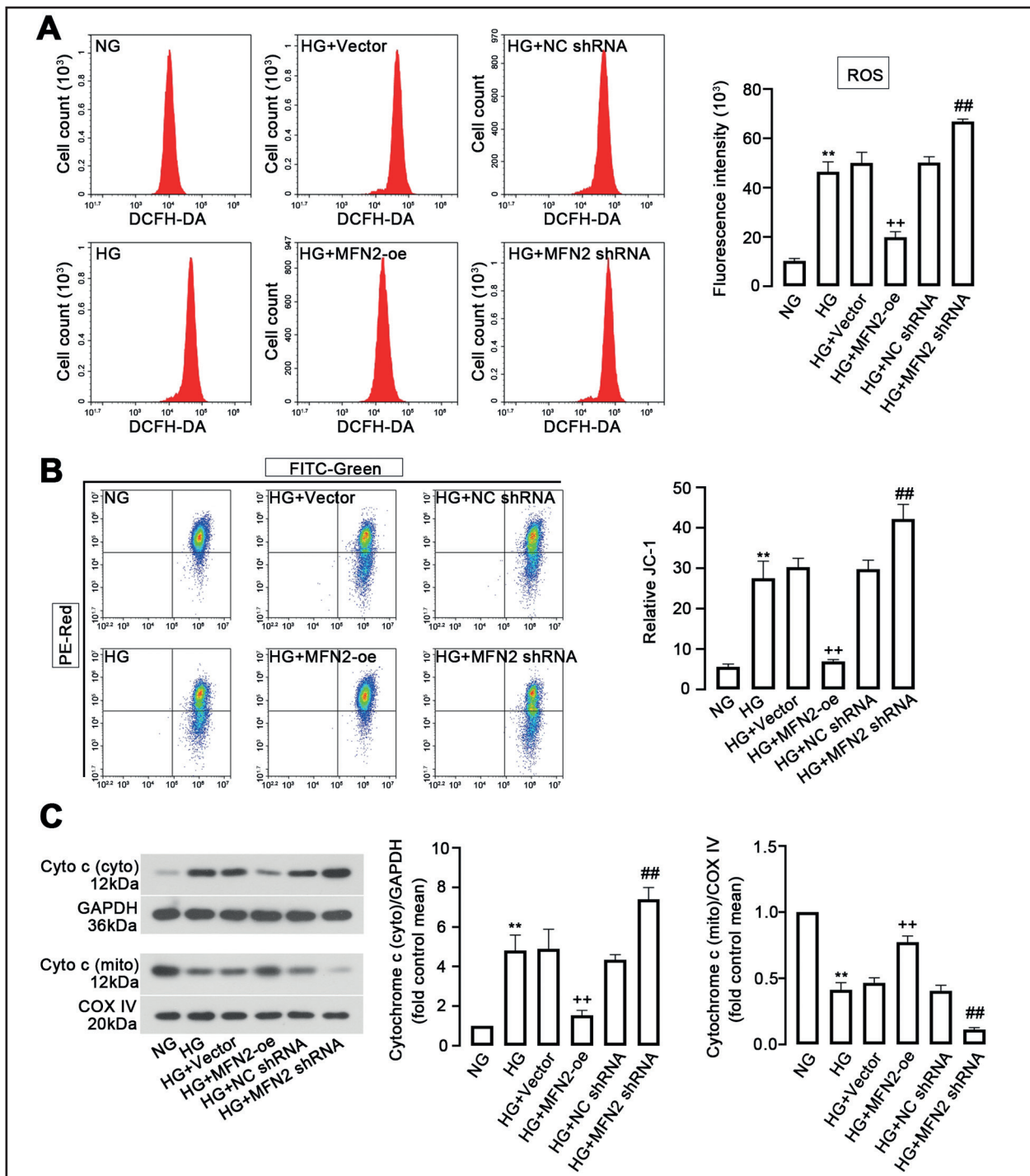
Figure 4. MFN2 affects mitochondria damage in HLE-B3 cells under HG conditions. **A.** Flow cytometry showed ROS level in HLE-B3 cells. **B.** Analysis of mitochondrial membrane potential by JC-1. **C.** Cytochrome c (Cyto c) expression in cytoplasm and mitochondria. **P < 0.01, *vs.* NG as control; ++P < 0.01, *vs.* HG + Vector as control; ##P < 0.01, *vs.* HG + NC shRNA as control.

MFN2 suppresses high glucose-induced HLE-B3 cell apoptosis

Annexin V/PI double staining assay was performed to evaluate the apoptosis of HLE-B3 cells in the presence of HG. As shown in Fig. 3A, following a 48-h treatment with HG, we observed an elevation in cell apoptosis rate. Treatment with MFN2-oe significantly reduced HG-induced HLE-B3 cell apoptosis, while MFN2 silencing increased this process. Moreover, MFN2 overexpression led to downregulated Bax and cleaved caspase-9 expression but upregulated Bcl-2 under HG conditions, and MFN2 silencing exerted the opposite effects (Fig. 3B).

MFN2 improves mitochondrial dysfunction induced by high glucose

The potential effect of MFN2 on HG-stimulated mitochondrial dysfunction in HLE-B3 cells was analyzed. ROS accumulation measured by flow cytometry was reduced following MFN2 overexpression in the presence of HG, whereas MFN2 silencing increased the ROS level (Fig. 4A). MFN2 overexpression also blunted the loss of $\Delta\psi$m caused by HG, while silencing MFN2 elevated it (Fig. 4B). Besides, western blot analysis showed that MFN2 overexpression declined the level of cytochrome c in the cytoplasm and increased it in the mitochondria under HG conditions. In contrast, MFN2 silencing increased the level of Cyto c released into the cytoplasm (Fig. 4C).

MFN2 activates high glucose-induced autophagy of HLE-B3 cells

As illustrated in Fig. 5A, treatment of HLE-B3 cells with MFN2-oe increased the expression of autophagy biomarkers LC3B and Beclin-1, but decreased p62 expression under HG conditions. However, MFN2 silencing reduced LC3B and Beclin-1 levels and increased p62. Further, we paid attention to the function of MFN2 in the mTOR signaling pathway involved in cataract formation [21, 22]. Western blot analysis
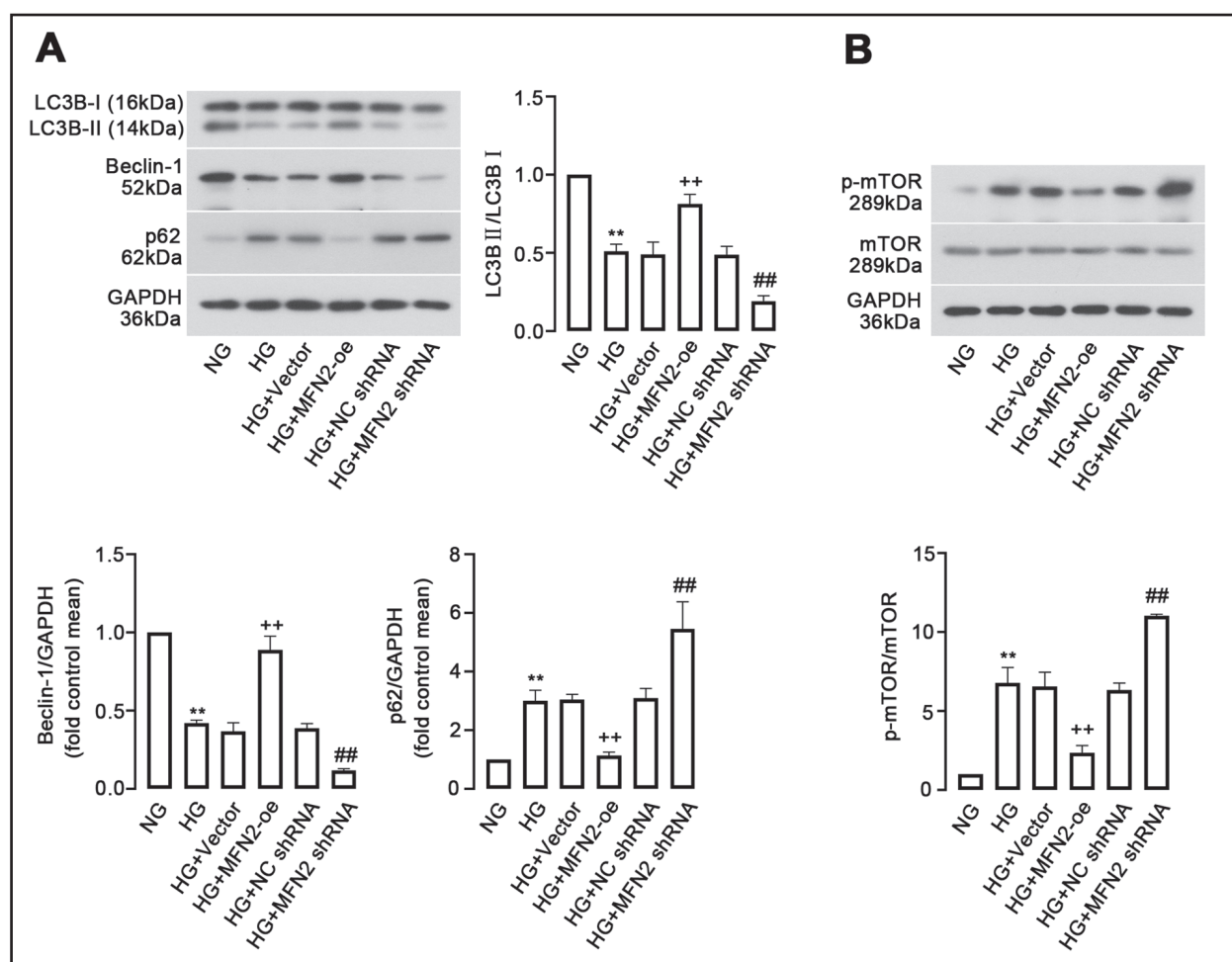

Figure 5. MFN2 alters autophagy in HLE-B3 cells upon HG stress. **A.** Western blot analysis of the markers (LC3BII, LC3BI, Beclin-1, p62) of autophagy in HLE-B3 cells. **B.** Western blot analysis of mTOR pathway-related proteins. **P < 0.01, *vs.* NG as control; $^{++}$P < 0.01, *vs.* HG + Vector as control; $^{\#\#}$P < 0.01, *vs.* HG + NC shRNA as control.

demonstrated that the HG-induced phosphorylation of mTOR in HLE-B3 cells was suppressed by over-expression of MFN2, whereas it was elevated by MFN2 silencing (Fig. 5B).

DISCUSSION

In the present study, we successfully constructed a rat model of DC and demonstrated, for the first time, decreased expression of MFN2 in the lens of STZ-exposed rats, indicating that MFN2 may be a key gene associated with DC. This study demonstrated that under HG conditions, *in vitro* overexpression of MFN2 could enhance cell viability, inhibit mitochondrial dysfunction and apoptosis, activate autophagy, whereas its silencing had the reverse effects. This study provides an important advance in understanding the pathogenesis of DC, and also provides a new clue for the treatment of disorders caused mainly by HG, including DC.

Lens epithelial cells (LECs) are the most active cell type in ocular lens and their abnormal function takes main blame for lens opacity. The death of LECs induced by apoptosis is a key cause of DC formation [23]. Here, we demonstrated that MFN2 was downregulated in HG-induced HLE-B3 cells. Also, MFN2 overexpression suppressed cell apoptosis, accompanied by the reduction in pro-apoptotic proteins Bax and cleaved caspase-9 and the increase in anti-apoptotic protein Bcl-2 expression. MFN2 silencing had the opposite effects. We propose that under HG conditions, MFN2 is a critical regulator of apoptosis in LECs. There is increasing evidence that mitochondrial pathway is relevant to apoptosis and is considered to be the basic mechanism modulating cell injury [24, 25]. Previous studies have suggested that damaged mitochondria of LECs can initiate the occurrence and development of DC, and exposure of LECs to HG can result in mitochondrial dysfunction and apoptosis [26]. Consistent with these reports, in this study, increased ROS accumulation, decreased $\Delta\psi m$ and elevated level of Cyto c released into the cytoplasm were observed, confirming the disruption of mitochondrial function in HLE-B3 cells in response to HG. MFN2, a well-known regulator of mitochondrial fusion, plays beneficial roles in diabetes-related heart diseases [27, 28]. Moreover, MFN2 deficiency has been reported to lead to abnormal mitochondrial morphology and severe mitochondrial dysfunction in mouse embryonic fibroblasts, 3T3-L1 and C2C12 cells or in macrophages [13, 29, 30]. In agreement with the previous reports, this study confirmed that the damage of mitochondria in HLE-B3 cells caused

by HG was attenuated by treatment with MFN2-oe, but further aggravated by MFN2 silencing. On the basis of these observations, we suggest that MFN2 plays a key role in restoring mitochondrial function in HG-induced HLE-B3 cells. In addition, mitochondria and endoplasmic reticulum (ER) are distinct organelles that physically interact with each other, including exchange of phospholipids, calcium and other metabolites to maintain cellular integrity and bioenergetics [31–33]. Previous studies have reported that MFN2 promotes the contact of mitochondria and ER [32, 34, 35]. Whether MFN2 plays a role in mitochondria-ER contacts (MERCs) in DC deserves further investigation.

Autophagy or "self-eating" in cells is an evolutionally conserved defense and stress mechanism that exerts a critically important role in the development of diabetes as well as its complications [36, 37]. Increased or reduced autophagy may trigger cell apoptosis, and a base level of autophagy is essential for maintaining intracellular homeostasis [38, 39]. Prior studies have revealed that exposure of HLE-B3 cells to HG contributes to a low level of autophagy, thereby possibly facilitating DC formation [40], which was consistent with the observation in HLE-B3 cells. MFN2 has been reported to induce autophagy, regulate the expression of autophagy-related proteins and suppress the activation of mTOR signaling pathway in Aspc-1 cells [41]. Current results were consistent with the previous findings, and the data suggested that MFN2 activated autophagy in HG-treated HLE-B3 cells. Intriguingly, presented results revealed that MFN2 overexpression led to a decrease in the phosphorylation of mTOR in HG-stimulated HLE-B3 cells, whereas MFN2 silencing accelerated this process, implying that mTOR signaling pathway may be one of the downstream signaling cascades implicated in MFN2-mediated regulation of autophagy. Although we demonstrated the beneficial effect of MFN2 overexpression on inhibiting HG-stimulated apoptosis, further researches are required to clarify the way MFN2 protects against HG-triggered LEC damage and to investigate whether MFN2 overexpression can alleviate the development of DC.

CONCLUSIONS

In summary, this report uncovers that MFN2 can inhibit mitochondrial dysfunction, elevate autophagy and reduce apoptosis in LECs cultured under HG conditions. These observations allow us to propose that MFN2 plays an important role in LECs apoptosis under HG conditions, and this study provides a new direction for DC therapy.

Article information and declarations

Data availability statement
All data used in the current study are available upon reasonable request.

Ethics statement
The Ethic Committee of the Fourth Affiliated Hospital of China Medical University (No. cmu2022045) approved all animal experiments.

Author contributions
GYY and ZJY designed the study. GYY, ZJY and LHR performed the experiments. GZ and SHY conducted the statistical analysis. GYY wrote the manuscript. All the authors have read and approved the final manuscript.

Conflict of interest
All authors claimed there was no conflict of interest.

Supplementary material
Supplementary materials are available on Journal's website.
Figure S1. MFN2 expression in HLE-B3 cells overexpressing or knocking down MFN2. A, B. HLE-B3 cells were transfected with lentivirus-mediated MFN2 overexpression vector or shRNA for 48 h, and RT-qPCR and western blot assays were performed to detect the MFN2 expression level as described in Methods section. **$P < 0.01$, MFN2-oe as Vector; ++$P < 0.01$, MFN2 shRNA as NC shRNA.

REFERENCES

1. Greenberg MJ, Bamba S. Diabetic cataracts. Dis Mon. 2021; 67(5): 101134, doi: 10.1016/j.disamonth.2021.101134, indexed in Pubmed: 33485606.
2. Obrosova IG, Chung SSM, Kador PF. Diabetic cataracts: mechanisms and management. Diabetes Metab Res Rev. 2010; 26(3): 172–180, doi: 10.1002/dmrr.1075, indexed in Pubmed: 20474067.
3. Peterson SR, Silva PA, Murtha TJ, et al. Cataract Surgery in Patients with Diabetes: Management Strategies. Semin Ophthalmol. 2018; 33(1): 75–82, doi: 10.1080/08820538.2017.1353817, indexed in Pubmed: 29144826.
4. Haddad NM, Sun JK, Abujaber S, et al. Cataract surgery and its complications in diabetic patients. Semin Ophthalmol. 2014; 29(5-6): 329–337, doi: 10.3109/08820538.2014.959197, indexed in Pubmed: 25325858.
5. Murtha T, Cavallerano J. The management of diabetic eye disease in the setting of cataract surgery. Curr Opin Ophthalmol. 2007; 18(1): 13–18, doi: 10.1097/ICU.0b013e32801129fc, indexed in Pubmed: 17159441.
6. Long AC, Agler A, Colitz CMH, et al. Isolation and characterization of primary canine lens epithelial cells. Vet Ophthalmol. 2008; 11(1): 38–42, doi: 10.1111/j.1463-5224.2007.00599.x, indexed in Pubmed: 18190351.
7. Su D, Hu S, Guan L, et al. Down-regulation of GJA3 is associated with lens epithelial cell apoptosis and age-related cataract. Biochem Biophys Res Commun. 2017; 484(1): 159–164, doi: 10.1016/j.bbrc.2017.01.050, indexed in Pubmed: 28088522.
8. Li WC, Kuszak JR, Dunn K, et al. Lens epithelial cell apoptosis appears to be a common cellular basis for non-congenital cataract development in humans and animals. J Cell Biol. 1995; 130(1): 169–181, doi: 10.1083/jcb.130.1.169, indexed in Pubmed: 7790371.
9. Li WC, Spector A. Lens epithelial cell apoptosis is an early event in the development of UVB-induced cataract. Free Radic Biol Med. 1996; 20(3): 301–311, doi: 10.1016/0891-5849(96)02050-3, indexed in Pubmed: 8720900.
10. Rovira-Llopis S, Bañuls C, Diaz-Morales N, et al. Mitochondrial dynamics in type 2 diabetes: Pathophysiological implications. Redox Biol. 2017; 11: 637–645, doi: 10.1016/j.redox.2017.01.013, indexed in Pubmed: 28131082.
11. Delmotte P, Sieck GC. Endoplasmic reticulum stress and mitochondrial function in airway smooth muscle. Front Cell Dev Biol. 2019; 7: 374, doi: 10.3389/fcell.2019.00374, indexed in Pubmed: 32010691.
12. Zorzano A, Hernández-Alvarez MI, Sebastián D, et al. Mitofusin 2 as a driver that controls energy metabolism and insulin signaling. Antioxid Redox Signal. 2015; 22(12): 1020–1031, doi: 10.1089/ars.2014.6208, indexed in Pubmed: 25567790.
13. Muñoz JP, Ivanova S, Sánchez-Wandelmer J, et al. Mfn2 modulates the UPR and mitochondrial function via repression of PERK. EMBO J. 2013; 32(17): 2348–2361, doi: 10.1038/emboj.2013.168, indexed in Pubmed: 23921556.
14. Tang WX, Wu WH, Zeng XXi, et al. Early protective effect of mitofusion 2 overexpression in STZ-induced diabetic rat kidney. Endocrine. 2012; 41(2): 236–247, doi: 10.1007/s12020-011-9555-1, indexed in Pubmed: 22095488.
15. Mi X, Tang W, Chen X, et al. Mitofusin 2 attenuates the histone acetylation at collagen IV promoter in diabetic nephropathy. J Mol Endocrinol. 2016; 57(4): 233–249, doi: 10.1530/JME-16-0031, indexed in Pubmed: 27997345.
16. Zhang R, Garrett Q, Zhou H, et al. Upregulation of miR-195 accelerates oxidative stress-induced retinal endothelial cell injury by targeting mitofusin 2 in diabetic rats. Mol Cell Endocrinol. 2017; 452: 33–43, doi: 10.1016/j.mce.2017.05.009, indexed in Pubmed: 28487236.
17. Zhao J, Wu X, Wu D, et al. Embryonic surface ectoderm-specific mitofusin 2 conditional knockout induces congenital cataracts in mice. Sci Rep. 2018; 8(1): 1522, doi: 10.1038/s41598-018-19849-2, indexed in Pubmed: 29367651.
18. Yang J, Wang T, Zhang Y, et al. Altered expression of mitofusin 2 in penile tissues of diabetic rats. Andrologia. 2014; 46(5): 522–528, doi: 10.1111/and.12108, indexed in Pubmed: 23682852.
19. Bahmani F, Bathaie SZ, Aldavood SJ, et al. Prevention of α-crystallin glycation and aggregation using l-lysine results in the inhibition of in vitro catalase heat-induced-aggregation and suppression of cataract formation in the diabetic rat. Int J Biol Macromol. 2019; 132: 1200–1207, doi: 10.1016/j.ijbiomac.2019.04.037, indexed in Pubmed: 30965074.
20. Zhao F, Maren NA, Kosentka PZ, et al. An optimized protocol for stepwise optimization of real-time RT-PCR analysis. Hortic Res. 2021; 8(1): 179–332, doi: 10.1038/s41438-021-00616-w, indexed in Pubmed: 34333545.
21. He L, Zhang N, Wang L, et al. Quercetin inhibits AQP1 translocation in high-glucose-cultured SRA01/04 cells through

21. PI3K/AKT/mTOR pathway. Curr Mol Pharmacol. 2021; 14(4): 587–596, doi: 10.2174/1874467213666200908120501, indexed in Pubmed: 32900356.

22. Li J, Sun Q, Qiu X, et al. Downregulation of AMPK dependent FOXO3 and TFEB involves in the inhibition of autophagy in diabetic cataract. Curr Eye Res. 2022; 47(4): 555–564, doi: 10.1080/02713683.2021.2009516, indexed in Pubmed: 34872443.

23. Kim J, Kim CS, Sohn E, et al. Lens epithelial cell apoptosis initiates diabetic cataractogenesis in the Zucker diabetic fatty rat. Graefes Arch Clin Exp Ophthalmol. 2010; 248(6): 811–818, doi: 10.1007/s00417-010-1313-1, indexed in Pubmed: 20162295.

24. Babizhayev MA, Yegorov YE. Reactive oxygen species and the aging eye: specific role of metabolically active mitochondria in maintaining lens function and in the initiation of the oxidation-induced maturity onset cataract--a novel platform of mitochondria-targeted antioxidants with broad therapeutic potential for redox regulation and detoxification of oxidants in eye diseases. Am J Ther. 2016; 23(1): e98–117, doi: 10.1097/MJT.0b013e3181ea31ff, indexed in Pubmed: 21048433.

25. Yao Ke, Ye P, Zhang Li, et al. Epigallocatechin gallate protects against oxidative stress-induced mitochondria-dependent apoptosis in human lens epithelial cells. Mol Vis. 2008; 14: 217–223, indexed in Pubmed: 18334937.

26. Li Yi, Jia Yi, Zhou J, et al. Effect of methionine sulfoxide reductase B1 silencing on high-glucose-induced apoptosis of human lens epithelial cells. Life Sci. 2013; 92(3): 193–201, doi: 10.1016/j.lfs.2012.11.021, indexed in Pubmed: 23270945.

27. Yu H, Hong X, Liu L, et al. Cordycepin decreases ischemia/reperfusion injury in diabetic hearts via upregulating ampk/mfn2-dependent mitochondrial fusion. Front Pharmacol. 2021; 12: 754005, doi: 10.3389/fphar.2021.754005, indexed in Pubmed: 34744731.

28. Hu L, Ding M, Tang D, et al. Targeting mitochondrial dynamics by regulating Mfn2 for therapeutic intervention in diabetic cardiomyopathy. Theranostics. 2019; 9(13): 3687–3706, doi: 10.7150/thno.33684, indexed in Pubmed: 31281507.

29. Hu Y, Chen H, Zhang L, et al. The AMPK-MFN2 axis regulates MAM dynamics and autophagy induced by energy stresses. Autophagy. 2021; 17(5): 1142–1156, doi: 10.1080/15548627.2020.1749490, indexed in Pubmed: 32249716.

30. Tur J, Pereira-Lopes S, Vico T, et al. Mitofusin 2 in macrophages links mitochondrial ROS production, cytokine release, phagocytosis, autophagy, and bactericidal activity. Cell Rep. 2020; 32(8): 108079, doi: 10.1016/j.celrep.2020.108079, indexed in Pubmed: 32846136.

31. Arruda AP, Hotamisligil GS, Fu S, et al. Phenotypic assays identify azoramide as a small-molecule modulator of the unfolded protein response with antidiabetic activity. Sci Transl Med. 2015; 7(292): 292ra98–397, doi: 10.1126/scitranslmed.aaa9134, indexed in Pubmed: 26084805.

32. Naón D, Hernández-Alvarez MI, Shinjo S, et al. Genes involved in mitochondrial biogenesis/function are induced in response to bilio-pancreatic diversion in morbidly obese individuals with normal glucose tolerance but not in type 2 diabetic patients. Diabetologia. 2009; 52(8): 1618–1627, doi: 10.1007/s00125-009-1403-y, indexed in Pubmed: 19504086.

33. Ding Y, Liu N, Zhang D, et al. Mitochondria-associated endoplasmic reticulum membranes as a therapeutic target for cardiovascular diseases. Front Pharmacol. 2024; 15: 1398381, doi: 10.3389/fphar.2024.1398381, indexed in Pubmed: 38694924.

34. de Brito O, Scorrano L. Mitofusin 2 tethers endoplasmic reticulum to mitochondria. Nature. 2008; 456: 605–610.

35. Cao Y, Chen Z, Hu J, et al. Mfn2 regulates high glucose-induced mams dysfunction and apoptosis in podocytes via PERK pathway. Front Cell Dev Biol. 2021; 9: 769213, doi: 10.3389/fcell.2021.769213, indexed in Pubmed: 34988075.

36. Barlow AD, Thomas DC. Autophagy in diabetes: β-cell dysfunction, insulin resistance, and complications. DNA Cell Biol. 2015; 34(4): 252–260, doi: 10.1089/dna.2014.2755, indexed in Pubmed: 25665094.

37. Tao T, Xu H. Autophagy and obesity and diabetes. Adv Exp Med Biol. 2020; 1207: 445–461, doi: 10.1007/978-981-15-4272-5_32, indexed in Pubmed: 32671767.

38. Clarke PGH, Puyal J. Autophagic cell death exists. Autophagy. 2012; 8(6): 867–869, doi: 10.4161/auto.20380, indexed in Pubmed: 22652592.

39. Fitzwalter BE, Thorburn A. Recent insights into cell death and autophagy. FEBS J. 2015; 282(22): 4279–4288, doi: 10.1111/febs.13515, indexed in Pubmed: 26367268.

40. Li Ji, Ye W, Xu W, et al. Activation of autophagy inhibits epithelial to mesenchymal transition process of human lens epithelial cells induced by high glucose conditions. Cell Signal. 2020; 75: 109768, doi: 10.1016/j.cellsig.2020.109768, indexed in Pubmed: 32896607.

41. Xue R, Meng Q, Lu Di, et al. Mitofusin2 induces cell autophagy of pancreatic cancer through inhibiting the PI3K/AKT/mTOR signaling pathway. Oxid Med Cell Longev. 2018; 2018: 2798070, doi: 10.1155/2018/2798070, indexed in Pubmed: 30046371.

ORIGINAL PAPER

VM
VIA MEDICA

Simvastatin suppresses ethanol effects on the kidney of adolescent mice

Makgotso Nchodu ⓘ**, Robin du Preez** ⓘ**, Alice Efuntayo** ⓘ**, Oladiran I Olateju** ⓘ

School of Anatomical Sciences, Faculty of Health Sciences, University of the Witwatersrand, Johannesburg, South Africa

Abstract

Introduction. Adolescents tend to experiment with ethanol which often results in heavy episodic drinking patterns leading to serious health concerns later in life. Chronic ethanol use damages renal tissue, promotes collagen deposition, and induces renal inflammation, thereby causing renal dysfunction. Therefore, an intervention such as simvastatin (a blood cholesterol-lowering drug) that could suppress the effects of ethanol on the kidney may be beneficial. This study explored the impact of simvastatin against the onset of renal morphological damage, fibrosis, and inflammation caused by ethanol exposure in mice.

Materials and methods. Ten four-week old C57BL/6J mice (F = 5; M = 5) were assigned to each experimental group: (I) NT; no administration of ethanol or simvastatin; (II) EtOH; 2.5 g/kg/day of 20% ethanol, intraperitoneal injection (*i.p.*); (III) SIM; 5 mg/kg/day of simvastatin, orally; (IV) EtOH + SIM5; 5 mg/kg/day of simvastatin, orally, followed by 2.5 g/kg/day of 20% ethanol, *i.p.*; and (V) EtOH + SIM15; 15 mg/kg/day of simvastatin, orally, followed by 2.5 g/kg/day of 20% ethanol, *i.p.* After the 28-day treatment period, the right kidney was removed and processed for haematoxylin and eosin staining, Masson's trichrome staining, or tumour necrosis factor-alpha (TNF-α) immunohistochemistry. The renal corpuscular area, glomerular area, and urinary space area were measured and the area of collagen or TNF-α expression was quantified using ImageJ software.

Results. Ethanol administration significantly increased the renal corpuscular area, the glomerular area, the area of collagen, and the area of tissue with TNF-α immunoreactivity but decreased the area of urinary space. Simvastatin generally suppressed the ethanol effects in both sexes, although to varying degrees.

Conclusions. Simvastatin proved to suppress collagen deposition and the TNF-α production induced by ethanol in the kidney of mice thus indicating its effectiveness in the treatment of ethanol-related renal diseases. (*Folia Histochem Cytobiol 2024; 62, 2: 87–95*)

Keywords: ethanol; kidney; simvastatin; fibrosis; TNF-alpha; sex effect

INTRODUCTION

Apart from the regulation of body fluid and mineral homeostasis, the kidneys play an important role in the control of blood pressure [1]. They are also responsible for filtering and excreting ethanol and its metabolites from the body [2], making the kidneys highly vulnerable to damage caused by excessive ethanol consumption [3]. Due to the function of the kidneys, damage or loss of function could negatively affect the functions of other organs, especially the heart [4]. It is proven that chronic consumption of ethanol increases the incidence of cardiovascular diseases [5, 6] by increasing blood pressure through various mechanisms, one of which is the activation of the renin-angiotensin system (RAS) in the kidney where a rise in systemic blood pressure causes glomerular hypertension and vasoconstriction [1]. The activated intrarenal RAS induced by chronic ethanol use also promotes renal damage by altering the morphologies of the glomeruli, tubules, and renal blood vessels [1, 7, 8]. Simultaneously, it prolongs hypertension

Correspondence address:

Oladiran I. Olateju
School of Anatomical Sciences, Faculty of Health Sciences,
University of the Witwatersrand, 7 York Road, Parktown, 2193,
Johannesburg, Republic of South Africa
tel. +27 11 717 2763; fax: +27 11 717 2422
e-mail: Oladiran.Olateju@wits.ac.za

which is detrimental to the heart and other organs [1, 9]. This interrelationship between the heart and the kidneys shows that the severity of cardiovascular disease increases the probability of renal disease and *vice versa* [8]. Unfortunately, chronic ethanol consumption is a social problem among adolescents as they tend to experiment with ethanol, often resulting in heavy episodic drinking patterns, especially in places where there are lapses in the regulation of access to ethanol [10–12]. Ethanol misuse is higher in male than in female adolescents and these adolescents often become ethanol addicts later in life thus contributing to social, economic, and health problems [5, 11–15].

Ethanol-induced renal damage changes the morphologies of the renal structures, *e.g.* the glomeruli and renal tubules. This causes renal functions such as glomerular filtration and tubular reabsorption to fail [2, 4, 7, 16, 17]. At the same time, chronic ethanol use inhibits the function of antidiuretic hormone (ADH) in the kidneys thus resulting in the loss of water from the body [17]. Likewise, extracellular matrix deposition (*i.e.* renal fibrosis) between the renal tubules and surrounding capillaries may increase in response to chronic ethanol use, delaying the oxygen supply and nutrients to the renal tubular cells [2].

Tumour necrosis factor-alpha (TNF-α) is produced in the kidney by endothelial, mesangial, and renal tubular epithelial cells [9, 18]. The basal interstitial level of TNF-α is considerably low or undetectable under normal conditions but it sporadically increases at the onset of inflammation. TNF-α can also induce apoptosis which may be beneficial or detrimental to renal tissues as apoptosis may contribute to the pathogenesis of renal diseases such as acute renal failure or may trigger cell proliferation to compensate for glomerular or tubular cell loss in glomerular or tubular disease [19].

With the plethora of effects of simvastatin on the cardiovascular system, it is envisaged that the ability of simvastatin (an FDA-approved blood cholesterol-lowering drug [20–23]) to prevent inflammation, regulate immune-responses, prevent cell death and fibrosis in diseases associated with a failing cardiovascular system [24–27] may also be of benefit against ethanol-induced renal damage. This study, therefore, explored the effects of simvastatin against ethanol-induced renal damage, fibrosis, or inflammation by analysing the morphology and morphometry of renal structures, quantifying the area of collagen and the area of TNF-α expression in the renal tissue of adolescent mice that were administered ethanol. Results of this study may provide new cues on the protective effects of simvastatin against ethanol-induced damage in the kidneys and may also provide additional evidence of its suitability for the treatment of alcohol-related renal diseases.

MATERIALS AND METHODS

Animals and study design

Animal ethics approval was granted (Ethics Clearance No: 2019/11/63/C) by the Animal Research Ethics Committee (AREC) of the University of the Witwatersrand, Johannesburg, South Africa. Mice of the same sex and belonging to the same experimental group were housed together in a group of five mice per cage (cage dimensions: $200 \times 200 \times 300$ mm) and kept under a reversed 12-hour day/12-hour dark cycle (with the light switched off from 06:00 to 18:00). For this study, the period of adolescence in the mice was taken as between 3–8 weeks old [28].

Ten four-week old (adolescent) C57BL/6J mice (F = 5; M = 5) housed in the Witwatersrand Research Animal Facility (WRAF), University of the Witwatersrand, were assigned to each experimental group: (I) non-treatment group (NT) — no administration of ethanol or simvastatin; (II) Ethanol only group (EtOH) — 2.5 g/kg/day of 20% ethanol *via* intraperitoneal injection (*i.p.*); (III) simvastatin only group (SIM) — 5 mg/kg/day by oral gavage; (IV) ethanol and 5 mg simvastatin (EtOH + SIM5) — 5 mg/kg/day of simvastatin by oral gavage followed by 2.5 g/kg/day of 20% ethanol *via i.p.* administration; (V) ethanol + 15 mg simvastatin (EtOH + SIM15) — 15 mg/kg/day of simvastatin by oral gavage followed by 2.5 g/kg/day of 20% ethanol *via i.p.* administration. The percentage concentration of ethanol used in this study was similar to the range used by Cardoso de Sousa *et al.* [29]. An intraperitoneal injection of ethanol is commonly used in ethanol-related studies to generate a high blood ethanol concentration (see review by Patten *et al.* [30]). In addition, the concentrations of simvastatin used were also within the range used by Mohammadi *et al.* [31]. A stock solution of simvastatin (Cat no: 1612700, Merck, South Africa) was prepared by dissolving 8 mg simvastatin in a solution of 100 μL ethanol (to increase solubility), 100 μL 0.1 M NaOH (emulsifier) and 800 μL distilled water similarly as described by McKay *et al.* [32]. In addition, a pharmacological grade ethanol (96%) (Sigma-Aldrich, South Africa; Cat no: SAAR-2233510LP) was serially diluted in saline (0.9% NaCl) to obtain a 20% ethanol solution. Both simvastatin and ethanol were prepared daily and then filter sterilized before being administered. Any unused solution on the day was discarded. All treatments were performed for 28 consecutive days. Oral gavage and intraperitoneal injections were performed with the utmost care by the trained staff of WRAF to reduce the introduction of stress into the animal.

On the last day of treatment, blood alcohol concentration (BAC) was determined from saphenous blood (50 μL) collected within 30 min after the administra-

tion of ethanol in each mouse (*i.e.* mice in the ETOH, ETOH + SIM5 or ETOH + SIM15 experimental groups). The BAC in the extracted serum was analysed using an EnzyChrom™ Ethanol Assay Kit (BioVision, Sandton, South Africa). The average BAC level was in the range of 182.5–253.4 mg/dL for the groups that received ethanol. Following blood collection, the mice were euthanized using Euthanaze (sodium pentobarbital, 80 mg/kg, *i.p.*). Then, the mice were transcardially perfused with 20 mL 4% paraformaldehyde (PFA) (in 0.1 M phosphate buffer, PB), the right kidney was then removed and further fixed in 4% buffered PFA at 4°C before further processing.

Processing of the kidney

The kidney was cut horizontally at its equator whereafter the inferior half of the tissue was dehydrated in a graded series of ethanol, cleared in xylene, and then embedded in paraffin wax. The tissue block was sectioned at 5 μm thickness and one in three series of sections was collected for haematoxylin and eosin (H&E) staining (for general morphology and morphometry of renal corpuscles and the glomeruli). The second series of sections was prepared for Masson's trichrome (MT) staining (for evaluating the area of collagen) and the third series of sections was for TNF-α immunohistochemistry (for quantifying the area of TNF-α expression in the renal corpuscles or renal tubules). In total, four sets of one in three series of sections were collected. A 50 μm-thick section was wasted after each set of series to minimize analysing the same area of the section.

Immunohistochemistry

For TNF-α immunohistochemistry, a citrate antigen retrieval was performed by immersing the sections in citrate buffer (pH 6) at 60°C overnight. Thereafter, endogenous peroxidase activity was blocked by immersing the sections in 1% hydrogen peroxide, 49.5% methanol and 49.5% 0.1 M PB for 30 min. Subsequently, the sections were washed twice in 0.1 M PB before incubating in a blocking buffer (5% normal goat serum in 0.1 M PB) for 30 min to block unspecified binding sites. Thereafter, the sections were incubated overnight at 4°C in the primary antibody (1:250, mouse anti--TNF-α, ab220210, Abcam, Cambridge, United Kingdom) to quantify the area of tissue that expressed TNF-α immunoreactivity (TNFα-IR) The sections were then washed twice in 0.1 M phosphate-buffered saline before incubating in the secondary antibody (1:1000, goat anti-mouse IgG, BA-9200-1.5, Vector labs). Following incubation, the sections were washed twice in PB before incubating in an avidin-biotin solution (1:125; Vector Labs) for 1 h. The sections were further washed twice in PB and then the sections were developed by immersing them in a solution containing 0.05% DAB (3,3'-diaminobenzidine), 2 mL Tris HCl, 29 μL cold distilled water, and 1 μL hydrogen peroxide for 10 mins. The DAB reaction was terminated by adding an equal volume of 0.1 M PB before counterstaining with haematoxylin.

Histomorphometry

For the morphometry of renal structures, the renal corpuscles that were visible within a field of view at the 10× objective lens (obtained by moving the stage at every 1-mm interval along the width of the renal cortex of H&E-stained sections) were used for the morphometry. Each renal corpuscle within this field of view was then photographed at the 63× objective lens using a Carl Zeiss Axiocam camera (Serial No. 5318003446, Shanghai, China) attached to a Carl Zeiss Axioskop microscope (Serial No. 804161, Germany). With the scale set on ImageJ 1.47v software (NIH, Bethesda, MD, USA), the areas of the renal corpuscle and the glomerulus were measured from the digitized images by tracing the boundary of the parietal layer of the Bowman's capsule and the boundary of the glomerulus using the freehand tool of the software. The area of Bowman's space was then calculated by subtracting the area of the glomerulus from the area of the renal corpuscle [33].

To determine the area of collagen in the kidney tissue, digitized images of the MT-stained sections were taken using a Carl Zeiss Axiocam camera attached to a Carl Zeiss Axioskop microscope at times 40× objective lens. The images were subsequently saved in a JPEG file format. The field of view was changed by moving the microscope stage along the width of the renal cortex to prevent duplicating measurements. The area of stained collagen within the kidney was determined using the deconvolution plugin settings of ImageJ software [34, 35]. The 24-bit RGB format was selected as a requirement for the deconvolution plugin setting in the software where the green component on the processed image indicated collagen staining [34, 35]. The area of stained collagen on each image was quantified using the threshold tool on the software which was adjusted until all the collagen (*i.e.* green-stainable) structures had been highlighted [34, 35]. The percentage area of collagen *per* image was calculated as the threshold area divided by the area of the image.

Similar to the analyses used for MT-stained sections, the percentage area of tissue with TNFα-IR in the renal tubules or the renal corpuscles was performed using digitized images at the 63× objective lens. The renal tubules or renal corpuscles were identified and photographed along the width of the renal cortex to prevent duplicating measurements. The digitized

images were saved in a JPEG file format before being analysed by ImageJ software. Using the 24-bit RGB format, the region of interest (ROI) manager was used to select the renal corpuscle or the renal tubules on an image. The size of the ROI (620368 μm^2) was kept constant throughout the analyses [36]. DAB staining was selected for the deconvolution plugin setting on the ImageJ software where the brown component was identified as the DAB staining. The area of tissue that expressed TNF-α in each ROI was quantified by adjusting the threshold tool of the software until all the DAB stains had been highlighted [36]. Thereafter, the percentage area of tissue with TNFα-IR was determined by dividing the threshold area by the area of the ROI. Throughout the analyses, the experimenter was blinded to the experimental groups and an inter-observer test was satisfactory.

Statistical analysis

Descriptive statistics using the mean and standard deviation (SD), or the median were performed. Normality test was conducted using the Shapiro-Wilk test and then either One-Way ANOVA or Kruskal-Wallis test was conducted to compare the mean or median of the measurements across the different groups. A *post hoc* test using either a Tukey's or a Dunn's test was conducted to determine where significant difference lies between any two groups. All statistical tests were performed using a PAST freeware data analyser (version 4.03; Germany) and boxplots were plotted using Excel software (Word Office Pro, Redmond, WA, USA). A statistical difference of 5% was regarded as significant for all statistical analyses (P < 0.05).

RESULTS

Kidney and body mass and morphology of the kidney

The average kidney mass, body mass and kidney//body mass ratio of the mice across the different experimental groups for both sexes are shown in Table 1. The average kidney mass, the average body mass or the kidney/body mass ratio was similar across the experimental groups for both sexes. In addition, all the mice in the different experimental groups gained body mass, for both sexes.

The morphology of the tissue was typical of the normal histology of the renal tissue of the mouse. The renal corpuscles and the renal tubules were distinct and abundant in the renal cortex across the different

Table 1. Mean kidney mass, mean body mass and kidney/body mass ratio of female and male mice across the experimental groups

	NT	SIM	EtOH	EtOH + SIM5	EtOH + SIM15	P
Female						
Kidney mass at day 28 [g]	0.162 ± 0.013	0.151 ± 0.028	0.169 ± 0.017	0.149 ± 0.039	0.183 ± 0.015	0.203
Body mass at day 1 [g]	12.500 ± 0.791	12.800 ± 0.758	12.600 ± 0.822	12.000 ± 0.935	12.700 ± 0.274	0.652
Kidney/body mass ratio at day 1	0.014 ± 0.001	0.012 ± 0.002	0.013 ± 0.001	0.012 ± 0.004	0.014 ± 0.001	0.311
Body mass at day 28 [g]	14.500 ± 1.581	14.800 ± 1.151	14.600 ± 1.245	13.900 ± 1.025	15.300 ± 1.891	0.639
Kidney/body mass ratio at day 28	0.012 ± 0.001	0.010 ± 0.003	0.012 ± 0.002	0.010 ± 0.003	0.012 ± 0.001	0.493
Male						
Kidney mass at day 28 [g]	0.162 ± 0.016	0.158 ± 0.010	0.177 ± 0.014	0.181 ± 0.016	0.177 ± 0.031	0.240
Body mass at day 1 [g]	15.300 ± 0.975	14.300 ± 1.304	14.400 ± 2.162	14.400 ± 0.742	13.700 ± 1.255	0.330
Kidney/body mass ratio at day 1	0.011 ± 0.002	0.012 ± 0.001	0.013 ± 0.003	0.013 ± 0.001	0.013 ± 0.003	0.438
Body mass at day 28 [g]	18.900 ± 1.673	18.400 ± 1.636	18.000 ± 1.658	18.100 ± 0.548	15.900 ± 1.387	0.072
Kidney/body mass ratio at day 28	0.009 ± 0.001	0.010 ± 0.002	0.010 ± 0.001	0.010 ± 0.001	0.011 ± 0.002	0.149

The values express mean ± SD (standard deviation). P indicates statistical difference (at 0.05) using One-Way ANOVA (parametric) or Kruskal-Wallis (non-parametric). There was no significant difference for all the measurements across the experimental groups. Abbreviations: NT — non-treatment (control) groups; SIM — 5 mg simvastatin; EtOH — ethanol; EtOH + SIM5 — 5 mg simvastatin and EtOH; EtOH + SIM15 — 15 mg simvastatin and EtOH.
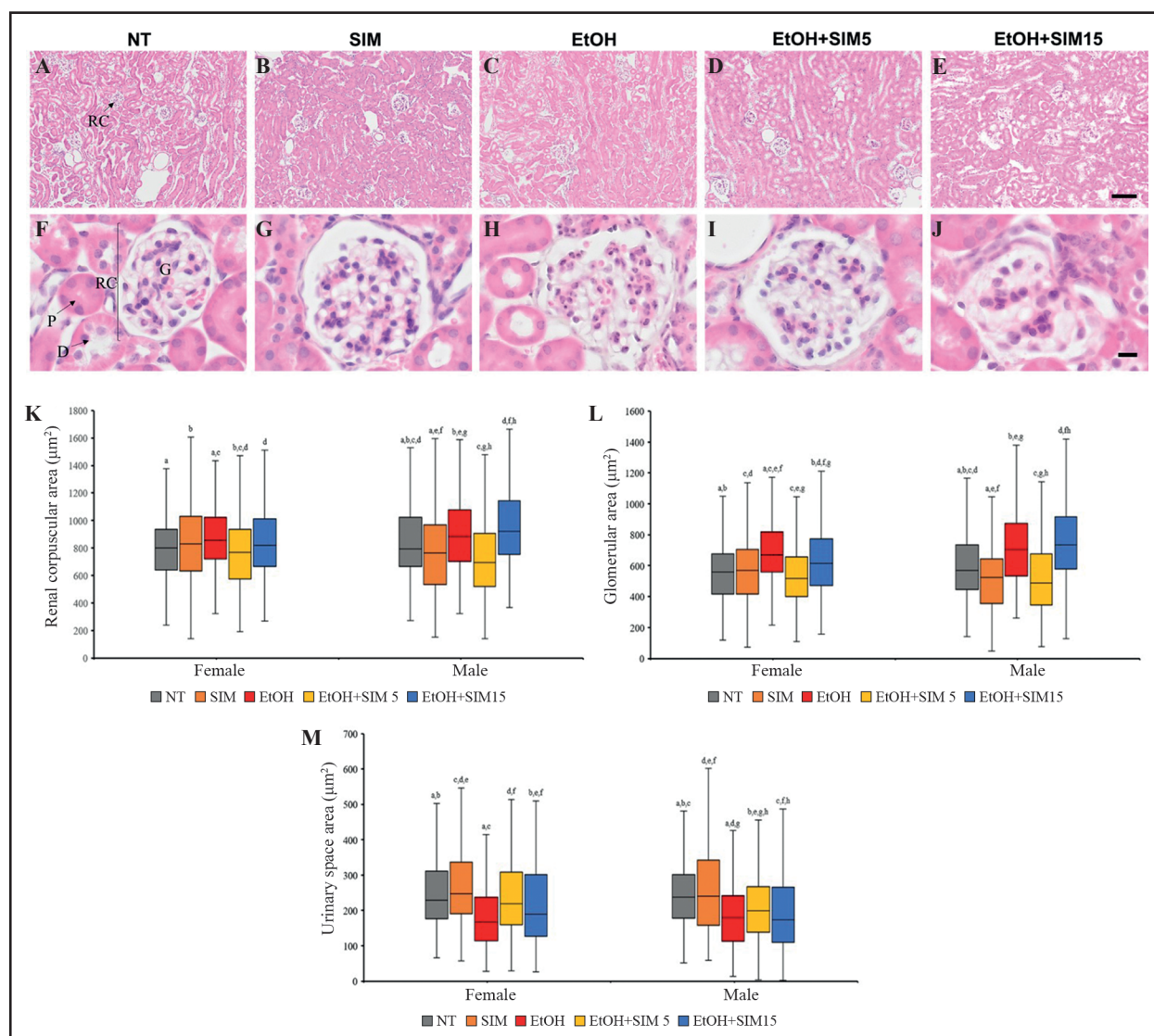
Figure 1. Representative photomicrographs of the H&E-stained sections of female and male mouse kidneys (**A–E**) at the low magnification (scale bar: 100 μm) and (**F–J**) at the high magnification (scale bar: 10 μm) as well as the box plots of the median values of: (**K**) kidney corpuscular area, (**L**) glomerular area, and (**M**) urinary space area across the different experimental groups. The renal morphology was typical of the normal histology of the mouse kidney with the renal corpuscles (RC), glomeruli (G), distal (D) and proximal (P) kidney tubules present in the renal cortex. In both sexes, ethanol increased the renal corpuscular and glomerular areas but decreased the urinary space area in the renal tissue. In both sexes, 5 mg simvastatin reduced the ethanol effect on the renal corpuscular and glomerular areas and increased the urinary space area. Abbreviations: NT — non-treatment (control group); SIM5 — 5 mg simvastatin; EtOH — ethanol; EtOH + SIM5 — 5 mg simvastatin and EtOH; EtOH + SIM15 — 15 mg simvastatin and EtOH; H & E — haematoxylin and eosin staining; RC — renal corpuscle; G — glomeruli; D — distal convoluted tubule; P — proximal convoluted tubule. The same letters indicate differences between paired groups that are statistically significantly different at P < 0.05.

experimental groups (Fig. 1A–J). Interstitial fibrosis was scanty in the MT-stained sections of the NT or the SIM group but not in the experimental groups that were administered ethanol (EtOH, EtOH + SIM5, or EtOH + SIM15) (Fig. 2A–J). Collagen staining was most noticeable in the EtOH group (Fig. 2C, H). Likewise, the area of tissue that expressed TNF-α immunoreactivity (Fig. 3A–J) in the extracellular matrix was most conspicuous in the renal corpuscles and the renal tubules of the EtOH group (Fig. 3C and H).

Morphometry of the renal corpuscular area

In the females, the renal corpuscular area was highest in the EtOH group and lowest in the EtOH + SIM5 group (Table 2; Fig. 1K). The renal corpuscular area was significantly different across the experimental groups (P = 0.000). A *post hoc* test revealed that the renal corpuscular area was significantly higher in the EtOH group than in the NT group (P = 0.001) or the EtOH + SIM5 group (P = 0.000). However, the area of renal corpuscle was similar in the NT *vs.* SIM
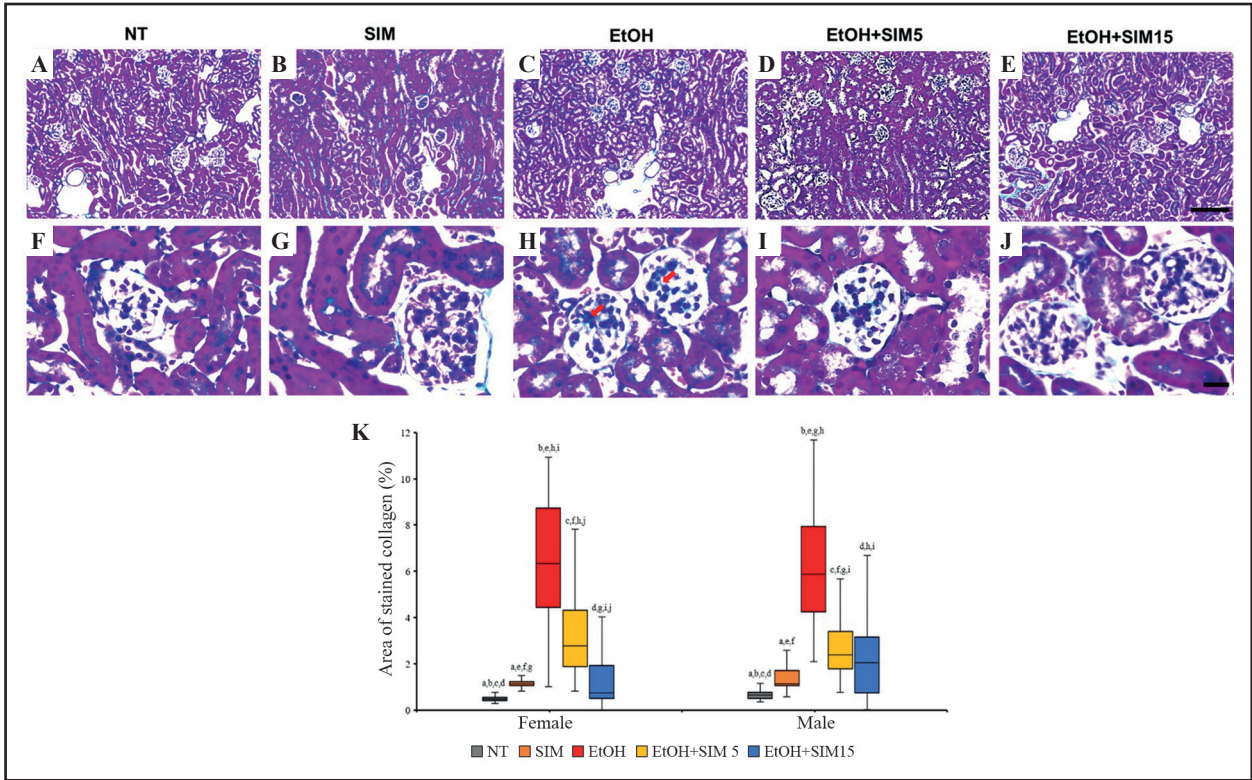
Figure 2. Representative photomicrographs of the sections of mouse kidney stained by Masson trichrome method (**A–E**) at the low magnification (scale bar: 100 μm) and (**F–J**) at the high magnification (scale bar: 20 μm) as well as the box plots of the median values of: (**k**) area of stained collagen across the different experimental groups, for both sexes. Interstitial fibrosis in the glomerulus and tubule (indicated by red arrows) was abundant in the EtOH group (C and H). In both sexes, the area of stained collagen was significantly higher in the ethanol-treated mice than in the NT groups. Both concentrations of simvastatin significantly reduced the ethanol effect on the area of stained collagen in the kidney. Abbreviations: NT — non-treatment (control group); SIM5 — 5 mg simvastatin; EtOH — ethanol; EtOH + SIM5 — 5 mg simvastatin and EtOH; EtOH + SIM15 — 15 mg simvastatin and EtOH; MT — Masson's trichrome staining. The same letters indicate differences between paired groups that are statistically significantly different at P < 0.05.

Table 2. The area of the renal corpuscle, the glomerular area, and the urinary space area in the kidney of female and male mice across the experimental groups

	No of animals	No of renal structures assessed	Renal corpuscular area	Glomerular area	Urinary space area
			Mean [μm^2]	Mean [μm^2]	Mean [μm^2]
Female					
NT	5	269	845 ± 381	578 ± 261	268 ± 163
SIM	5	269	858 ± 337	574 ± 231	283 ± 148
EtOH	5	268	903 ± 306	710 ± 243	193 ± 113
EtOH + SIM5	5	270	787 ± 291	545 ± 218	243 ± 122
EtOH + SIM15	5	262	881 ± 330	643 ± 241	238 ± 160
Male					
NT	5	259	857 ± 307	601 ± 236	256 ± 116
SIM	5	260	809 ± 415	529 ± 262	280 ± 185
EtOH	5	265	918 ± 288	726 ± 246	191 ± 103
EtOH + SIM5	5	269	755 ± 352	525 ± 254	230 ± 144
EtOH + SIM15	5	264	967 ± 314	755 ± 243	212 ± 144

The values express mean ± SD (standard deviation). Abbreviations: NT — non-treatment (control) groups; SIM — 5 mg simvastatin; EtOH — ethanol; EtOH + SIM5 — 5 mg simvastatin and EtOH; EtOH + SIM15 — 15 mg simvastatin and EtOH.
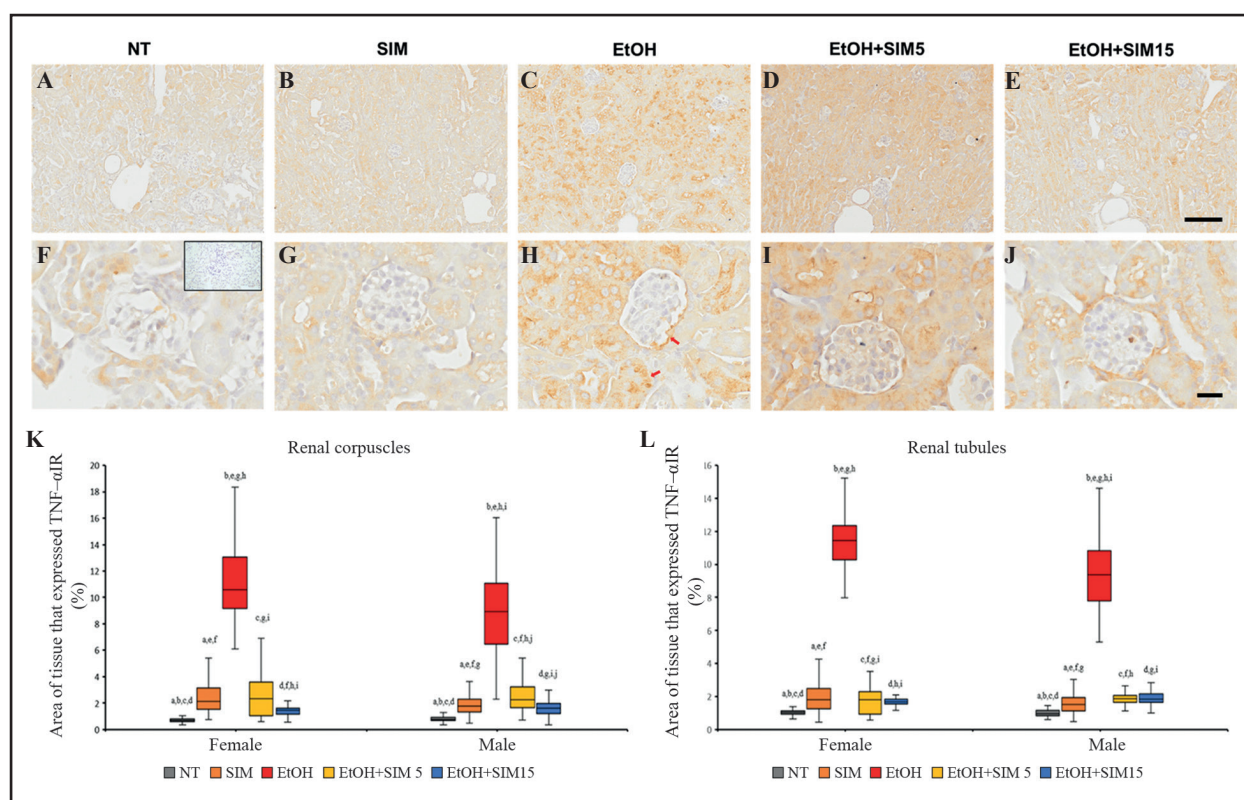
Figure 3. Representative photomicrographs of the area of mouse kidneys that expressed TNF-α IR (**A–E**) at the low magnification (scale bar: 100 μm) and (**F–J**) at the high magnification (scale bar: 20 μm) as well as the box plots of the median values of area of kidney with TNF-α IR in (a) the kidney corpuscles and (b) the kidney tubules across the different experimental groups, for both sexes. TNF-α IR in the glomeruli and the kidney tubules are indicated by the red arrows (b). The inset in (a) illustrates the reagent control where the primary antibody was omitted. In both sexes, the area of tissue that expressed TNF-α IR was significantly higher in the EtOH groups than in the NT groups in regard to the renal corpuscles and tubules. Both concentrations of simvastatin significantly reduced the ethanol effect on the area of tissue that expressed TNF-α IR in the kidney corpuscles or the tubules. Abbreviations: NT — non-treatment (control group); SIM5 — 5 mg simvastatin; EtOH — ethanol; EtOH + SIM5 — 5 mg simvastatin and EtOH; EtOH + SIM15 — 15 mg simvastatin and EtOH; TNF-α IR — Tumour Necrosis Factor-alpha immunoreactivity. The same letter indicates paired groups that are statistically significantly different at P < 0.05.

(P = 0.155), the NT *vs.* EtOH + SIM5 (P = 0.132), SIM *vs.* EtOH (P = 0.073) or EtOH *vs.* EtOH + SIM15 groups (P = 0.1409) (Fig. 1K). In the male mice, the renal corpuscular area was highest in the EtOH+SIM15 group and lowest in the EtOH+SIM5 group (Table 2; Fig. 1K). The renal corpuscular area was significantly different across the experimental groups (P = 0.000) and a *post hoc* test revealed that the renal corpuscular area in any paired groups was significantly different except the SIM *vs.* EtOH + SIM5 (P = 0.058) or EtOH *vs.* EtOH + SIM15 (P = 0.117) groups (Fig. 1K).

Morphometry of the glomerular area

In the female mice, the glomerular area was highest in the EtOH group and lowest in the EtOH + SIM5 group (Table 2; Fig. 1L). The glomerular area was significantly different across the experimental groups (P = 0.000) and a *post hoc* test revealed that the glo-

merular area in any paired groups was significantly different except the NT *vs.* SIM (P = 0.557), the NT *vs.* EtOH + SIM5 (P = 0.188), or the SIM *vs.* EtOH + SIM5 (P = 0.057) groups (Fig. 1L). In addition, the glomerular area was significantly higher in the EtOH group than in the NT (P = 0.000), SIM (P = 0.000), EtOH + SIM5 (P = 0.000) or EtOH + SIM15 groups (P = 0.001). In the male mice, the glomerular area was highest in the EtOH + SIM15 group and lowest in the EtOH + SIM5 group (Table 2, Fig. 1L). The glomerular area was significantly different across the experimental groups (P = 0.000). A *post hoc* test revealed that the area of the glomerulus in any paired groups was significantly different except for the SIM *vs.* EtOH + SIM5 (P = 0.856) or the EtOH *vs.* EtOH + SIM15 groups (P = 0.139) (Fig. 1L). In addition, the glomerular area was significantly higher in the EtOH group than in the NT (P = 0.000), SIM (P = 0.000) or EtOH + SIM5 groups (P = 0.000).

Morphometry of the urinary space area

The urinary space area was highest in the SIM group and lowest in the EtOH group for both sexes (Table 2; Fig. 1M). In the females, the urinary space area was significantly different across the experimental groups (P = 0.000). A *post hoc* test revealed that the urinary space area was significantly lower in the EtOH group than in the NT (P = 0.000), SIM (P = 0.000), EtOH + SIM5 (P = 0.000) or EtOH + SIM15 groups (P = 0.001). However, there was no significant difference in the urinary space area in NT *vs.* SIM (P = 0.085) or NT *vs.* EtOH + SIM5 groups (P = 0.101) (Fig. 1M). In the male mice, the urinary space area was significantly different across the experimental groups (P = 0.000). A *post hoc* test revealed that the urinary space area was significantly lower in the EtOH group than in the NT (P = 0.000), SIM (P = 0.000), or EtOH + SIM5 groups (P = 0.005) but not in NT *vs.* SIM (P = 0.687) or EtOH *vs.* EtOH + SIM15 (P = 0.449) groups (Fig. 1M).

Percentage area of collagen in the kidney

The percentage area of stained collagen in the kidney was highest in the EtOH group and lowest in the NT group for both sexes (Table 3, Fig. 2K). In the female mice, the percentage area of stained collagen was significantly different across the experimental groups (P = 0.000). A *post hoc* test revealed that the percentage area of stained collagen was significantly higher in the EtOH group than in the NT (P = 0.000), SIM (P = 0.000), EtOH + SIM5 (P = 0.000), or EtOH + SIM15 groups (P = 0.000) (Fig. 2K). The significant difference between EtOH *vs.* NT demonstrates ethanol-induced collagen production in the kidney. Both concentrations of simvastatin significantly suppressed collagen production induced by ethanol, but the higher simvastatin concentration (15 mg) seems to be more effective.

In the males, the percentage area of stained collagen was significantly different across the experimental groups (P = 0.000) and a *post hoc* test revealed that the percentage area of stained collagen was significantly higher in the EtOH group than in the NT (P = 0.000), SIM (P = 0.000), EtOH + SIM5 (P = 0.000), or EtOH + SIM15 groups (P = 0.000) except in SIM *vs.* EtOH + SIM15 groups (P = 0.163) (Fig. 2K). The significant difference between the EtOH *vs.* NT groups also demonstrates ethanol-induced renal production of collagen. Similar to the females, both concentrations of simvastatin suppressed collagen production induced by ethanol in the renal tissues in the males, but the higher simvastatin concentration (15 mg) seems to be more effective.

Percentage area of tissue that expressed TNF-α immunoreactivity

The percentage area of tissue that expressed TNF-α in the renal corpuscle or the renal tubule was highest in the EtOH group and was lowest in the NT group

Table 3. The percentage area of Masson trichrome-stained collagen and the area of tissue that expressed TNF-α immunoreactivity in the kidney of female and male mice across the experimental groups

| | No of animals | Area of stained collagen | | Area of tissue that expressed TNF-α IR | | | |
| | | | | Renal tubules | | Renal corpuscles | |
		No of images assessed	Mean [%]	No of ROIs assessed	Mean [%]	No of ROIs assessed	Mean [%]
Female							
NT	5	260	0.51 ± 0.14	205	1.03 ± 0.15	224	0.70 ± 0.15
SIM	5	260	1.48 ± 1.22	215	1.93 ± 0.84	202	2.39 ± 1.09
EtOH	5	231	6.52 ± 2.60	225	11.04 ± 1.54	252	11.13 ± 2.71
EtOH + SIM5	5	259	3.18 ± 1.73	252	1.69 ± 0.78	249	2.56 ± 1.60
EtOH + SIM15	5	257	1.35 ± 1.44	246	1.67 ± 0.20	242	1.41 ± 0.33
Male							
NT	5	260	0.67 ± 0.21	217	1.00 ± 0.21	201	0.79 ± 0.20
SIM	5	259	1.81 ± 1.66	184	1.56 ± 0.54	170	1.84 ± 0.66
EtOH	5	258	6.13 ± 5.87	248	9.51 ± 2.02	252	8.94 ± 2.92
EtOH + SIM5	5	255	2.78 ± 1.41	252	1.85 ± 0.30	252	2.48 ± 1.05
EtOH + SIM15	5	261	2.13 ± 1.49	252	1.90 ± 0.37	252	1.58 ± 0.57

The values express mean ± SD (standard deviation). Abbreviations: NT — non-treatment (control) groups; SIM — 5 mg simvastatin; EtOH — ethanol; EtOH + SIM5 — 5 mg simvastatin and ethanol; EtOH + SIM15 — 15 mg simvastatin and ethanol; ROI — Region of interest; TNF-α IR — Tumour necrosis factor-alpha immunoreactivity.

for both sexes (Table 3, Fig. 3K, L). In the females, a Kruskal-Wallis test revealed that the percentage area of tissue immunoreactive for TNF-α was significantly different across the experimental groups (P = 0.000) while a Dunn's *post hoc* revealed that the percentage area of tissue that showed TNF-α immunoreactivity in any paired groups was significantly different except the SIM *vs.* EtOH + SIM5 groups (P = 0.200) for the renal corpuscles (Fig. 3K) or the SIM *vs.* EtOH + SIM15 groups (P = 0.453) for the renal tubules (Fig. 3L). The significant difference between the EtOH *vs.* NT also demonstrates ethanol-induced TNF-α production in the renal tissue and both concentrations of simvastatin reduced ethanol-induced TNF-α production in the renal tissue.

In the male mice, the percentage area of tissue that expressed TNF-α was significantly different across the experimental groups (P = 0.000) while a *post hoc* test revealed that the percentage area of TNF-α production in the renal tissue in any paired groups for the renal corpuscles or the renal tubules was significantly different except in the EtOH + SIM5 *vs.* EtOH + SIM15 groups (P = 0.733) for the renal tubule in the male (Fig. 3L). The significant difference between the EtOH *vs.* NT groups also confirms ethanol-induced TNF-α production in the renal tissue and both concentrations of simvastatin were also effective in reducing ethanol--induced inflammation in the renal tissue.

DISCUSSION

Chronic ethanol use damages renal tissues in diverse ways. It promotes the accumulation of inflammatory cells to infiltrate the interstitial tissue. Even though this is essential for triggering a repair process, prolonged accumulation of inflammatory cells and pro-inflammatory cytokines hinders the repair process which then progresses to renal disease [37, 38]. Structural renal damage such as tubular epithelial cell atrophy, renal interstitial oedema, and tubular interstitial fibrosis suppress renal function [2, 7]. Kidney tubular cell injury and apoptosis also disrupt the selective reabsorption of molecules [16, 17]. Furthermore, fluid and mineral homeostasis is also disrupted as the secretion of antidiuretic hormone (ADH) is hindered by chronic ethanol use due to the renal collecting tubules becoming impermeable to water leading to electrolyte imbalance [17, 39]. Chronic ethanol consumption results in the thickening of the glomerular basement membrane, increased proliferation of mesangial cells, and swelling of the glomeruli, thereby leading to renal dysfunction [7].

Our study revealed that prolonged ethanol administration to young adult mice enlarged the size of the glomeruli with a corresponding decrease in urinary space. These outcomes seem to be ethanol-specific because increased glomerular capillaries favour glomerular hyperfiltration with a resultant urinary space dilation owing to the high hydrostatic pressure gradient in the glomeruli. A dilated urinary space results in a reduced urinary space pressure which is expected to maintain a glomerular hyperfiltration by sustaining a high transcapillary hydrostatic pressure gradient in the glomerular capillaries [40–42]. The failure of an 'envisaged' urinary space dilation to cope with glomerular hyperfiltration may therefore lead to upstream loss of parietal epithelial cells [41] which may trigger narrowing of glomerular capillaries causing synechiae formation in glomerulosclerosis [41, 43]. According to Tobar *et al.* [41], a dilated urinary space protects against the damage that could arise from high-pressure glomerular hyperfiltration. In the present study, glomerular hypertrophy induced by ethanol reduced the size of urinary space which seems to suggest ethanol--specific renal damage. Unfortunately, the extent of the renal damage by ethanol could not be elucidated in the present study.

Ethanol is also implicated in promoting extracellular matrix build-up (*i.e.* fibrosis) in the renal interstitium surrounding the tubules and capillaries. At the early stages of renal injury, myofibroblasts are stimulated by the inflammatory cytokines to produce collagen in order to initiate a repair process [44, 45]. However, when the injury is prolonged as in the case of chronic ethanol use, a sustained accumulation of collagen damages the endothelium of capillaries and increases the distance between the capillaries and the tubules thus delaying or reducing the oxygen supply and nutrients to the epithelial tubular and interstitial cells. This invariably leads to the accumulation of collagen in the renal tissue, as found in this study, leading to kidney dysfunction [2].

Likewise, the basal concentration of TNF-α is considerably low or undetectable under normal conditions but sporadically increases at the onset of renal inflammation to trigger a recovery pathway [9, 18]. TNF-α at low levels promotes tissue repair and induces the regeneration of renal cells in order to promote recovery from injury [18]. Furthermore, TNF-α regulates renal function and controls haemodynamics through its ability to control the constriction of renal vessels, thereby affecting the rate of glomerular filtration [18]. However, this system is destabilized by the chronic use of ethanol as ethanol-induced prolonged inflammatory stress leads to structural kidney damage and dysfunction [9]. This also aligns with the observations in the present study that found that chronic ethanol significantly increased the expression

of TNF-α in the kidney cortex, indicating ethanol-induced renal inflammation.

With the rising prevalence of ethanol use amongst adolescents, it will not be far-fetched to find that the prevalence of chronic renal diseases caused by ethanol (or other substance abuse) will also be on the rise even though there is no data available on the prevalence of ethanol-related renal diseases, specifically in this age group [46]. It is however proven that acute or chronic ethanol consumption can hinder kidney function, and this may be worsened in the presence of other metabolic diseases [17].

Simvastatin, a drug that belongs to the anti-atherosclerotic group of statins, seems to be a promising intervention for treating renal diseases as it is widely used in the treatment of cardiovascular diseases due to its ability to reduce inflammation, cell death, and fibrosis in the heart [20–23, 25, 27, 47–51]. Generally, statins inhibit the upregulation of angiotensin-dependent oxidative stress [52, 53]. More so, simvastatin inhibits the differentiation of fibroblasts into myofibroblasts thus reducing the activity of myofibroblasts and subsequently reducing collagen deposition [27]. Simvastatin is also effective in lowering blood cholesterol in subjects with chronic kidney disease [54]. Christensen *et al.* [55] reported that in mice simvastatin at a dose of 10 or 25 mg, but not 1 mg, hindered the development of glomerular hypertrophy and glomerulonephritis as a result of immune-mediated kidney damage. We are not aware of reports on the effects of simvastatin against ethanol-related renal disease. However, Mohammadi *et al.* [31] found that simvastatin reduced lead-induced renal damage in Balb/c male mice. In the same study, kidney damage was severely reduced in the mice that were treated with 20 mg simvastatin. These findings, although obtained in a different experimental model, support the results of the present study which showed that simvastatin reduced glomerular hypertrophy, renal fibrosis, and inflammation in the chronic ethanol-administration model in young adult mice. Our observations are also consistent with the findings of the simvastatin effects on ethanol-induced myocardial damage in C57BL/6J mice [56]. It is also evident in the present study that both concentrations (5 and 15 mg) of simvastatin suppressed (to varying degrees in both sexes) the onset of ethanol-induced kidney damage. Interestingly, 5 mg simvastatin was more effective for preventing the onset of ethanol-related renal damage whereas 15 mg simvastatin was more effective against ethanol-related renal fibrosis while both concentrations proved to be similarly effective against ethanol-related indices of renal inflammation. It, therefore, indicates that the effectiveness of simvastatin may be specific to the pathology (*e.g.* renal damage, fibrosis, or inflammation) induced by a toxin (*e.g.* ethanol). Additional studies are needed to further elucidate the true effects of simvastatin against ethanol-induced renal damage.

In conclusion, this study demonstrated that simvastatin suppressed the onset of ethanol-related renal damage in a murine model. Although the mechanism of action was not explored in the present study, it has been assumed that the ability of simvastatin to modulate intracellular activities may have played a vital role in preventing ethanol-induced kidney damage. Further studies on the engaged cellular pathways need to be explored. Data presented in this novel study may broaden the applications of simvastatin which could be considered for the treatment or management of ethanol-related kidney diseases.

Article information and declarations

Conflict of interest
The authors declare no conflicting interests in this work.

REFERENCES

1. Van Beusecum J, Inscho EW. Regulation of renal function and blood pressure control by P2 purinoceptors in the kidney. Curr Opin Pharmacol. 2015; 21: 82–88, doi: 10.1016/j.coph.2015.01.003, indexed in Pubmed: 25616035.

2. Ojeda ML, Barrero MJ, Nogales F, et al. Oxidative effects of chronic ethanol consumption on the functions of heart and kidney: folic acid supplementation. Alcohol Alcohol. 2012; 47(4): 404–412, doi: 10.1093/alcalc/ags056, indexed in Pubmed: 22596042.

3. Brzóska MM, Moniuszko-Jakoniuk J, Piłat-Marcinkiewicz B, et al. Liver and kidney function and histology in rats exposed to cadmium and ethanol. Alcohol Alcohol. 2003; 38(1): 2–10, doi: 10.1093/alcalc/agg006, indexed in Pubmed: 12554600.

4. Damman K, Testani JM. The kidney in heart failure: an update. Eur Heart J. 2015; 36(23): 1437–1444, doi: 10.1093/eurheartj/ehv010, indexed in Pubmed: 25838436.

5. Matzopoulos RG, Truen S, Bowman B, et al. The cost of harmful alcohol use in South Africa. S Afr Med J. 2014; 104(2): 127–132, doi: 10.7196/samj.7644, indexed in Pubmed: 24893544.

6. Obad A, Peeran A, Little JI, et al. Alcohol-mediated organ damages: heart and brain. Front Pharmacol. 2018; 9: 81, doi: 10.3389/fphar.2018.00081, indexed in Pubmed: 29487525.

7. Das Kumar S, Vasudevan DM. Alcohol induced effects on kidney. Indian J Clin Biochem. 2008; 23(1): 4–9, doi: 10.1007/s12291-008-0003-9, indexed in Pubmed: 23105711.

8. Hu PJ, Wu MY, Lin TC, et al. Effect of statins on renal function in chronic kidney disease patients. Sci Rep. 2018; 8(1): 16276, doi: 10.1038/s41598-018-34632-z, indexed in Pubmed: 30390007.

9. Abdollahzadeh Fa, Samadi M, Shirpoor A, et al. Ethanol consumption promotes TNF–α signaling pathway in rat kidney: rescue effect of curcumin. J Chem Health Risks. 2022; 12(2): 271–280, doi: 10.22034/jchr.2021.1913474.1211.

10. Marshall EJ. Adolescent alcohol use: risks and consequences. Alcohol Alcohol. 2014; 49(2): 160–164, doi: 10.1093/alcalc/agt180, indexed in Pubmed: 24402246.

11. Morojele N, Ramsoomar L. Addressing adolescent alcohol use in South Africa. South African Medical Journal. 2016; 106(6): 551, doi: 10.7196/samj.2016.v106i6.10944.

12. Yudhisthira NL. Renal histopathology after mixed liquor consumption in Wistar rat. GSC Biol Pharm Sci. 2022; 20(3): 324––329, doi: 10.30574/gscbps.2022.20.3.0354.

13. Swart LA, Seedat M, Nel J. Alcohol consumption in adolescent homicide victims in the city of Johannesburg, South Africa. Addiction. 2015; 110(4): 595–601, doi: 10.1111/add.12825, indexed in Pubmed: 25588696.

14. Olsson CA, Romaniuk H, Salinger J, et al. Drinking patterns of adolescents who develop alcohol use disorders: results from the Victorian Adolescent Health Cohort Study. BMJ Open. 2016; 6(2): e010455, doi: 10.1136/bmjopen-2015-010455, indexed in Pubmed: 26868948.

15. Bertscher A, London L, Rohrs SA. human rights analysis of South Africa's control of marketing of alcoholic beverages bill. Homa Publica. 2020; 4(1): 065–065.

16. Lee YJ, Cho S, Kim SR. Effect of alcohol consumption on kidney function: population-based cohort study. Sci Rep. 2021; 11(1): 2381, doi: 10.1038/s41598-021-81777-5, indexed in Pubmed: 33504820.

17. Latchoumycandane C, Nagy LE, McIntyre TM. Chronic ethanol ingestion induces oxidative kidney injury through taurine-inhibitable inflammation. Free Radic Biol Med. 2014; 69: 403–416, doi: 10.1016/j.freeradbiomed.2014.01.001, indexed in Pubmed: 24412858.

18. Kainama SY, Kakisina P, Watuguly T, et al. Expression of TNF-α on Wistar Rat (L.) with Extract of Pletekan Leaves (L.). Pak J Biol Sci. 2022; 25(10): 938–951, doi: 10.3923/pjbs.2022.938.951, indexed in Pubmed: 36404748.

19. Justo P, Lorz C, Sanz A, et al. Expression of apoptosis regulatory proteins in tubular epithelium stressed in culture or following acute renal failure. Kidney Int. 2000; 57(3): 969–981, doi: 10.1046/j.1523-1755.2000.00925.x, indexed in Pubmed: 10720950.

20. Thabit A, Alhifany A, Alsheikh R, et al. Effect of simvastatin and atorvastatin on serum vitamin d and bone mineral density in hypercholesterolemic patients: a cross-sectional study. J Osteoporos. 2014; 2014: 468397, doi: 10.1155/2014/468397, indexed in Pubmed: 25197610.

21. Liu D, Liu Y, Yi Z, et al. Simvastatin protects cardiomyocytes from doxorubicin cardiotoxicity by suppressing endoplasmic reticulum stress and activating Akt signaling. Int J Clin Exp Med. 2016; 9(2): 2193–201.

22. Morse LR, Coker J, Battaglino RA. Statins and bone health: a mini review. Actual Osteol. 2018; 14(1): 31.

23. Pedersen TR. Pleiotropic effects of statins: evidence against benefits beyond LDL-cholesterol lowering. Am J Cardiovasc Drugs. 2010; 10 Suppl 1: 10–17, doi: 10.2165/1158822-S0-000000000-00000, indexed in Pubmed: 21391729.

24. Gao K, Wang G, Wang Y, et al. Neuroprotective effect of simvastatin via inducing the autophagy on spinal cord injury in the rat model. Biomed Res Int. 2015; 2015: 260161, doi: 10.1155/2015/260161, indexed in Pubmed: 26539474.

25. Xiao X, Chang G, Liu J, et al. Simvastatin ameliorates ventricular remodeling via the TGFβ1 signaling pathway in rats following myocardial infarction. Mol Med Rep. 2016; 13(6): 5093–5101, doi: 10.3892/mmr.2016.5178, indexed in Pubmed: 27121011.

26. Bea S, Oh IS, Kim JuH, et al. High-Intensity statin reduces the risk of mortality among chronic liver disease patients with atherosclerotic cardiovascular disease: a population-based cohort study. J Am Heart Assoc. 2023; 12(8): e028310, doi: 10.1161/JAHA.122.028310, indexed in Pubmed: 37066797.

27. Cahyawati PN, Lestari D, Siskayani A, et al. Simvastatin Improves Renal Function and Glomerulosclerosis in Ischemic-reperfusion Injury. Indones Biomed J. 2020; 12(2): 143–8, doi: 10.18585/inabj.v12i2.1082.

28. Lach G, Fülling C, Bastiaanssen TFS, et al. Enduring neurobehavioral effects induced by microbiota depletion during the adolescent period. Transl Psychiatry. 2020; 10(1): 382, doi: 10.1038/s41398-020-01073-0, indexed in Pubmed: 33159036.

29. Cardoso de Sousa M, Vegian MR, Biserra MA, et al. Influence of chronic alcohol use on osteoblastic differentiation of bone marrow cells, bone properties, and hepatic and renal morphology of rats. Sci World J. 2018; 2018: 2494918, doi: 10.1155/2018/2494918, indexed in Pubmed: 30057490.

30. Patten AR, Fontaine CJ, Christie BR. A comparison of the different animal models of fetal alcohol spectrum disorders and their use in studying complex behaviors. Front Pediatr. 2014; 2: 93, doi: 10.3389/fped.2014.00093, indexed in Pubmed: 25232537.

31. Mohammadi S, Zamani E, Mohadeth Z, et al. Effects of different doses of simvastatin on lead-induced kidney damage in Balb/c male mice. Pharm Sci. 2015; 20(4): 157–162, doi: 10.5681/PS.2015.005.

32. McKay A, Leung BP, McInnes IB, et al. A novel anti-inflammatory role of simvastatin in a murine model of allergic asthma. J Immunol. 2004; 172(5): 2903–2908, doi: 10.4049/jimmunol.172.5.2903, indexed in Pubmed: 14978092.

33. Fernandes C, Marcondes S, Galindo G, et al. Kidney anatomy, histology and histometric traits associated to renosomatic index

in Gymnotus inaequilabiatus (Gymnotiformes: Gymnotidae). Neotrop Ichthyol. 2019; 17(4), doi: 10.1590/1982-0224-20190107.

34. Chen Y, Yu Q, Xu CBA. convenient method for quantifying collagen fibers in atherosclerotic lesions by ImageJ software. Int J Clin Exp Med. 2017; 10(10): 14904–10.

35. Latiff S, Olateju OI. Quantification and comparison of tenocyte distribution and collagen content in the commonly used autografts for anterior cruciate ligament reconstruction. Anat Cell Biol. 2022; 55(3): 304–310, doi: 10.5115/acb.22.005, indexed in Pubmed: 35668478.

36. Balzano T, Arenas YM, Dadsetan S, et al. Sustained hyperammonemia induces TNF-a IN Purkinje neurons by activating the TNFR1-NF-κB pathway. J Neuroinflammation. 2020; 17(1): 70, doi: 10.1186/s12974-020-01746-z, indexed in Pubmed: 32087723.

37. Silverstein DM. Inflammation in chronic kidney disease: role in the progression of renal and cardiovascular disease. Pediatr Nephrol. 2009; 24(8): 1445–1452, doi: 10.1007/s00467-008-1046-0, indexed in Pubmed: 19083024.

38. López-Hernández FJ, López-Novoa JM. Role of TGF-β in chronic kidney disease: an integration of tubular, glomerular and vascular effects. Cell Tissue Res. 2012; 347(1): 141–154, doi: 10.1007/s00441-011-1275-6, indexed in Pubmed: 22105921.

39. Singh VP, Singh N, Jaggi AS. A review on renal toxicity profile of common abusive drugs. Korean J Physiol Pharmacol. 2013; 17(4): 347–357, doi: 10.4196/kjpp.2013.17.4.347, indexed in Pubmed: 23946695.

40. Chagnac A, Weinstein T, Korzets A, et al. Glomerular hemodynamics in severe obesity. Am J Physiol Renal Physiol. 2000; 278(5): F817–F822, doi: 10.1152/ajprenal.2000.278.5.F817, indexed in Pubmed: 10807594.

41. Tobar A, Ori Y, Benchetrit S, et al. Proximal tubular hypertrophy and enlarged glomerular and proximal tubular urinary space in obese subjects with proteinuria. PLoS One. 2013; 8(9): e75547, doi: 10.1371/journal.pone.0075547, indexed in Pubmed: 24086563.

42. Kataoka H, Nitta K, Hoshino J. Glomerular hyperfiltration and hypertrophy: an evaluation of maximum values in pathological indicators to discriminate "diseased" from "normal". Front Med (Lausanne). 2023; 10: 1179834, doi: 10.3389/fmed.2023.1179834, indexed in Pubmed: 37521339.

43. Kuppe C, Gröne HJ, Ostendorf T, et al. Common histological patterns in glomerular epithelial cells in secondary focal segmental glomerulosclerosis. Kidney Int. 2015; 88(5): 990–998, doi: 10.1038/ki.2015.116, indexed in Pubmed: 25853334.

44. Eddy AA. Overview of the cellular and molecular basis of kidney fibrosis. Kidney Int Suppl (2011). 2014; 4(1): 2–8, doi: 10.1038/kisup.2014.2, indexed in Pubmed: 25401038.

45. Latchoumycandane C, Hanouneh M, Nagy LE, et al. Inflammatory PAF receptor signaling initiates hedgehog signaling and kidney fibrogenesis during ethanol consumption. PLoS One. 2015; 10(12): e0145691, doi: 10.1371/journal.pone.0145691, indexed in Pubmed: 26720402.

46. Steele MR, Belostotsky V, Lau KK. The dangers of substance abuse in adolescents with chronic kidney disease: a review of the literature. CANNT J. 2012; 22(1): 15–22; quiz 23, indexed in Pubmed: 22558679.

47. Patel R, Nagueh SF, Tsybouleva N, et al. Simvastatin induces regression of cardiac hypertrophy and fibrosis and improves cardiac function in a transgenic rabbit model of human hypertrophic cardiomyopathy. Circulation. 2001; 104(3): 317–324, doi: 10.1161/hc2801.094031, indexed in Pubmed: 11457751.

48. Sun F, Duan W, Zhang Yu, et al. Simvastatin alleviates cardiac fibrosis induced by infarction via up-regulation of TGF-β receptor III expression. Br J Pharmacol. 2015; 172(15): 3779–3792, doi: 10.1111/bph.13166, indexed in Pubmed: 25884615.

49. MacDougall DA, Pugh SD, Bassi HS, et al. Simvastatin promotes cardiac myocyte relaxation in association with phosphorylation of troponin I. Front Pharmacol. 2017; 8: 203, doi: 10.3389/fphar.2017.00203, indexed in Pubmed: 28469574.

50. Lee MMY, Sattar N, McMurray JJV, et al. Statins in the Prevention and Treatment of Heart Failure: a Review of the Evidence. Curr Atheroscler Rep. 2019; 21(10): 41, doi: 10.1007/s11883-019-0800-z, indexed in Pubmed: 31350612.

51. Skrzypiec-Spring M, Sapa-Wojciechowska A, Haczkiewicz-Leśniak K, et al. HMG-CoA reductase inhibitor, simvastatin is effective in decreasing degree of myocarditis by inhibiting metalloproteinases activation. Biomolecules. 2021; 11(10), doi: 10.3390/biom11101415, indexed in Pubmed: 34680049.

52. Zhou Q, Liao JK. Statins and cardiovascular diseases: from cholesterol lowering to pleiotropy. Curr Pharm Des. 2009; 15(5): 467–478, doi: 10.2174/138161209787315684, indexed in Pubmed: 19199975.

53. Zhang X, Xiang C, Zhou YH, et al. Effect of statins on cardiovascular events in patients with mild to moderate chronic kidney disease: a systematic review and meta-analysis of randomized clinical trials. BMC Cardiovasc Disord. 2014; 14: 19, doi: 10.1186/1471-2261-14-19, indexed in Pubmed: 24529196.

54. Baigent C, Landray MJ, Reith C, et al. SHARP Investigators. The effects of lowering LDL cholesterol with simvastatin plus ezetimibe in patients with chronic kidney disease (Study of Heart and Renal Protection): a randomised placebo-controlled trial. Lancet. 2011; 377(9784): 2181–2192, doi: 10.1016/S0140-6736(11)60739-3, indexed in Pubmed: 21663949.

55. Christensen M, Su AW, Snyder RW, et al. Simvastatin protection against acute immune-mediated glomerulonephritis in mice. Kidney Int. 2006; 69(3): 457–463, doi: 10.1038/sj.ki.5000086, indexed in Pubmed: 16407885.

56. Nchodu M, Efuntayo A, du Preez R, et al. Simvastatin significantly reduced alcohol-induced cardiac damage in adolescent mice. Cardiovasc Toxicol. 2024; 24(1): 15–26, doi: 10.1007/s12012-023-09821-6, indexed in Pubmed: 38261135.

ORIGINAL PAPER

VM
VIA MEDICA

Diosmetin ameliorates osteoarthritic inflammation *in vivo* and ECM macromolecules degradation in interleukin-1β-stimulated murine chondrocytes through the Nrf2/NF-κB pathway

Liang Qian[1], Chuang Li[1], Hong Liu[1], Hui Zhou[1], Tao Tan[2]

[1]Department of Orthopedics, The Eighth Hospital of Wuhan, Wuhan, China

[2]Department of Trauma Surgery, The Eighth Hospital of Wuhan, Wuhan, China

Abstract

Introduction. Osteoarthritis (OA) is a prevailing degenerative disease in elderly population and can lead to severe joint dysfunction. Studies have revealed various pharmacological activities of diosmetin, including the anti-OA efficacy. The present study further investigated its effect on interleukin (IL)-1β-induced OA in chondrocytes.

Material and methods. Primary chondrocytes were isolated from young mice, stimulated with IL-1β (10 ng/mL), and pretreated with diosmetin (10 and 20 μM) to conduct the *in vitro* assays. CCK-8 assay assessed the cytotoxicity of diosmetin whereas the levels of inflammatory factors (PGE2, nitrite, TNF-α, and IL-6) in homogenized cells were evaluated by ELISA. The levels of inflammatory cytokines, content of extracellular matrix (ECM), and signaling-related proteins (Nrf2, HO-1, and NF-κB p65) were assessed by western blotting. Expression of collagen II, p65, and Nrf2 in the chondrocytes was confirmed by immunofluorescence staining. The chondrocytes treated with IL-1β and diosmetin were transfected with Nrf2 knockdown plasmid (si-Nrf2) to investigate the role of Nrf2. *In vivo* OA mouse model was induced by surgically destabilizing the medial meniscus (DMM). Safranin O staining was conducted to assess the OA severity in the knee-joint tissue.

Results. Diosmetin suppressed the expression of iNOS, COX-2, PGE2, nitrite, TNF-α, IL-6, MMP-13, and ADAMTS-5 induced by IL-1β in chondrocytes. The expression of p-p65, p-IκBα, and nuclear p65 was decreased whereas that of Nrf2 and HO-1 increased by diosmetin treatment in IL-1β-treated chondrocytes. Nrf2 knockdown by siRNA reversed the inhibitory effect of diosmetin on IL-1β-induced degradation of ECM proteins and inflammatory factors in cultured chondrocytes. In the DMM-induced model of OA, diosmetin alleviated cartilage degeneration and decreased the Osteoarthritis Research Society International score.

Conclusions. Diosmetin ameliorates expression of inflammation biomarkers and ECM macromolecules degradation in cultured murine chondrocytes *via* inactivation of NF-κB signaling by activating Nrf2/HO-1 signaling pathway. *(Folia Histochem Cytobiol 2024; 62, 2:99–109)*

Keywords: mouse; osteoarthritis; chondrocytes; diosmetin; ECM proteins; Nrf2/HO-1; NF-κB

INTRODUCTION

Osteoarthritis (OA) is a degenerative joint disorder that leads to unbearable pain, seriously affecting the life quality of more than 250 million people worldwide [1]. Degeneration and inflammation of articular cartilage are the two main features of it [2]. Current treatments for OA mainly focus on the pain management and symptom alleviation [3]. However, those pain-relief drugs, such as corticosteroids, opioids, and nonsteroidal anti-inflammatory drugs (NSAIDs) have certain side effects, and surgical treatment also carries significant risks, which remain an obstacle to preventing OA [4]. Thus, novel therapeutic targets with fewer side effects are needed.

Correspondence address:

Tao Tan
The Eighth Hospital of Wuhan,
No.1 Huasheng Road, Tazihu Street, Jiang'an District,
Wuhan 430000, Hubei Province, China
e-mail: tantaodoctor@hotmail.com

Increasing studies have revealed inflammatory mechanisms and cartilage extracellular matrix (ECM) damage as the crucial risk factors for the OA progression [5]. It is well known that the key pro-inflammatory cytokine interleukin-1β (IL-1β) is highly expressed in the cartilage tissue of OA patients [6]. It can trigger the secretion of other inflammatory mediators synthesized by inducible nitric oxide synthase 2 (iNOS) and cyclooxygenase-2 (COX-2) and proteolytic enzymes including matrix metalloproteinases (MMPs) in OA chondrocytes, resulting in the disorders of the homeostasis between ECM synthesis and degradation [7]. Therefore, inhibition of IL-1β-induced inflammation and ECM degradation has become a potential approach to alleviate the progression of OA.

Diosmetin (3′,5,7-trihydroxy-4′-methoxy flavone) is a type of flavonoid, which is abundant in lemon peel and citrus fruits [8]. Hesperidin, an another flavanone derived from *Citrus aurantium L.*, has been reported to repress the OA development [9]. Multiple pharmacological activities of diosmetin have been found, such as anti-cancer [10], anti-oxidant [11], anti-microbial [12], anti-apoptotic [13], anti-estrogenic [14], anti-hyperglycemic [15], and anti-diabetic [16]. Particularly, it has also been reported to be effective in inhibiting inflammatory reaction in various diseases, including myocardial ischemia-reperfusion injury [17], colitis [18], and rheumatoid arthritis [19]. In recent years, the beneficial effects of diosmetin on bone-related diseases have been revealed. For instance, diosmetin regulates bone formation and has an anti-osteoporosis function [20, 21]. Shao *et al.* revealed its inhibitory effect on osteolysis induced by lipopolysaccharide [22]. It can also protect against osteopenia induced by chronic kidney disease [23]. In a recent study, diosmetin has been shown to prevent the loss of subchondral bone in OA mouse model [24]. However, its specific role in IL-1β-treated chondrocytes has not been detected yet.

In this study, we investigated the effect of diosmetin on IL-1β-induced degradation of ECM proteins and inflammatory response in cultured murine chondrocytes. We also revealed the possible signaling pathways that participate in the regulatory role of diosmetin in OA. The results of this study may provide novel research option for improving OA treatments.

MATERIALS AND METHODS

Animal model

C57BL/6 mice (male; 5–8 weeks old) were provided by the Animal Center of Chinese Academy of Sciences (Shanghai, China) and randomly divided into three groups (n = 12 in each group): Sham; DMM; and DMM + diosmetin. All the mice were anesthetized

using 1% sodium pentobarbital (60 mg/kg). To establish an OA model, the right knee joint capsule of the mouse was exposed, and then medial meniscotibial ligaments was sectioned to induce the destabilization of the medial meniscus (DMM) as described by Glasson *et al.* [25]. Mice in the Sham group received arthrotomy without transecting the meniscotibial ligament. Finally, the right knee joint capsule and skin were sutured using surgical absorbable suture. Two weeks after the DMM surgery, diosmetin (10 mg/kg; purity: 99.80%; 520-34-3; MedChemExpress, China) dissolved in sterile saline was subcutaneously injected into the mice in the DMM + diosmetin group every other day for 7 consecutive days. The treatment dose was used according to the previous study [22]. Meanwhile, the mice in the Sham and DMM groups only received 1 ml of sterile 0.9% NaCl. At the end of the drug treatment, all the mice were euthanized using an overdose injection of pentobarbital sodium (100 mg/kg), and the knee joints of all mice were resected for the subsequent experiments. All animal experiments were performed in accordance with the National Institutes of Health Guidelines for the Care and Use of Laboratory Animals and were approved by the Ethical Review System for Laboratory Animal Welfare of the Wuhan Myhalic Biotechnology Co., Ltd (approval number: HLK-20207112; approval date: 2023.7.26).

Safranin O staining

The collected knee joints were fixed in paraformaldehyde (4%; Sigma-Aldrich, MO, USA) for 24 h and then decalcified in EDTA (10%; Sigma-Aldrich). Followed by paraffin embedding, the specimens were sectioned into slices (5 μm-thick) and stained with safranin O/fast green (Solarbio, Beijing, China) [26]. Then, the Osteoarthritis Research Society International (OARSI) scoring system was used to grade the severity of OA (between 0 and 15) in each group according to Glasson *et al.* recommendations [27].

Cell culture and treatment

Primary chondrocytes were isolated from C57BL/6 mice (2 weeks old; Animal Center of Chinese Academy of Sciences). Briefly, the articular cartilage was separated from the knee joint of the mice after euthanasia (cervical dislocation under inhalation anesthesia) and cut into 1–3 mm pieces, which were then treated with trypsin (0.25%; Gibco, CA, USA) for 10 min and collagenase type II (0.25%; Gibco) for 1.5 h at 37°C and centrifuged for 5 min at 1000 *g* to obtain the cell pellet. Then, the collected chondrocytes were cultured in Dulbecco's modified Eagle's medium (Gibco) containing penicillin/streptomycin (1%; Gibco) and

fetal bovine serum (10%; Gibco) at 37°C. Cells were passaged when the confluency reached 80–90%, and the second-generation chondrocytes were selected. Chondrocytes were stimulated with IL-1β (10 ng/mL; PeproTech, Drive Cranbury, NJ, USA) for 24 h and then the cells were treated with diosmetin (10 and 20 μM) for 48 h. In rescue assay, cells were transfected with si-Nrf2 (sc-37030; Santa Cruz, USA) and its control using Lipofectamine 2000 (Thermo Fisher, Waltham, MA, USA). Transfection efficiency was verified using western blotting analysis.

CCK-8 assay

Cell counting kit-8 (Beyotime, *Haimen, Jiangsu*, China) was used to assess the cytotoxicity of diosmetin to mouse chondrocytes. Chondrocytes were seeded on 96-well plates and treated with diosmetin (5, 10, 20, or 30 μM) for 24 h and 48 h. Then, the CCK-8 solution (10 μL) was added. After 4 h of incubation, the absorbance at 450 nm was determined using a microplate reader (Thermo Fisher).

Western blotting

Total protein extraction from the treated mouse chondrocytes was conducted using RIPA lysis buffer (Beyotime), and the BCA protein assay kit (Beyotime) was used to evaluate the protein concentration. Proteins (50 μg) were separated by SDS-PAGE (10% gels) and electro-transferred onto PVDF membrane (Millipore, USA), which was subsequently blocked with 5% skim milk. Primary antibodies against iNOS (ab178945; 1:1000; Abcam, UK), COX-2 (ab179800; 1:1000), collagen II (ab34712; 1:1000), aggrecan (FNab00213; 1:500; FineTest, China), MMP-13 (ab39012; 1:3000), ADAMTS-5 (ab41037; 1:250), p-p65 (ab76302; 1:1000), p65 (ab32536; 1:1000), p-IκBα (ab133462; 1:10000), IκBα (ab32518; 1:1000), Nrf2 (abs130481; 1:500; Absin Bioscience, China), HO-1 (ab52947; 1:2000), GAPDH (ab181602; 1:10000), and lamin B (ab151735; 1:2000) were incubated at 4°C with the membranes overnight. Then, goat anti-rabbit secondary antibody (ab205718; 1:2000) was added. Finally, electrochemiluminescence plus reagent (Invitrogen, China) was prepared for visualizing the protein bands, and the intensity of protein bands was quantified with Image Lab 3.0 software (Bio-Rad, USA).

ELISA

Mouse chondrocytes were seeded on 6-well plates and treated with IL-1β (10 ng/mL) for 24 h and diosmetin (10 and 20 μM) for 48 h. Then the levels of PGE2, Nitrite, TNF-α, and IL-6 in the cell culture supernatants were measured by ELISA kits (Invitrogen) according to the manufacturer's protocol.

Immunofluorescence

The chondrocytes were fixed with 4% paraformaldehyde for 10 min and permeabilized with Triton X-100 (0.1%; Sigma-Aldrich) for 15 min. After rinsing with phosphate-buffered saline (PBS), cells were incubated with primary antibodies against Collagen II (ab34712), p65 (ab32536), and Nrf2 (abs130481; 1:100; Absin Bioscience) at 4°C overnight. Then, the secondary antibodies were added (ab150077; 1:200) for 1 h at room temperature. Then, the nuclei of cells were stained with 4',6-diamidino-2'-phenylindole (Sigma-Aldrich) for 30 min. At the end, an Olympus IX73 fluorescence microscope (Olympus, Tokyo, Japan) was used for analyzing the results.

Statistical analysis

SPSS18.0 software (IBM, USA) was used to conduct the statistical analysis, and the data are presented as mean ± SD. Significant differences ($P < 0.05$) were analyzed using Student's *t*-test or one-way analysis of variance followed by the Tukey *post hoc* tests. Nonparametric data (OARSI scores) were evaluated using the Kruskal-Wallis H test. All the experiments were repeated at least three times.

RESULTS

Diosmetin inhibits IL-1β-induced markers of inflammation in chondrocytes

To confirm the optimal concentrations of diosmetin, CCK-8 assay was conducted to evaluate the cell viability of chondrocytes under the treatment with diosmetin (5, 10, 20, and 30 μM). Chondrocytes viability had no significant alteration when the cells were treated with 5, 10, and 20 μM of diosmetin for 24 and 48 h; however, 30 μM of diosmetin slightly reduced the viability of cells after 48 h (Fig. 1A). Therefore, diosmetin at 10 μM and 20 μM concentrations was used for the subsequent experiments. After the stimulation of chondrocytes by IL-1β, the protein levels of enzymes producing inflammatory mediators (iNOS and COX-2) were increased in the chondrocytes. Subsequent treatment of cells with diosmetin remarkably reduced the protein levels of iNOS and COX-2 (Fig. 1B, C).

To further check the effect of diosmetin on inflammatory biomarkers induced by IL-1β in chondrocytes, ELISA was performed to further assess the changes in PGE2, nitrite, TNF-α, and IL-6 levels in the supernatants. Consistently, the treatment with diosmetin suppressed the release of PGE2, nitrite, TNF-α, and IL-6, indicating its anti-inflammatory role in the *in vitro* OA model (Fig. 1D–G).
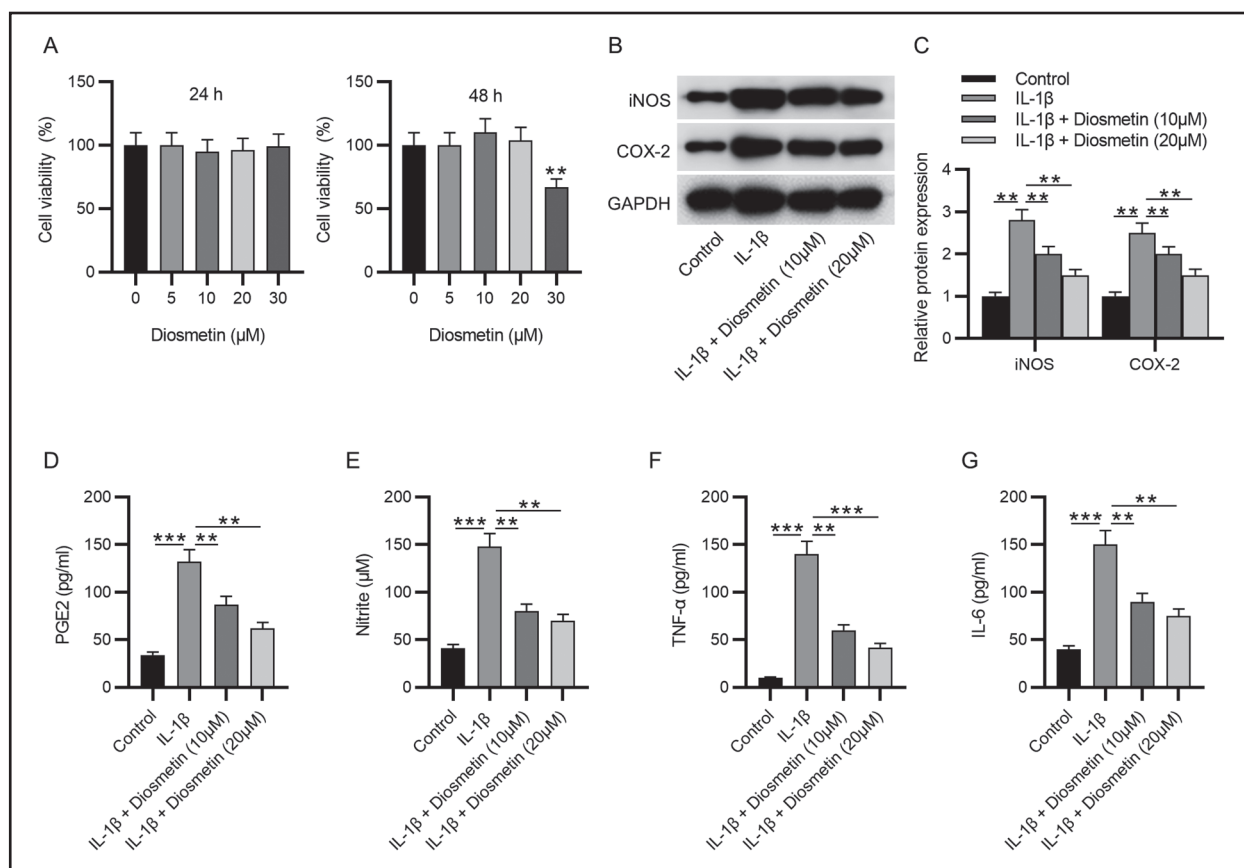
Figure 1. Diosmetin inhibits IL-1β-induced inflammation in cultured murine chondrocytes. **A.** CCK-8 assessed the viability of chondrocytes under the treatment of diosmetin (5, 10, 20, and 30 μM). **B, C.** Western blotting of iNOS and COX-2 expression in chondrocytes treated with IL-1β and diosmetin. **D, G.** The levels of inflammatory markers in the supernatants of chondrocytes treated with IL-1β and diosmetin were measured by ELISA as described in Methods. **P < 0.01, *** P < 0.001

Diosmetin suppresses IL-1β-induced EC molecules' degradation in chondrocytes

In this part of our study, we further explored the effect of diosmetin on ECM molecules degradation. We found (Fig. 2) that the levels of collagen II and aggrecan proteins were decreased while the levels of MMP-13 and ADAMTS-5 proteins were increased in the chondrocytes stimulated by IL-1β, suggesting severe degradation of ECM molecular components in chondrocytes. By contrast, diosmetin promoted collagen II and aggrecan expression and restrained MMP-13 and ADAMTS-5 expression in IL-1β-treated chondrocytes (Fig. 2A–C). Immunofluorescence also showed decreased collagen II expression after IL-1β stimulation, while collagen II expression was restored in the cells incubated with IL-1β and diosmetin (Fig. 2D), indicating that diosmetin had inhibitory effect on ECM molecules' degradation in IL-1β-treated chondrocytes.

Diosmetin inactivates NF-κB signaling pathway in IL-1β-treated chondrocytes

To investigate the potential mechanisms of diosmetin action, expression of signaling-related proteins was evaluated in cultured chondrocytes. Relative to the control group, IL-1β upregulated p-p65 and p-IκBα expression and downregulated IκBα expression, and diosmetin reversed these alterations (Fig. 3A, B). Additionally, the protein level of nuclear p65 in the chondrocytes was increased by IL-1β and was reduced by diosmetin (Fig. 3C, D). Consistent with that, immunofluorescence showed that diosmetin decreased the fluorescence of nuclear p65 induced by IL-1β in the chondrocytes (Fig. 3E), suggesting that diosmetin inhibited NF-κB signaling by blocking NF-κB p65 nuclear translocation.

Diosmetin activates Nrf2/HO-1 signaling pathway in IL-1β-treated chondrocytes

Western blotting revealed that the levels of nuclear Nrf2 and HO-1 proteins were not affected by IL-1β in chondrocytes. However, diosmetin treatment markedly enhanced the protein levels of nuclear Nrf2 and HO-1 in IL-1β-treated chondrocytes (Fig. 4A, B). Consistently, enhanced fluorescence intensity of nuclear Nrf2 was observed in the IL-1β + diosmetin group relative to the IL-1β group (Fig.4C), suggesting
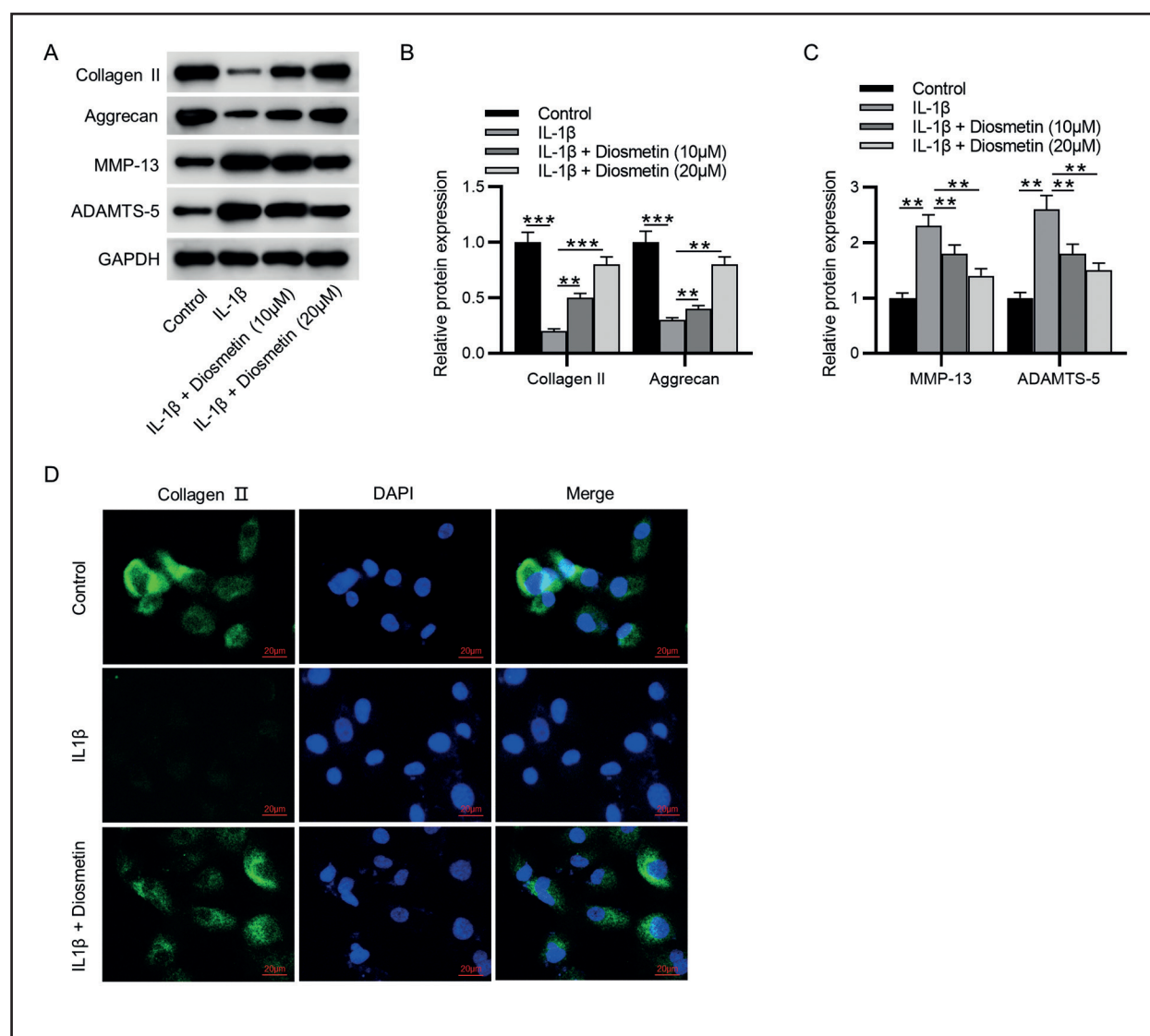
Figure 2. Diosmetin suppresses IL-1β-induced ECM degradation in chondrocytes. **A–C.** Western blotting of ECM-related proteins in chondrocytes treated with IL-1β and diosmetin. **D.** Immunofluorescence of collagen II expression in chondrocytes treated with IL-1β and diosmetin. **P < 0.01, ***P < 0.001.

that diosmetin activated Nrf2/HO-1 pathway in IL--1β-treated chondrocytes.

Diosmetin inhibits IL-1β-induced changes in chondrocytes *via* activation of Nrf2/HO-1 signaling pathway

In this part of our study, chondrocytes were treated with IL-1β (10 ng/mL) and diosmetin (20 μM) and then transfected with Nrf2 knockdown plasmid (si-Nrf2) or its control (si-NC) to investigate how Nrf2/HO-1 signaling possibly influences the diosmetin action in OA. Transfection efficiency was then confirmed by western blotting, which showed that the protein levels of nuclear Nrf2 and HO-1 were markedly reduced in the si-Nrf2-treated chondrocytes si-Nrf2 compared with the cells transfected

with control plasmid (Fig. 5A, B). Interestingly, the downregulated protein levels of nuclear p65 and p-p65 induced by diosmetin were restored by Nrf2 knockdown (Fig. 5C, D). In addition, the elevated protein levels of inflammatory markers (iNOS and COX-2) and ECM degradation markers (MMP-13 and ADAMTS-5) induced by IL-1β were decreased by diosmetin, whereas Nrf2 knockdown counteracted these diosmetin effects (Fig. 5E, F). Moreover, the effect of diosmetin on the levels of inflammatory biomarkers PGE2, nitrite, TNF-α, and IL-6 in the supernatants of IL-1β-treated cells was also abolished by Nrf2 knockdown (Fig. 5G–J). These results suggested that diosmetin may inhibit NF-κB signaling-mediated inflammatory response by activating Nrf2.
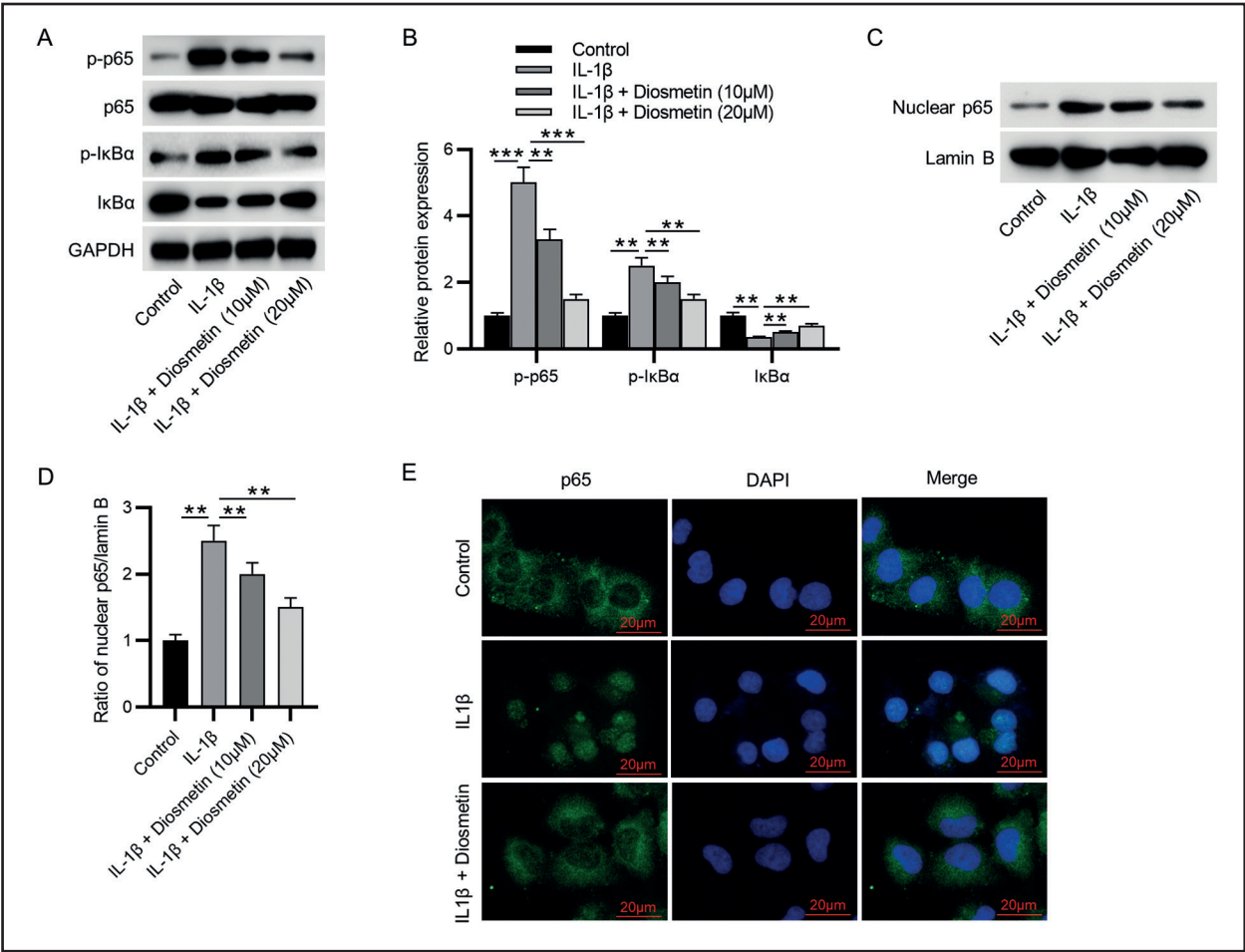
Figure 3. Diosmetin inactivates NF-κB signaling pathway in IL-1β-treated chondrocytes. **A–D.** Western blotting of NF-κB signaling-related proteins in chondrocytes treated with IL-1β and diosmetin. **E.** Immunofluorescence of p65 expression in chondrocytes treated with IL-1β and diosmetin. **P < 0.01, *** P < 0.001.
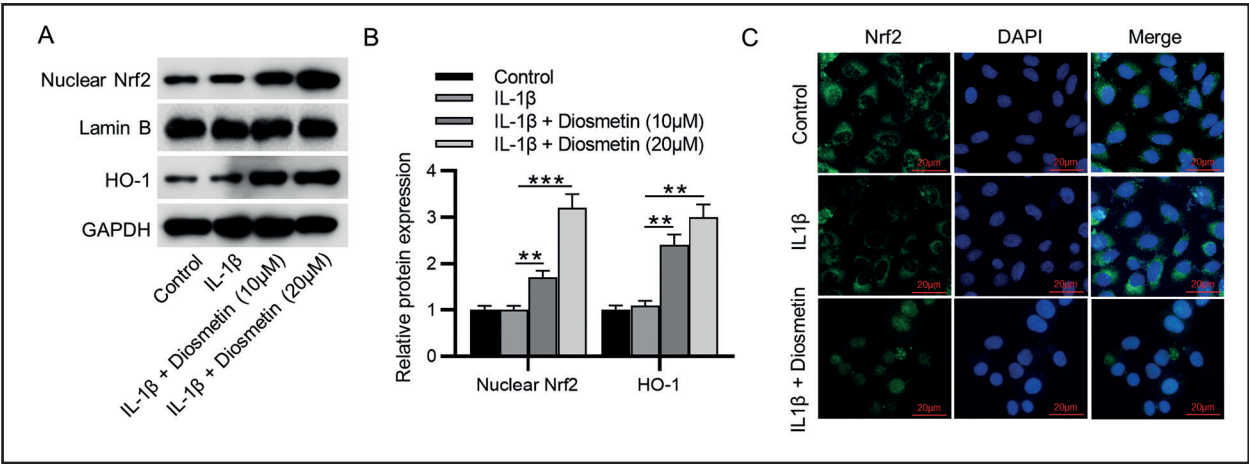

Figure 4. Diosmetin activates Nrf2/HO-1 signaling pathway in IL-1β-treated chondrocytes. **A, B.** Western blotting of Nrf2/HO-1 signaling-related proteins in chondrocytes treated with IL-1β and diosmetin. **C.** Immunofluorescence of Nrf2 expression in chondrocytes treated with IL-1β and diosmetin. **P < 0.01, ***P < 0.001.
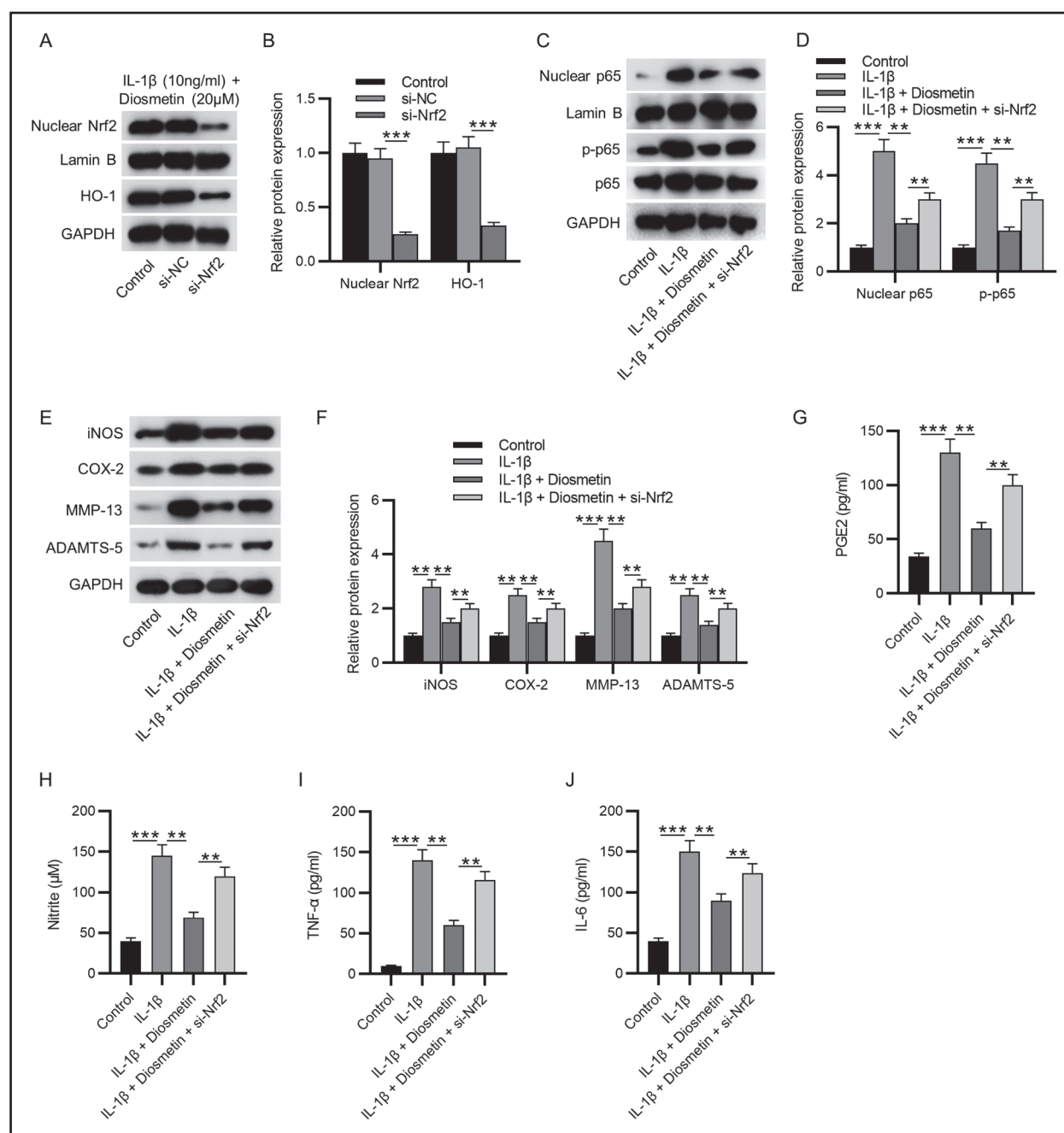
Liang Qian et al. Effect of diosmetin in osteoarthritis

105

Figure 5. Diosmetin inhibits IL-1β-induced markers of OA in chondrocytes *via* activation of Nrf2/HO-1 signaling pathway. **A, B.** Western blotting of NF-κB and **C, D**. Nrf2/HO-1 signaling-related proteins, as well as **(E, F)** inflammation and ECM-related proteins. **G–J.** The levels of inflammatory markers in IL-1β-treated chondrocytes pretreated with diosmetin and transfected with siRNA targeting Nrf2 were assessed by ELISA. $^{**}P < 0.01$, $^{***}P < 0.001$.

Diosmetin improves osteoarthritis progression in destabilized medial meniscus (DMM) mouse model

The OA mouse model was established by the DMM surgery to investigate the role of diosmetin in protecting articular cartilage. According to the results of Safranin O staining, the mice in the DMM group presented early OA-like manifestations, including erosion of the cartilage and massive loss of proteo-

glycan staining with higher OARSI score compared to the control (Fig. 6). In contrast, diosmetin treatment significantly slowed the OA progression in mouse model, which was evidenced by less cartilage erosion, smoother cartilage surface, and more proteoglycan staining than the DMM group. In addition, the increase of OARSI score in the DMM group was suppressed by diosmetin as well, indicating its protective effect against pathological osteoarthritic changes (Fig. 6A, B).
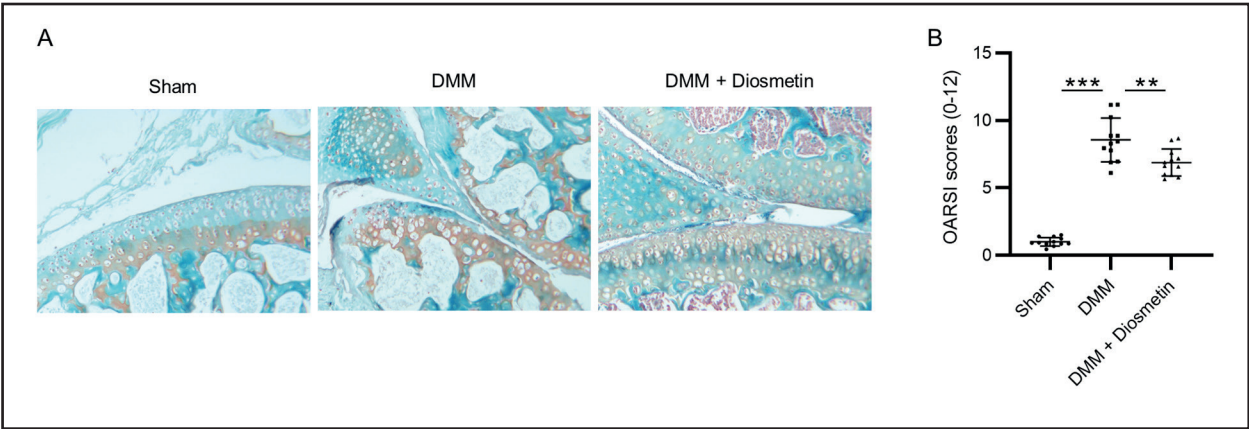
Figure 6. Diosmetin improves osteoarthritis progression in destabilization of the medial meniscus mouse model. **A.** Safranin O staining of the articular cartilage from different experimental groups. **B.** Osteoarthritis Research Society International (OARSI) scores of cartilages from different experimental groups. **P < 0.01, ***P < 0.001.
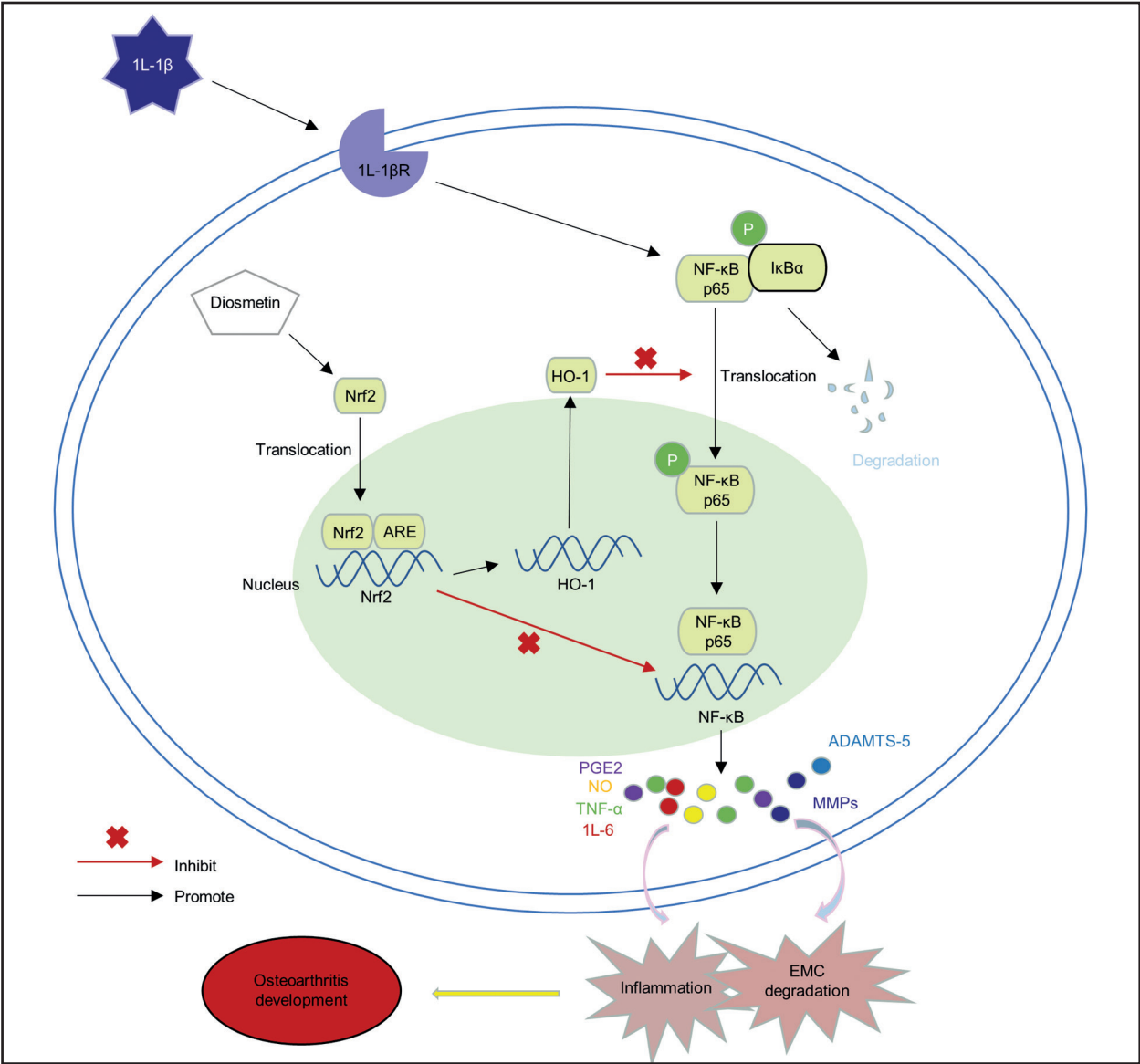

Figure 7. Graphical summary of diosmetin effects on IL-1β-induced murine chondrocytes.

Liang Qian et al. Effect of diosmetin in osteoarthritis

107

DISCUSSION

In recent years, increasing plant-based natural agents have caught much attention of researchers and have been confirmed as potential drugs to treat OA, such as Astilbin extracted from Dimorphandra Mollis [28], murine OA model), β-HIVS derived from Lithospermum erythrorhizon [29], murine OA model), and Xanthohumol isolated from hops [30], rat OA model). Diosmetin from *Citrus aurantium L.* has been shown to protect cartilage in a surgically-induced OA mouse model [24]. We for the first time confirmed the anti-OA effect of diosmetin occurs *via* Nrf2/NF-κB signaling pathways. Inflammation has been proved to be a critical factor in the pathogenesis of OA [28]. IL-1β is often used as an inducer of OA in articular chondrocytes, and it was shown to stimulate the secretion of inflammatory cytokines IL-6 and TNF-α, leading to an inflammatory response [29]. Diosmetin is recognized as an anti-inflammatory agent in various diseases. For example, in atopic dermatitis model, it has been reported to inhibit the production of nitric oxide (NO) and reduce the expression of iNOS [30]. Yu *et al.* also demonstrated its inhibitory effect on iNOS expression in cerulein-induced acute pancreatitis [31]. Similarly, we found that the levels of iNOS and COX-2 proteins and their products were elevated in mouse chondrocytes under the stimulation by IL-1β, and their levels were significantly reduced by diosmetin treatment, suggesting the anti-inflammatory action of diosmetin in the IL-1β-induced OA *in vitro* model. It has been reported that PGE2, nitrite, TNF-α, and IL-6 are upregulated in OA animal models [32, 33]. PGE2, nitrite, TNF-α, and IL-6 are regarded as important catabolic factors that can trigger the degradation of ECM macromolecules in chondrocytes [7, 34]. In our study, diosmetin remarkably reduced levels of those catabolic factors in IL-1β-treated chondrocytes, suggesting that during OA *in vivo* diosmetin may suppress the ECM degradation and protect chondrocytes and articular cartilage against inflammation-induced dysfunction.

Many studies revealed that impaired ECM metabolism also contributes to OA progression [35]. Under IL-1β stimulation in chondrocytes, key ECM degradative enzymes, including MMPs and aggrecanases, are upregulated, and collagen II and aggrecan are downregulated, which contribute to ECM molecules' degradation [29]. Consistently, here, IL-1β-induced murine chondrocytes showed decreased expression of collagen II and aggrecan and increased levels of MMP-13 and ADAMTS-5, while diosmetin reversed the changes, suggesting its suppressive effect on IL--1β-induced ECM degradation.

As an upstream regulatory factor of inflammation-related factors (iNOS, IL-1β, and TNF-α and other) and cartilage-degrading enzymes (ADAMTs and MMPs), NF-κB signaling has been widely reported to participate in inflammatory processes and degradation of ECM in articular cartilage and chondrocytes [36, 37]. After stimulation by IL-1β, the IκB subunit can be activated, resulting in the transport of NF-κB p65 to the nucleus [38, 39]. Diosmetin has been previously reported to exert anti-inflammatory effect by decreasing the p-JNK and p-NF-κB protein expression in the aorta of hypertensive rats [40]. Chen *et al.* reported that diosmetin inhibited inflammatory response in synoviocyte-like MH7A cells by inhibiting Akt and NF-κB pathways, suppressing features of rheumatoid arthritis *in vitro* model [19]. Here, we found that diosmetin reversed the upregulated p-p65, p-IκBα, nuclear p65 expression and downregulated IκBα expression induced by IL-1β in chondrocytes, indicating that probably *via* inactivation of NF-κB signaling diosmetin inhibits markers of inflammation and ECM degradation in IL-1β-exposed chondrocytes.

Nrf2 is demonstrated to be responsible for the inactivation of NF-κB pathway [41], and emerging evidence has implied the key role of Nrf2 pathway in alleviating IL-1β-induced ECM molecule's degradation in chondrocytes *via* the inhibition of NF-κB pathway [42, 43]. Consistent with the previous study showing the effect of diosmetin on activation of Nrf2 in thoratic aorta of hypertensive rats [40], also in our *in vitro* OA model, diosmetin upregulated the expression of Nrf2 and HO-1 protein in IL-1β-treated chondrocytes, which confirmed the beneficial involvement of Nrf2/HO-1 pathway. Furthermore, we were the first to show that Nrf2 knockdown in IL-1β-treated chondrocytes significantly abolished the inhibitory effect of diosmetin on NF-κB signaling activation, inflammation, and ECM molecules' degradation, indicating that diosmetin mitigates OA development *via* the inactivation of NF-κB signaling by promoting Nrf2/HO-1 pathway.

To verify the anti-inflammatory effect of diosmetin elucidated in the *in vitro* OA model, we conducted a histological analysis of the articular cartilage of mice subjected to the classical DMM OA model. The protective effect of diosmetin against IL-1β-induced inflammatory in the *in vitro* model of OA has been confirmed in the *in vivo* model. Diosmetin dampened pathological osteoarthritic changes including cartilage erosion and massive loss of proteoglycans. In addition, the reduced OARSI score was shown in diosmetin-treated OA mice, which confirmed the therapeutic effect of diosmetin in murine OA model.

In conclusion, the current study revealed that diosmetin effectively alleviated OA progression under *in vivo* and *in vitro* conditions acting *via* the inactivation of NF-κB signaling pathway by activating Nrf2/HO-1 signaling (Fig. 7). The results of our study proved that diosmetin could be considered as a potential drug for OA treatment.

Article information and declarations

Data availability statement
The datasets used or analyzed during the current study are available from the corresponding author on reasonable request.

Ethics statement
All animal experiments were performed in accordance with the National Institutes of Health Guidelines for the Care and Use of Laboratory Animals and were approved by the Ethical Review System for Laboratory Animal Welfare of the Wuhan Myhalic Biotechnology Co., Ltd (approval number: HLK-20207112; approval date: 2023.7.26).

Author contributions
Liang Qian was the main designer of this study. Liang Qian, Chuang Li, Hong Liu, Hui Zhou and Tao Tan collected and analyzed the data. Liang Qian, Chuang Li, Hong Liu, Hui Zhou and Tao Tan drafted the manuscript. All authors read and approved the final manuscript.

Funding
This research received no specific grant from any funding agency in the public, commercial, or not-for--profit sectors.

Acknowledgments
We appreciate all participants who contributed to the study.

Conflict of interest
The authors declared no competing interests in this study.

REFERENCES

1. Hunter DJ, Bierma-Zeinstra S. Osteoarthritis. Lancet. 2019; 393(10182): 1745–1759, doi: 10.1016/S0140-6736(19)30417-9, indexed in Pubmed: 31034380.
2. Glyn-Jones S, Palmer AJR, Agricola R, et al. Osteoarthritis. Lancet. 2015; 386(9991): 376–387, doi: 10.1016/S0140-6736(14)60802-3, indexed in Pubmed: 25748615.
3. Zhang W, Ouyang H, Dass C, et al. Current research on pharmacologic and regenerative therapies for osteoarthritis. Bone Res. 2016; 4(1), doi: 10.1038/boneres.2015.40.
4. Bindu S, Mazumder S, Bandyopadhyay U. Non-steroidal anti-inflammatory drugs (NSAIDs) and organ damage: A current perspective. Biochem Pharmacol. 2020; 180: 114147, doi: 10.1016/j.bcp.2020.114147, indexed in Pubmed: 32653589.
5. Philp AM, Davis ET, Jones SW. Developing anti-inflammatory therapeutics for patients with osteoarthritis. Rheumatology (Oxford). 2017; 56(6): 869–881, doi: 10.1093/rheumatology/kew278, indexed in Pubmed: 27498352.
6. Kobayashi M, Squires GR, Mousa A, et al. Role of interleukin-1 and tumor necrosis factor alpha in matrix degradation of human osteoarthritic cartilage. Arthritis Rheum. 2005; 52(1): 128–135, doi: 10.1002/art.20776, indexed in Pubmed: 15641080.
7. Kapoor M, Martel-Pelletier J, Lajeunesse D, et al. Role of proinflammatory cytokines in the pathophysiology of osteoarthritis. Nat Rev Rheumatol. 2011; 7(1): 33–42, doi: 10.1038/nrrheum.2010.196, indexed in Pubmed: 21119608.
8. Zheng Y, Zhang R, Shi W, et al. Metabolism and pharmacological activities of the natural health-benefiting compound diosmin. Food Funct. 2020; 11(10): 8472–8492, doi: 10.1039/d0fo01598a, indexed in Pubmed: 32966476.
9. Fu J, Zhang Y, Yan T, et al. Comprehensive characterization of monoclonal antibody by Fourier transform ion cyclotron resonance mass spectrometry. MAbs. 2019; 11(1): 106–115, doi: 10.1080/19420862.2018.1525253, indexed in Pubmed: 30230956.
10. Pakradooni R, Shukla N, Gupta K, et al. Diosmetin Induces Modulation of Igf-1 and Il-6 Levels to Alter Rictor-Akt-PKCα Cascade in Inhibition of Prostate Cancer. J Clin Med. 2021; 10(20), doi: 10.3390/jcm10204741, indexed in Pubmed: 34682865.
11. Guo G, Dong J. Diosmetin attenuates oxidative stress-induced damage to lens epithelial cells via the mitogen-activated protein kinase (MAPK) pathway. Bioengineered. 2022; 13(4): 11072—11081, doi: 10.1080/21655979.2022.2068755, indexed in Pubmed: 35481411.
12. Wang SY, Sun ZL, Liu T, et al. Flavonoids from Sophora moorcroftiana and their synergistic antibacterial effects on MRSA. Phytother Res. 2014; 28(7): 1071–1076, doi: 10.1002/ptr.5098, indexed in Pubmed: 24338874.
13. Si Q, Shi Y, Huang D, et al. Diosmetin alleviates hypoxiainduced myocardial apoptosis by inducing autophagy through AMPK activation. Mol Med Rep. 2020; 22(2): 1335–1341, doi: 10.3892/mmr.2020.11241, indexed in Pubmed: 32627001.
14. Xie B, Pan D, Liu H, et al. Diosmetin protects against obesity and metabolic dysfunctions through activation of adipose estrogen receptors in mice. Mol Nutr Food Res. 2021; 65(17): e2100070, doi: 10.1002/mnfr.202100070, indexed in Pubmed: 34223710.
15. Juárez-Reyes K, Brindis F, Medina-Campos ON, et al. Hypoglycemic, antihyperglycemic, and antioxidant effects of the edible plant Anoda cristata. J Ethnopharmacol. 2015; 161: 36–45, doi: 10.1016/j.jep.2014.11.052, indexed in Pubmed: 25490313.
16. Gong X, Xiong Li, Bi C, et al. Diosmetin ameliorate type 2 diabetic mellitus by up-regulating Corynebacterium glutamicum to regulate IRS/PI3K/AKT-mediated glucose metabolism disorder in KK-Ay mice. Phytomedicine. 2021; 87: 153582, doi: 10.1016/j.phymed.2021.153582, indexed in Pubmed: 34091150.
17. Shi M, Wang J, Bi F, et al. Diosmetin alleviates cerebral ischemia-reperfusion injury through Keap1-mediated Nrf2/ARE signaling pathway activation and NLRP3 inflammasome inhibition. Environ Toxicol. 2022; 37(6): 1529–1542, doi: 10.1002/tox.23504, indexed in Pubmed: 35191607.
18. Li HL, Wei YY, Li XH, et al. Diosmetin has therapeutic efficacy in colitis regulating gut microbiota, inflammation, and oxidative stress via the circ-Sirt1/Sirt1 axis. Acta Pharmacol Sin. 2022; 43(4): 919–932, doi: 10.1038/s41401-021-00726-0, indexed in Pubmed: 34262136.

19. Chen Y, Wang Y, Liu M, et al. Diosmetin exhibits anti-proliferative and anti-inflammatory effects on TNF-α-stimulated human rheumatoid arthritis fibroblast-like synoviocytes through regulating the Akt and NF-κB signaling pathways. Phytother Res. 2020; 34(6): 1310–1319, doi: 10.1002/ptr.6596, indexed in Pubmed: 31833613.

20. Hu S, Huang Y, Chen Y, et al. Diosmetin reduces bone loss and osteoclastogenesis by regulating the expression of TRPV1 in osteoporosis rats. Ann Transl Med. 2020; 8(20): 1312, doi: 10.21037/atm-20-6309, indexed in Pubmed: 33209892.

21. Hsu YL, Kuo PL. Diosmetin induces human osteoblastic differentiation through the protein kinase C/p38 and extracellular signal-regulated kinase 1/2 pathway. J Bone Miner Res. 2008; 23(6): 949–960, doi: 10.1359/jbmr.080219, indexed in Pubmed: 18269307.

22. Shao S, Fu F, Wang Z, et al. Diosmetin inhibits osteoclast formation and differentiation and prevents LPS-induced osteolysis in mice. J Cell Physiol. 2019; 234(8): 12701–12713, doi: 10.1002/jcp.27887, indexed in Pubmed: 30515812.

23. Sharma S, Porwal K, Kulkarni C, et al. Diosmin, a citrus fruit-derived phlebotonic bioflavonoid protects rats from chronic kidney disease-induced loss of bone mass and strength without deteriorating the renal function. Food Funct. 2022; 13(4): 2184–2199, doi: 10.1039/d1fo03867b, indexed in Pubmed: 35119062.

24. Ding H, Ding H, Mu P, et al. Diosmetin inhibits subchondral bone loss and indirectly protects cartilage in a surgically-induced osteoarthritis mouse model. Chem Biol Interact. 2023; 370: 110311, doi: 10.1016/j.cbi.2022.110311, indexed in Pubmed: 36563736.

25. Glasson SS, Blanchet TJ, Morris EA. The surgical destabilization of the medial meniscus (DMM) model of osteoarthritis in the 129/SvEv mouse. Osteoarthritis Cartilage. 2007; 15(9): 1061–1069, doi: 10.1016/j.joca.2007.03.006, indexed in Pubmed: 17470400.

26. Obeidat AM, Kim SY, Burt KG, et al. A standardized approach to evaluation and reporting of synovial histopathology in two surgically induced murine models of osteoarthritis. Osteoarthritis Cartilage. 2024 [Epub ahead of print], doi: 10.1016/j.joca.2024.05.006, indexed in Pubmed: 38823432.

27. Glasson SS, Chambers MG, Van Den Berg WB, et al. The OARSI histopathology initiative — recommendations for histological assessments of osteoarthritis in the mouse. Osteoarthritis Cartilage. 2010; 18 Suppl 3: S17–S23, doi: 10.1016/j.joca.2010.05.025, indexed in Pubmed: 20864019.

28. Bonnet CS, Walsh DA. Osteoarthritis, angiogenesis and inflammation. Rheumatology (Oxford). 2005; 44(1): 7–16, doi: 10.1093/rheumatology/keh344, indexed in Pubmed: 15292527.

29. Daheshia M, Yao JQ. The interleukin 1beta pathway in the pathogenesis of osteoarthritis. J Rheumatol. 2008; 35(12): 2306–2312, doi: 10.3899/jrheum.080346, indexed in Pubmed: 18925684.

30. Lee DH, Park JK, Choi J, et al. Anti-inflammatory effects of natural flavonoid diosmetin in IL-4 and LPS-induced macrophage activation and atopic dermatitis model. Int Immunopharmacol. 2020; 89(Pt A): 107046, doi: 10.1016/j.intimp.2020.107046, indexed in Pubmed: 33045572.

31. Yu Ge, Wan R, Yin G, et al. Diosmetin ameliorates the severity of cerulein-induced acute pancreatitis in mice by inhibiting the activation of the nuclear factor-κB. Int J Clin Exp Pathol. 2014; 7(5): 2133–2142, indexed in Pubmed: 24966921.

32. Sun S, Yan Z, Shui X, et al. Astilbin prevents osteoarthritis development through the TLR4/MD-2 pathway. J Cell Mol Med. 2020; 24(22): 13104–13114, doi: 10.1111/jcmm.15915, indexed in Pubmed: 33063931.

33. Zhang M, Zhang R, Zheng T, et al. Xanthohumol attenuated inflammation and ECM degradation by mediating HO-1/C/EBPβ pathway in osteoarthritis chondrocytes. Front Pharmacol. 2021; 12: 680585, doi: 10.3389/fphar.2021.680585, indexed in Pubmed: 34017261.

34. Cook AE, Cook JL, Stoker AM. Metabolic responses of meniscus to IL-1β. J Knee Surg. 2018; 31(9): 834–840, doi: 10.1055/s-0037-1615821, indexed in Pubmed: 29294496.

35. Rahmati M, Nalesso G, Mobasheri A, et al. Aging and osteoarthritis: central role of the extracellular matrix. Ageing Res Rev. 2017; 40: 20–30, doi: 10.1016/j.arr.2017.07.004, indexed in Pubmed: 28774716.

36. Marcu KB, Otero M, Olivotto E, et al. NF-kappaB signaling: multiple angles to target OA. Curr Drug Targets. 2010; 11(5): 599–613, doi: 10.2174/138945010791011938, indexed in Pubmed: 20199390.

37. Choi MC, Jo J, Park J, et al. NF-κB signaling pathways in osteoarthritic cartilage destruction. Cells. 2019; 8(7), doi: 10.3390/cells8070734, indexed in Pubmed: 31319599.

38. Wang J, Ma J, Gu JH, et al. Regulation of type II collagen, matrix metalloproteinase-13 and cell proliferation by interleukin-1β is mediated by curcumin via inhibition of NF-κB signaling in rat chondrocytes. Mol Med Rep. 2017; 16(2): 1837–1845, doi: 10.3892/mmr.2017.6771, indexed in Pubmed: 28627596.

39. Shu C, Chen J, Lv M, et al. Plumbagin relieves rheumatoid arthritis through nuclear factor kappa-B (NF-κB) pathway. Bioengineered. 2022; 13(5): 13632–13642, doi: 10.1080/21655979.2022.2081756, indexed in Pubmed: 35653787.

40. Meephat S, Prasatthong P, Potue P, et al. Diosmetin ameliorates vascular dysfunction and remodeling by modulation of nrf2/ho-1 and p-JNK/p-NF-κB expression in hypertensive rats. Antioxidants (Basel). 2021; 10(9), doi: 10.3390/antiox10091487, indexed in Pubmed: 34573119.

41. Wu S, Liao X, Zhu Z, et al. Antioxidant and anti-inflammation effects of dietary phytochemicals: the Nrf2/NF-κB signalling pathway and upstream factors of Nrf2. Phytochemistry. 2022; 204: 113429, doi: 10.1016/j.phytochem.2022.113429, indexed in Pubmed: 36096269.

42. Miao Z, Dong M, Wang Ze, et al. Linalool inhibits the progression of osteoarthritis via the Nrf2/HO-1 signal pathway both in vitro and in vivo. Int Immunopharmacol. 2022; 113(Pt A): 109338, doi: 10.1016/j.intimp.2022.109338, indexed in Pubmed: 36330908.

43. Li W, Tao C, Mao M, et al. The Nrf2/HMGB1/NF-κB axis modulates chondrocyte apoptosis and extracellular matrix degradation in osteoarthritis. Acta Biochim Biophys Sin (Shanghai). 2023; 55(5): 818–830, doi: 10.3724/abbs.2023078, indexed in Pubmed: 37232576.

ORIGINAL PAPER

VM
VIA MEDICA

Dioscin attenuates lupus nephritis in NZB/W F1 mice by decreasing NF-κB activation and NLRP3 inflammasome

Yaling Xu[1], Han Li[2]

[1]Department of Nephrology, Wuhan Sixth Hospital, Wuhan, China

[2]Department of Geriatrics, Wuhan Sixth Hospital, Affiliated Hospital of Jianghan University, Wuhan, China

Abstract

Introduction. Dioscin, a natural steroid saponin, has anticancer, anti-inflammatory, anti-hyperlipidemic, and glycemic capabilities. This study focused on dioscin roles and its related mechanisms in experimental lupus nephritis.

Materials and methods. Lupus-prone NZB/W F1 mice were intragastrically administered with dioscin, prednisone or vehicle, and kidney, urine and blood samples were harvested after the mice were sacrificed. Proteinuria, blood urea nitrogen (BUN), creatinine, anti-dsDNA, IL-1β, and IL-18 levels in serum as well as IFN-γ, IL-6, IL-17 and TNF-α levels in kidney tissues were assessed. Renal histopathology was examined through hematoxylin-eosin staining. IgG and C3 expression in kidney was evaluated using immunofluorescence staining. The number of glomerular F4/80-positive cells and NLRP3-positive cells was determined by immunohistochemical staining. The protein expression was examined by western blotting.

Results. Dioscin alleviated lupus nephritis in NZB/W F1 mice. Dioscin declined serum anti-dsDNA level, prevented deposition of immune complexes in renal glomeruli, and inhibited the inflammatory response and infiltration of macrophages into mouse kidneys. Dioscin inhibited NF-κB and NLRP3 inflammasome in NZB/W F1 mice.

Conclusions. Dioscin ameliorates lupus nephritis through inhibition of NLRP3 inflammasome and NF-κB signaling.
(Folia Histochem Cytobiol 2024; 62, 2: 110–121)

Keywords: mouse; osteoarthritis; chondrocytes; diosmetin; ECM proteins; Nrf2/HO-1; NF-κB

INTRODUCTION

Systemic lupus erythematosus (SLE) refers to an autoimmune disorder involving one or more organs. Epidemiological research suggests that 0.4 million individuals are newly diagnosed with SLE worldwide, and the yearly incidence of SLE is 5.14 per 100,000 people [1]. Lupus nephritis, a frequent and severe manifestations of SLE, occurs in approximately 40% of SLE patients within 5 years, and approximately 4.3–10.1% of patients with lupus nephritis develop end-stage renal disease [2]. Renal dysfunction with inflammatory response and glomerulonephritis resulting in proteinuria is the major characteristics of lupus nephritis [3]. IgG, IgA, IgM, C1q and C3 are recognized as pathological biomarkers of lupus nephritis [4]. In human lupus nephritis, substantial infiltration of inflammatory cells, mainly macrophages, is observed in kidneys [5]. It has been reported that anti-dsDNA antibodies have diagnostic and prognostic values in lupus nephritis [6]. Currently, corticosteroids and cyclophosphamide are widely used for lupus nephritis treatment. Despite therapeutic improvements, lupus nephritis can increase mortality risk in SLE patients [7]. Thus, exploring the pathomechanisms associated with lupus nephritis and developing novel therapies for lupus nephritis treatment are urgently needed.

Correspondence address:
Han Li
Department of Geriatrics, Wuhan Sixth Hospital,Affiliated
Hospital of Jianghan University, Wuhan, China
e-mail: LiHan19931206@163.com

The NLRP3 inflammasome consists of NLRP3, ASC protein and pro-cascpase-1 [8]. Patients with lupus nephritis exhibit higher levels of NLRP3 inflammasome, IL-1β, and IL-18 in the kidney than healthy controls [9, 10]. In several lupus nephritis mouse models, the NLRP3 inflammasome and its components are upregulated in the kidney [11, 12]. In lupus nephritis, activation of NLRP3 inflammasome in podocytes can lead to severe proteinuria [13, 14]. Inactivation of NLRP3 inflammasome has been shown to ameliorate severe lupus nephritis in mice [13, 15, 16].

NF-κB, transcription factor, is a critical inflammation regulator [17]. Under steady state, NF-κB is sequestered by IκB in cytosol. Upon activation, the kinase complex phosphorylates and degrades IκB, inducing nuclear translocation of NF-κB [18]. Activated NF-κB and elevated inflammatory cytokines were observed in glomeruli of lupus nephritis patients, and the lupus nephritis severity is associated with NF-κB activation [19]. NF-κB inactivation can ameliorate lupus nephritis pathogenesis [20, 21].

Dioscin, a natural steroid saponin, is an active ingredient in Dioscoreaceae herbs, and its anti-carcinogenic, anti-inflammatory, anti-hyperlipidemic and glycemic properties have been well-established [22]. The renoprotective effects of dioscin have been previously documented. For example, dioscin suppresses inflammation and renal ischemia/reperfusion injury *via* inactivating TLR4/MyD88 signaling [23]. Additionally, dioscin exerts protective effects against renal fibrosis by inhibiting the inflammatory response mediated by NF-κB signaling [24]. Moreover, dioscin alleviates diabetic nephropathy in mice by blocking TLR4/NF-κB signaling [25]. Furthermore, dioscin has been found to alleviate silica-aggravated SLE through inhibiting apoptosis and improving LC3-associated phagocytosis in MPL/lpr mice [26]. The effect of dioscin on inactivating NLRP3 inflammasome in periodontitis has also been reported previously [27]. Given the above, we speculated that dioscin might alleviate lupus nephritis.

Consequently, this study focused on dioscin roles and its related mechanisms in lupus nephritis. We hypothesized that dioscin might attenuate lupus nephritis pathomechanisms. This study provides evidence for the therapeutic potential of dioscin in the treatment of lupus nephritis.

MATERIALS AND METHODS

Animals

Female NZB/W F1 mice (21 weeks of age; Slack Laboratory, Shanghai, China) and wild-type C57BL/6 mice (Charles River Laboratories, Beijing, China) were housed in a specific pathogen-free animal research facility at $25 \pm 2°C$ with 65% of humidity under a 12-h light/dark cycle. The mice were divided into 4 groups, namely control group, NZB/W F1 group, NZB/W F1 + Dioscin group, and NZB/W F1 + Prednisone group. Each group had 10 mice. Dioscin (60 mg/kg; purity 99.76%, MedChemExpress, Shanghai, China) and prednisone (purity 99.84%; MedChemExpress) were dissolved in 0.5% sodium carboxymethyl cellulose (CMC-Na; Sigma-Aldrich, Shanghai, China) solution in distilled water. Mice were intragastrically administered with dioscin (60 mg/kg), prednisone (5 mg/kg) or vehicle (0.5% CMC-Na) from 23 weeks of age (3 times/week). The mice were sacrificed under isoflurane anesthesia at 30 weeks of age (Fig 1A). Urine and blood samples were collected followed by collection of kidney tissues. The dioscin and prednisone doses were determined according to previous publications [25, 28]. Laboratory procedures were approved by Ethics Committee of Wuhan Sixth Hospital. All the animal care was performed according to the Guide for Care and Use of Laboratory Animals.

Renal injury assessment

Following treatment, mice were individually placed in metabolic cages, and spot urine was collected from each mice using the bladder massage method [29], and urine protein level was evaluated by a Coomassie brilliant blue dye-binding assay (Sigma-Aldrich, St Louis, MO, USA).

Fresh blood was harvested from abdominal aorta, followed by a 15-min centrifugation at 3000 rpm. The blood urea nitrogen (BUN) and creatinine levels in serum were measured using QuantiChrom urea and creatinine assay kits (Nanjing Jiancheng Bioengineering Institute, Nanjing, China) and a HITACHI-7080 automatic biochemical analyzer.

Renal histopathology

After sacrificing the animals, the kidneys were resected, fixed overnight in 4% paraformaldehyde, paraffin-embedded, and cut into 5-μm sections. Then, the sections were stained with hematoxylin-eosin (H&E; Sigma-Aldrich) and visualized using a light microscope (Olympus, Tokyo, Japan). The tubular and glomerular damages were scored semi-quantitatively on the previously described scoring system by two independent pathologists [30, 31]. Glomerular pathology was evaluated by assessing 60–80 glomeruli per kidney, and each glomerulus was scored on a semiquantitative scale: 0, no change, normal glomerulus; 1, lining of capillaries to Bowman's capsule; 2, accumulation of mesangial matrix in 25% of the glomerulus; 3, accumulation of

mesangial matrix in 50% of the glomerulus and capillary obliteration; 4, accumulation of mesangial matrix in 75% of the glomerulus. The tubular injury was scored according to the percentage of damage including atrophy, flattening of proximal tubule epithelial cells, and tubular dilation in 10 randomly selected fields on a scale of 0–5 at a magnification of 200×: 0, no change; 1, < 20% damage; 2, 20–40% damage; 3, 40–60% damage, 4, 60–80% damage; and 5, > 80% damage.

Enzyme-linked immunosorbent assay (ELISA) assay

Kidney tissues were homogenized in ice-cold 0.9% NaCL solution using a glass-Teflon homogenizer and then centrifuged at 3000 *g* for 20 min at 4℃, followed by collection of the supernatants for assessing IFN-γ, IL-6, IL-17 and TNF-α levels using commercially available ELISA kits (Cusabio, Wuhan, China). The anti-dsDNA, IL-1β and IL-18 levels in serum were also estimated *via* ELISA kits. The mouse ELISA kits included IFN-γ (CSB-E04578m), IL-6 (CSB-E04639m), IL-17 (CSB-E04608m), TNF-α (CSB-E04741m) anti-dsDNA antibodies (CSB-E12911m), IL-1β (CSB-E08054m) and IL-18 (CSB-E04609m).

Immunofluorescence staining

Kidney tissues were embedded in OCT compound (MaoKang Biotechnology, Shanghai, China), frozen at –70℃, and then cut into 5 μm-thick sections using a cryostat at –20℃. Subsequently, the sections were blocked in Tris buffered saline with Tween (TBST; pH 7.5; Yeasen, Shanghai, China) containing 1% normal goat serum for 30 min. Thereafter, the sections were incubated with mouse anti-IgG antibodies (1:50; 406601, Biolegend, Beijing, China) or rabbit anti-C3 antibodies (ab97462, 1:100; Abcam, Shanghai, China) overnight at 4℃, followed by incubation with Alexa Fluor 594 goat anti-mouse IgG (ab150116, 1:200; Abcam) or Alexa Fluor 488 goat anti-rabbit IgG (ab150077, 1:200; Abcam) for 1 h at room temperature. The sections were then placed in phosphate-buffered saline (PBS; Beyotime, Shanghai, China), washed three times for 5 min each, and counterstained with 4',6-diamidino-2-phenylindole (DAPI; Beyotime). The sections were again placed in PBS and washed three times for 5 min each with shaking on a decolorization shaker. When the sections had dried slightly, a small amount of anti-fluorescence quenching agent was dropped onto each slide, and the slide was sealed with resin mounting agent. Finally, the sections were observed under a fluorescence microscope (BX63, Olympus, Tokyo, Japan).

Reverse transcription quantitative polymerase chain reaction (RT-qPCR)

Total RNA was extracted using TRIzol reagent (Sigma-Aldrich), and total RNA (1 μg) was reverse transcribed into cDNA using a PrimeScript RT reagent kit (Takara, Beijing, China). Subsequently, RT-qPCR was performed using the TaqMan Gene Expression Assays Protocol (Thermo Fisher Scientific, Shanghai, China). The amplification conditions included 10 min at 95℃ for initialization, followed by denaturation at 95℃ for 15 s and 60℃ for 30 s with 40 cycles. GAPDH served as the reference gene. Relative mRNA expressions were quantified using the $2^{-\triangle\triangle Ct}$ method [32]. The primer sequences used in this study were listed in Table 1.

Immunohistochemical staining

Samples of kidney cortex and medulla were fixed in 10% neutral-buffered formalin solution (MaoKang Biotechnology) overnight at room temperature, dehydrated, paraffin-embedded, and cut into 3 μm-thick sections. Then, the sections were de-paraffinized to water and incubated in 3% H_2O_2 for 10 min to eliminate endogenous peroxidase activity, followed by antigen retrieval. Subsequently, the sections were soaked in PBS (5 min, two times), blocked with 10% normal goat serum and incubated at room temperature for 30 min. Thereafter, the sections were incubated with primary antibodies against rabbit anti-F4/80 antibodies (ab300421, 1:500; Abcam) and rabbit anti-NLRP3 antibodies (MA5-32255, 1:100; Thermo Fisher Scientific) overnight at 4℃. Next, the sections were washed with PBS and incubated with Alexa Fluor 488 goat anti-rabbit IgG (ab150077, 1:500; Abcam) for

Table 1. Sequences of primers used for reverse transcription-quantitative PCR

| Gene (mice)	Sequence (5'→3')
IFN-γ forward	AGCAAGGCGAAAAAGGATGC
IFN-γ reverse	TCATTGAATGCTTGGCGCTG
IL-6 forward	TGTATGAACAACGATGATGCAC
IL-6 reverse	TGGTACTCCAGAAGACCAGAGG
IL-17 forward	ACCGCAATGAAGACCCTGAT
IL-17 reverse	CAGGATCTCTTGCTGGATGAGA
TNF-α forward	CGAGTGACAAGCCTGTAGCC
TNF-α reverse	GAGAACCTGGGAGTAGACAAGG
GAPDH forward	TCCGCCCCTTCTGCCGATG
GAPDH reverse	CACGGAAGGCCATGCCAGTGA
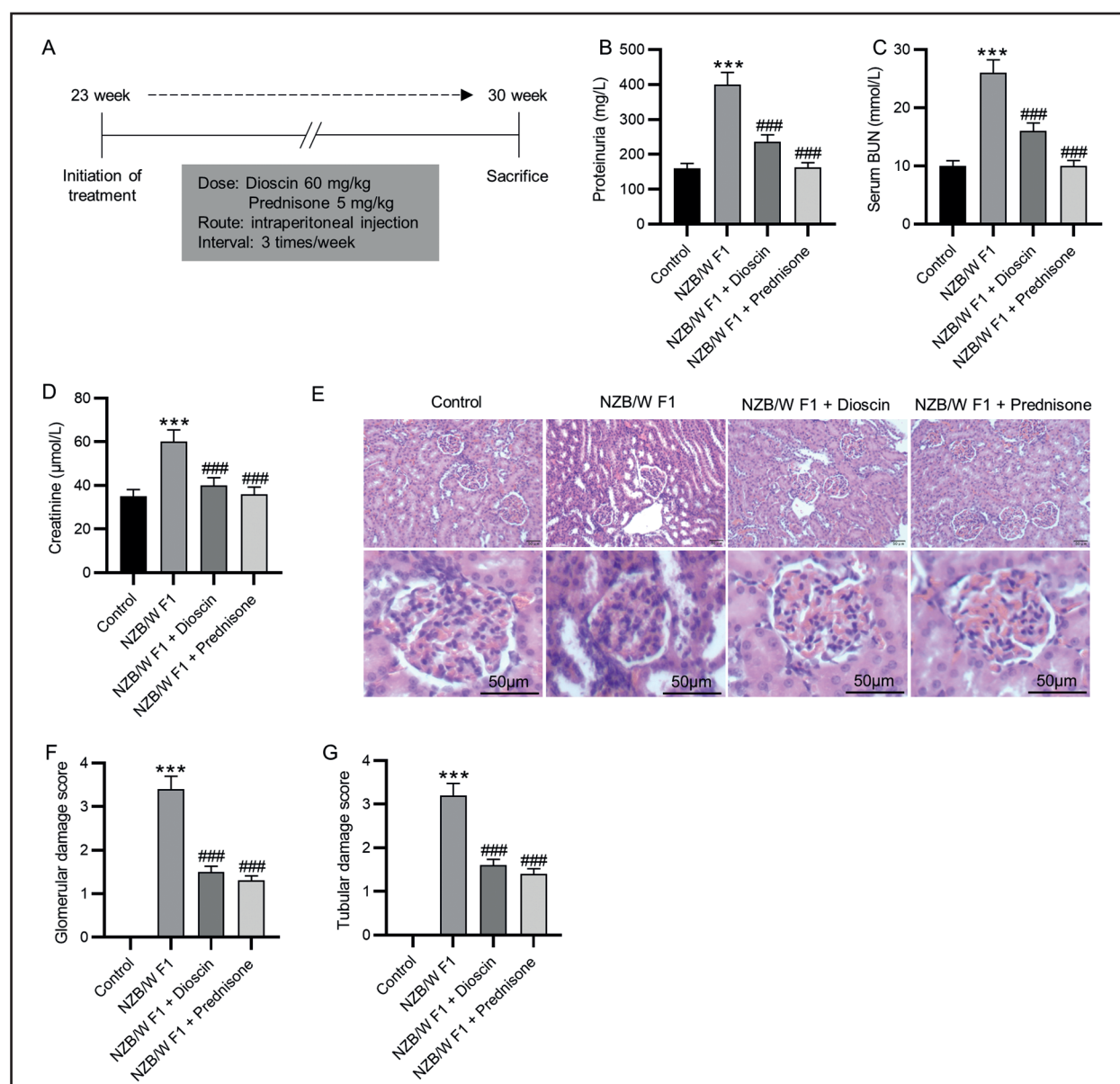
Figure 1. Dioscin alleviates the pathological features of lupus nephritis in NZB/W F1 mice. **A.** Treatment schedule for NZB/W F1 mice with PBS (vehicle), dioscin (60 mg/kg) and prednisone (5 mg/kg). **B–D.** The levels of proteinuria, serum BUN and creatinine in the control, the NZB/W F1, the dioscin and the prednisone groups. **E.** Representative images of HE staining in the renal tissues. F, G. Quantitative analysis of glomerular and tubular damage scores in renal tissues. There were five mice used in each group. The data indicated the mean SD of three independent experiments. ***$P < 0.001$ *vs.* control group; ###$P < 0.001$ *vs.* NZB/W F1 group.

2 h at 37°C. The HRP-labelled streptavidin (Beyotime, Shanghai, China) was added for incubation at 37°C for 20 min. The sections were developed with 3',3-diaminobenzidine (Sigma-Aldrich) and counter-stained with hematoxylin (Sigma-Aldrich) for 1 min. The mounted sections were observed under a microscope (CKX31, Olympus) after immersing in 1% ammonia water to return blue in color. Five high-power field views per slice both in cortex and medulla were randomly selected with 400 cells per field of view.

Western blotting

Total protein in kidney tissues was lysed in RIPA lysis buffer (Beyotime) containing protease inhibitor and phosphatase inhibitor (MedChemExpress). After being quantified with a BCA Protein Assay kit (Beyotime), protein samples (30 μg) were resolved by sodium dodecyl sulfate-polyacrylamide gel electrophoresis and transferred to polyvinylidene difluoride membranes. Then, the membranes were blocked with 5% skimmed milk in PBS solution with
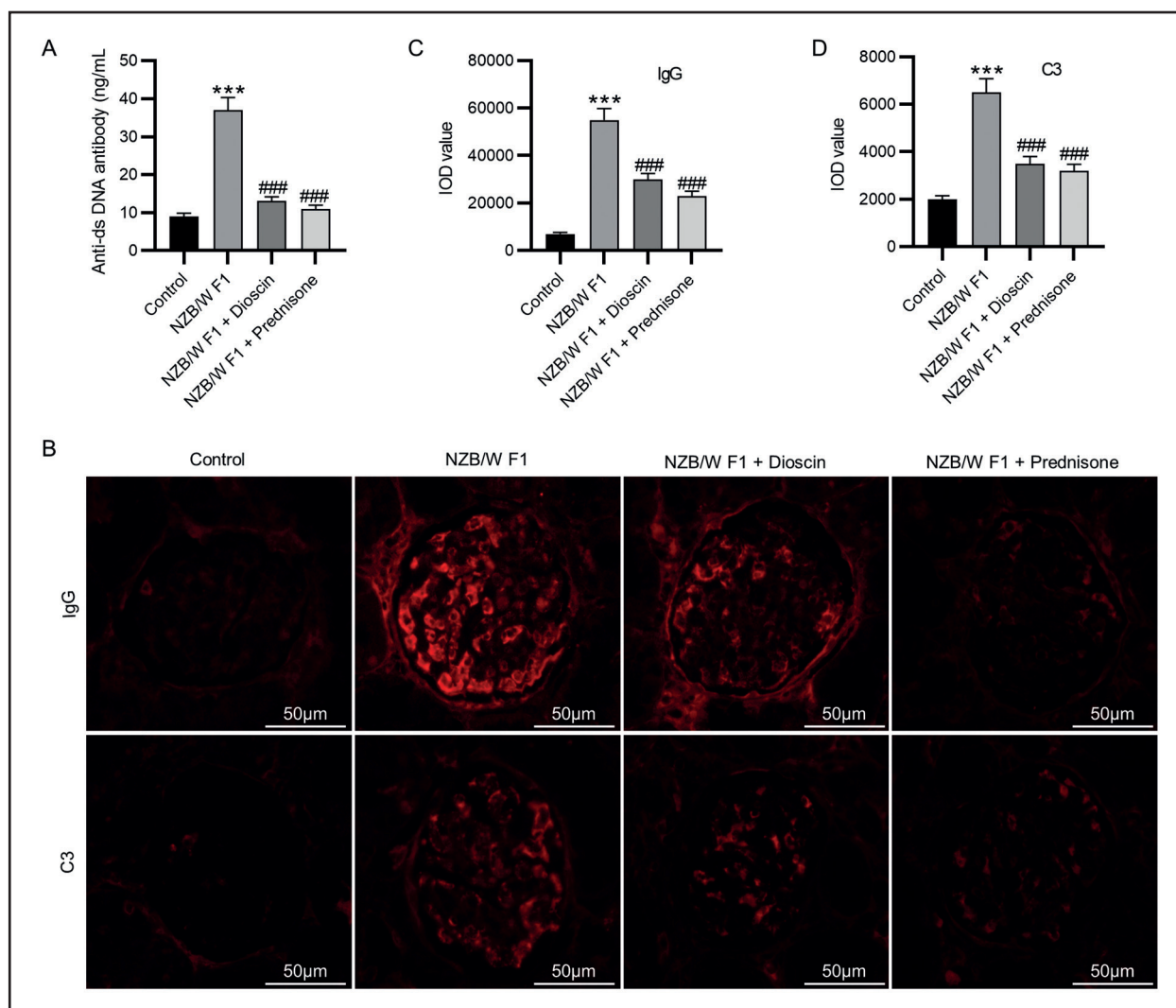
Figure 2. Dioscin reduces serum anti-dsDNA level and glomerular deposition of IgG and C3 in NZB/W F1 mice. **A.** The levels of serum anti-dsDNA antibodies were measured by ELISA. **B.** Representative immunofluorescence staining images for IgG and C3 deposition in the kidney glomeruli. **C, D.** Quantitative analysis of IgG and C3 deposition in the glomeruli, presented as the IOD value (integrated optical density value). The data indicated the mean SD of three independent experiments, n = 5 in each group. ***P < 0.001 *vs*. control group; ###P < 0.001 *vs*. NZB/W F1 group.

0.05% Tween (PBST; Thermo Fisher Scientific) for 1 h at room temperature and incubated with rabbit anti-p-NF-κB p65 antibodies (ab76302, 1:1000; Abcam), rabbit anti-IκB antibodies (ab92700, 1:1000; Abcam), mouse anti-β-actin antibodies (ab8226, 1:1000; Abcam), rabbit anti-NF-κB p65 antibodies (ab32536, 1:2000; Abcam), rabbit anti-histone H3 antibodies (ab1791, 1:1000; Abcam), rabbit anti-N-LRP3 antibodies (ab263899, 1:1000; Abcam), rabbit anti-cleaved caspase-1 antibodies (#89332, 1:1000; Cell Signaling Technology, Shanghai, China), and rabbit anti-IL-1β antibodies (ab283818, 1:1000; Abcam) at 4°C overnight. Subsequently, the membranes were washed with PBST and incubated with

corresponding horseradish peroxidase-conjugated secondary antibodies for 1 h at room temperature. Immunoblots were developed using enhanced chemiluminescence reagent (Beyotime). Densitometric analysis was performed using ImageJ software (Bio-Rad, Hercules, CA, USA).

Statistical analysis

The data were analyzed using GraphPad Prism 9.0 (GraphPad, San Diego, CA, USA) and expressed as the mean ± standard deviation (SD). One-way analysis of variance followed by Tukey *post hoc* test was used for comparisons among groups. P < 0.05 was considered statistically significant.
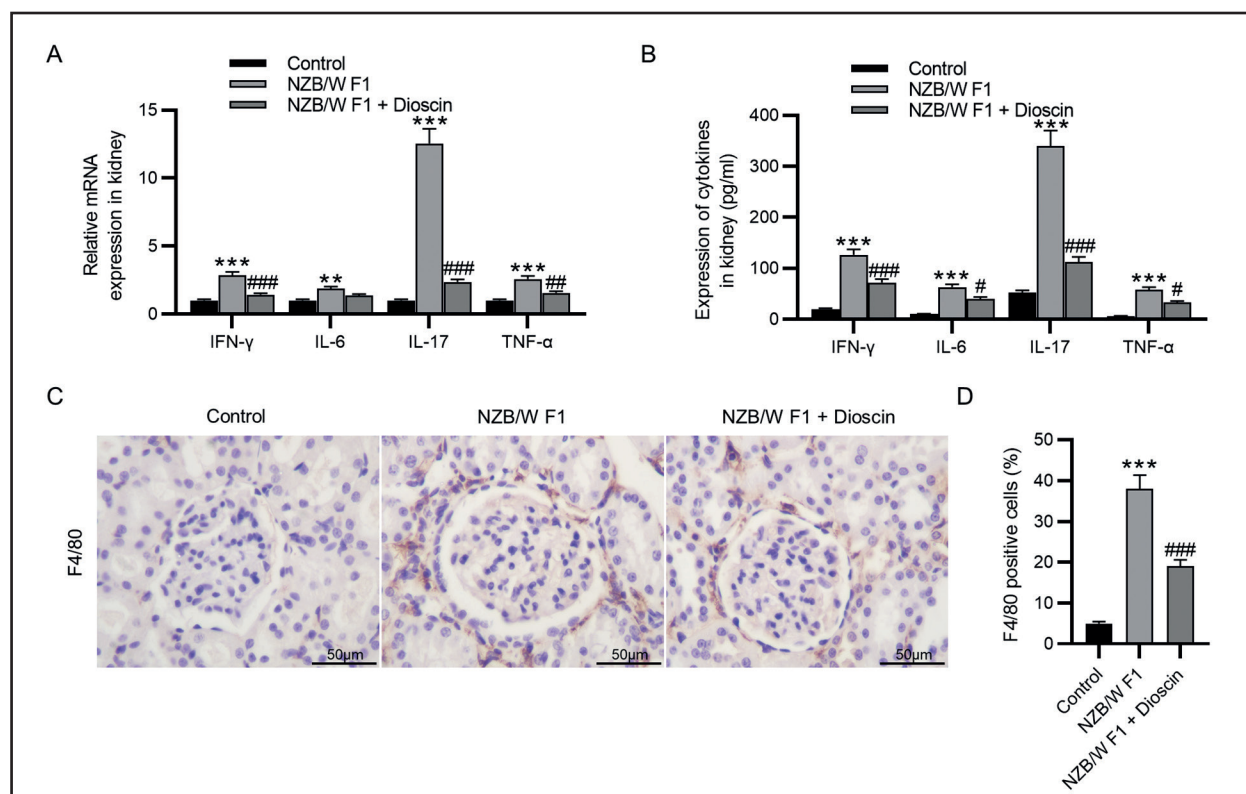
Figure 3. Dioscin inhibits the inflammatory response and infiltration of macrophages into the kidneys of NZB/W F1 mice. **A, B.** The mRNA and protein levels of IFN-γ, IL-6, IL-17 and TNF-α in mouse kidney tissues were estimated by RT-qPCR and ELISA. **C, D.** Macrophage infiltration was detected by immunohistochemistry staining. N = 5 in each group. **P < 0.01, ***P < 0.001 *vs.* control group; $^{#}$P < 0.05, $^{###}$P < 0.001 *vs.* NZB/W F1 group.

RESULTS

Dioscin alleviates lupus nephritis

To investigate dioscin roles in lupus nephritis, we used NZB/W F1 mice. NZB/W F1 mice had higher proteinuria and serum BUN and creatinine concentrations than WT mice, whereas administration of dioscin or prednisone greatly lowered proteinuria and serum BUN and creatinine levels (Fig. 1B–D). Then, HE staining showed that NZB/W F1 mice presented obvious glomerular and tubular damages, such as glomerular expansion, hypercellularity, interstitial inflammation, crescents, increased mesangial matrix and tubular cast deposition. These severe renal lesions were greatly reduced by administration of dioscin or prednisone (Fig. 1E). The quantitative analyses of glomerular and tubular damage scores demonstrated that compared with the control group, the NZB/W F1 group exhibited significantly higher damage scores. However, dioscin or prednisone treatment remarkably decreased the damage scores in NZB/W F1 mice (Fig. 1F, G). These results demonstrate that dioscin significantly attenuates kidney injury in NZB/W F1 mice.

Dioscin declines serum anti-dsDNA and glomerular IgG and C3 deposits

As shown by ELISA, the lupus-prone NZB/W F1 mice exhibited significantly higher serum anti-dsDNA levels than control animals, whereas administration of dioscin or prednisone decreased them (Fig. 2A). The immunofluorescence staining was performed to assess immune complex deposition of IgG and C3. The fluorescence intensities of antibodies labeling for IgG and C3 greatly increased in NZB/W F1 mice, which were reduced after dioscin or prednisone treatment (Fig. 2B–D).

Dioscin inhibits inflammatory response and macrophage infiltration in lupus-prone mice

The results of RT-qPCR and ELISA demonstrated that mRNA and protein levels of IFN-γ, IL-6, IL-17 and TNF-α expression in homogenates of NZB/W F1 mice kidneys were significantly higher than those in control mice, whereas administration of dioscin decreased them in NZB/W F1 mice (Fig. 3A, B). Then, we detected macrophage marker expression (F4/80) in the kidney. As shown by immunohistochemical staining, the NZB/W F1 mice showed profound infiltration of
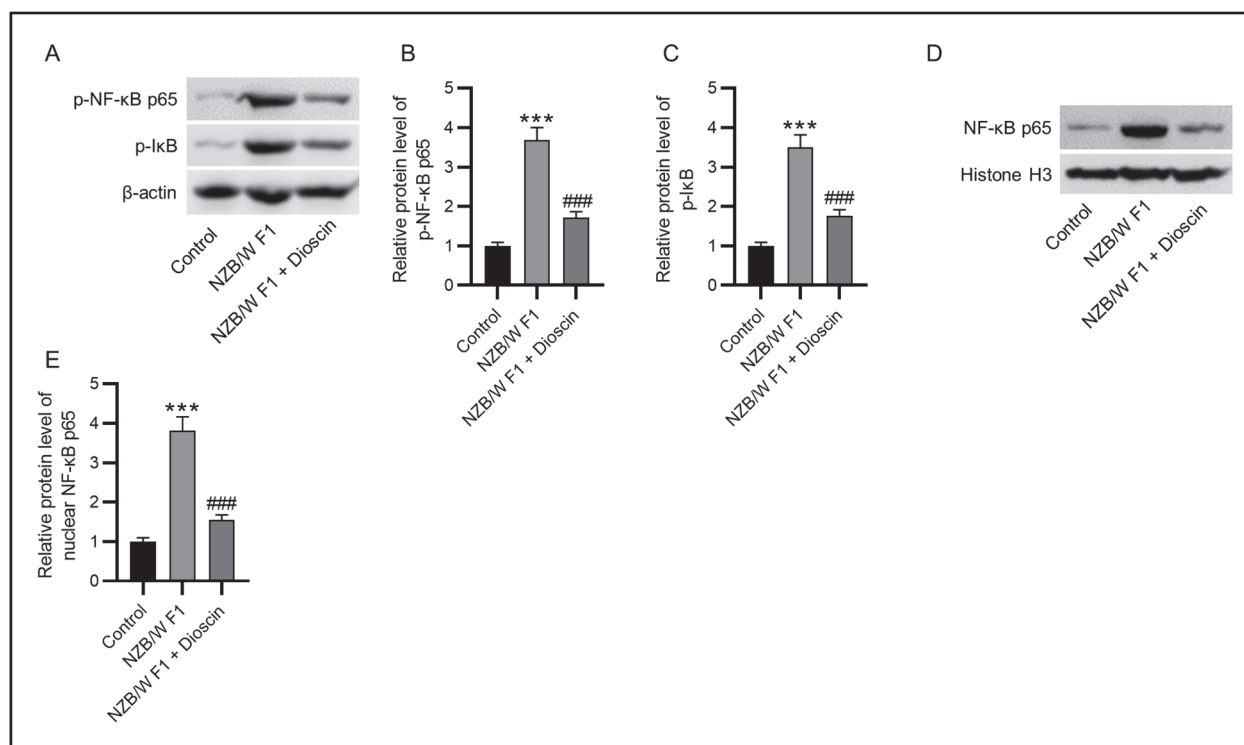
Figure 4. Dioscin inactivates NF-κB signaling in the kidneys of NZB/W F1 mice. **A–C.** The protein levels of p-NF-κB p65 and p-IκB in renal tissues were measured by western blotting. **D, E.** Nuclear NF-κB p65 was determined by western blotting. N= 5 in each group. ***$P < 0.001$ *vs.* control group; ###$P < 0.001$ *vs.* NZB/W F1 group.

F4/80-positive macrophages in renal tissues, whereas administration of dioscin resulted in a significantly decreased proportion of F4/80-positive inflammatory cells in kidneys of lupus-prone mice (Fig. 3C, D).

Dioscin inactivates NF-κB signaling in kidneys of lupus-prone mice

As western blotting revealed, compared with control mice, NZB/W F1 mice had remarkably elevated protein levels of p-NF-κB p65 and p-IκB, whereas treatment with dioscin effectively downregulated their levels (Fig. 4A–C). Additionally, the nuclear translocation of NF-κB p65 was remarkably inhibited by dioscin in NZB/W F1 mice (Fig. 4D, E).

Dioscin restrains NLRP3 inflammasome activation in kidneys of lupus-prone mice

The concentrations of IL-1β and IL-18 in serum of NZB/W F1 mice were visibly upregulated than those in control mice, whereas treatment with dioscin markedly decreased their levels (Fig. 5A, B). Immunohistochemistry staining results demonstrated that NLRP3 upregulation in NZB/W F1 mice was inhibited after dioscin administration (Fig. 5C, D). Western blotting analysis revealed that the NZB/W F1

mice had notably higher NLRP3, cleaved caspase-1, and IL-1β protein level in kidney homogenates than controls, whereas administration of dioscin reversed these changes (Fig. 5E–H).

Figure 6 presents the schematic diagram based on the results of this study that suggests the mechanisms by which dioscin alleviates lupus nephritis in the mouse model acting through inhibiting NLRP3 inflammasome and NF-κB activation.

DISCUSSION

Lupus nephritis is an immune complexes-mediated glomerulonephritis and occurs in approximately 40% of patients diagnosed with SLE within 5 years. Despite great improvements in lupus nephritis outcomes over the past decades, the risk of kidney failure is 22% for all lupus nephritis classes and 44% for class IV lupus nephritis within 15 years of lupus nephritis diagnosis [33]. Therefore, developing novel agents for the treatment of lupus nephritis is urgent. Dioscin is an active ingredient of Dioscoreaceae herbs, and increasing evidence has shown its anti-inflammatory and renoprotective effects [24, 25, 34]. However, the potential roles and related mechanisms of dioscin in lupus nephritis remain uncertain. We used NZB/W F1
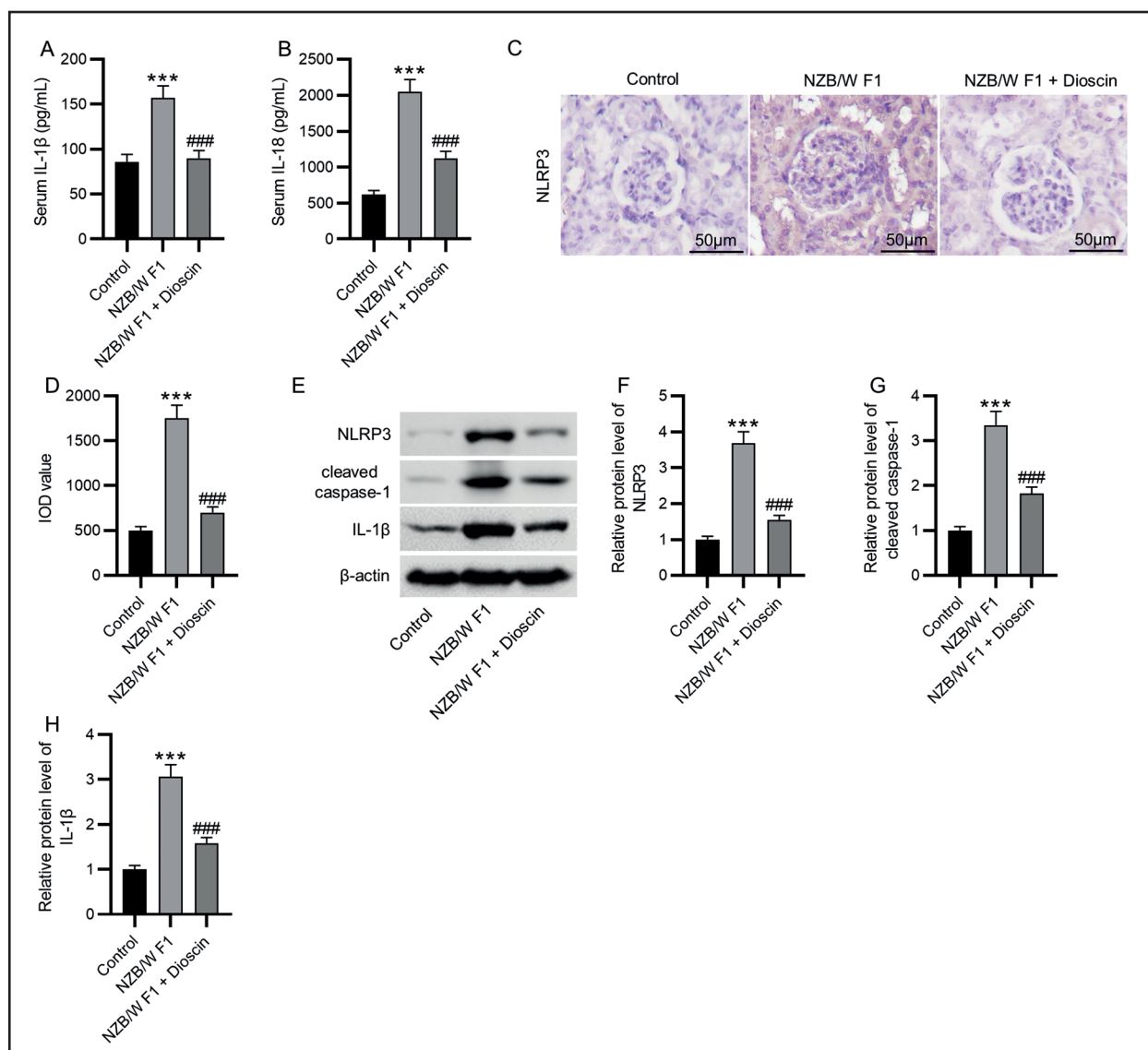
Figure 5. Dioscin restrains NLRP3 inflammasome activation in the kidneys of NZB/W F1 mice. **A, B.** The serum levels of IL-1β and IL-18 were estimated by ELISA. **C, D.** Immunohistochemistry staining of NLRPS in kidney tissues. **E–H.** Western blotting to measure the protein levels of NLRP3, cleaved caspase-1 and IL-1β. N = 5 in each group. ***P < 0.001 *vs.* control group; ###P < 0.001 *vs.* NZB/W F1 group.

mice to investigate the potential effect of dioscin in lupus nephritis pathologies. Our findings revealed that dioscin attenuated lupus nephritis by decreasing proteinuria, serum BUN and serum creatinine and alleviating glomerular and tubular damage. Mechanistically, dioscin suppressed the activations of NLRP3 inflammasome and NF-κB.

Formation and deposition of immune complexes in blood vessels and renal glomeruli, resulting in complement activation, the synthesis of inflammatory mediators, immune cell infiltration, proteinuria, and renal fibrosis, is critical in lupus nephritis pathophysiology [35]. Macrophages, innate immune cells, are widely distributed and infiltrated in the kidney and regulate renal immune responses [36]. In lupus nephritis patients, the efferocytosis activity of macrophages is reduced, leading to deficient clearance of apoptotic cells, pro-inflammatory polarization of macrophages, secretion of inflammatory factors, and tissue destruction [37]. As reported, TNF-α, IL-6, IL-17 and IFN-γ are involved in glomerulonephritis pathogenesis [38]. Herein, elevated anti-dsDNA, TNF-α, IL-6, IL-17, and IFN-γ levels, increased glomerular IgG and C3 deposits, and renal infiltration of macrophages were observed in lupus-prone mice. Dioscin can alleviate IgA nephropathy by inhibiting excessive activation of IgA-secreting cells [39]. Additionally, dioscin has been found to inhibit macrophage M1 polarization and
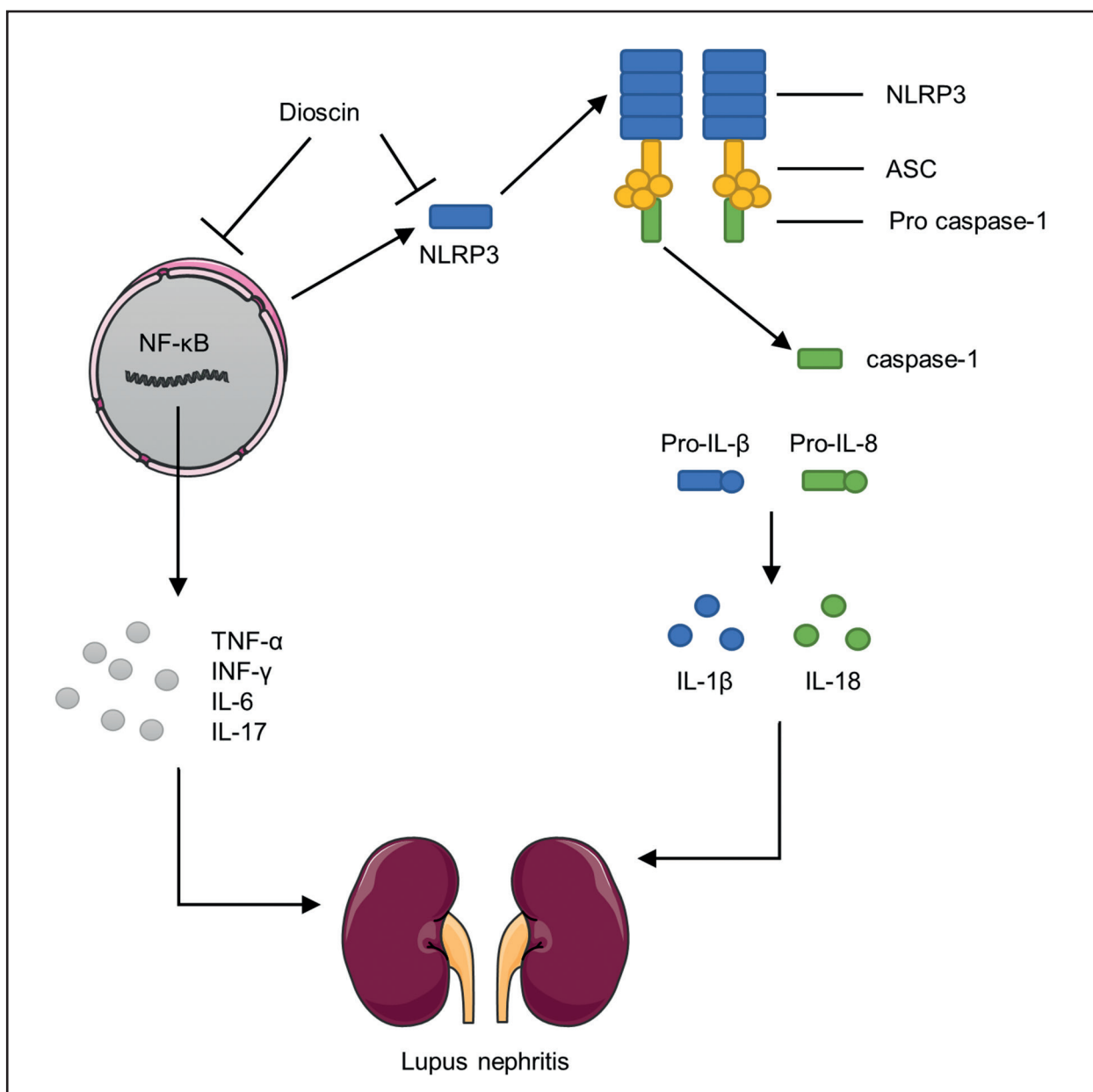
Figure 6. Schematic diagram depicts the mechanisms by which dioscin alleviates lupus nephritis. Dioscin ameliorates lupus nephritis through inhibiting NLRP3 inflammasome and NF-κB activation.

macrophage-derived inflammation, thereby ameliorating murine ulcerative colitis [40], inflammatory bowel disease [41] and pulmonary fibrosis [42]. The current study revealed that dioscin downregulated serum anti-dsDNA concentrations and decreased glomerular IgG and C3 deposition. Additionally, dioscin also decreased TNF-α, IL-6, IL-17 and IFN-γ levels and inhibited macrophage infiltration in NZB/W F1 mice.

The NLRP3 inflammasome is activated in macrophages isolated from lupus patients [43]. Inflammatory stimuli can activate NLRP3 inflammasome and subsequently induce caspase-1 activation and IL-1β and

IL-18 release [44]. Blockade of the NLRP3 inflammasome is found to attenuate lupus nephritis in MRP/lpr mice [16]. NF-κB is a transcription factor. Once the IκB kinase complexes phosphorylate IκB, nuclear translocation of NF-κB appears, initiating inflammation [45]. In the current study, NZB/W F1 mice exhibited activation of NLRP3 inflammasome. Additionally, increased NF-κB p65 and IκB phosphorylation and elevated nuclear NF-κB p65 expression were observed in NZB/W F1 mice. These findings revealed NLRP3 inflammasome and NF-κB activations in NZB/W F1 mice. Dioscin was shown to prevent experimental

gouty arthritis, mastitis, colitis, periodontitis and diabetes cognitive dysfunction by inhibiting NLRP3 inflammasome activation [27, 46–49]. Additionally, dioscin can ameliorate renal fibrosis, diabetic nephropathy and inflammatory kidney injury by inactivating NF-κB signaling [24, 25, 50]. Our study demonstrated that dioscin inactivated NLRP3 inflammasome and NF-κB signaling in lupus-prone NZB/W F1 mice.

In conclusion, dioscin ameliorates lupus nephritis through inactivating NLRP3 inflammasome and NF-κB. However, there are some limitations to this study. First, the MRL/lpr mouse model recapitulates many of the clinical manifestations and immune dysregulation observed in human SLE [51]. Experiments should also be conducted in MRL/lpr mice. Second, dioscin roles in podocyte injury, autophagy and oxidative stress in lupus nephritis should be determined. Third, the safety of dioscin in clinical practice remains unknown. Despite these limitations, our findings provide support for the clinical translation of dioscin as novel treatment for lupus nephritis.

Article information and declarations

Data availability statement
The datasets used or analyzed during the current study are available from the corresponding author on reasonable request.

Ethics statement
Laboratory procedures were approved by Ethics Committee of Wuhan Sixth Hospital. All the animal care was performed according to the Guide for Care and Use of Laboratory Animals.

Author contributions
Yaling Xu conceived and designed the experiments. Yaling Xu and Han Li carried out the experiments. Yaling Xu and Han Li analyzed the data. Yaling Xu and Han Li drafted the manuscript. All authors agreed to be accountable for all aspects of the work. All authors have read and approved the final manuscript.

Conflict of interest
The authors declare that they have no competing interests.

REFERENCES

1. Tian J, Zhang D, Yao Xu, et al. Global epidemiology of systemic lupus erythematosus: a comprehensive systematic analysis and modelling study. Ann Rheum Dis. 2023; 82(3): 351–356, doi: 10.1136/ard-2022-223035, indexed in Pubmed: 36241363.
2. Hanly JG, O'Keeffe AG, Su Li, et al. The frequency and outcome of lupus nephritis: results from an international inception cohort study. Rheumatology (Oxford). 2016; 55(2): 252–262, doi: 10.1093/rheumatology/kev311, indexed in Pubmed: 26342222.
3. Li D, Shi G, Wang J, et al. Baicalein ameliorates pristane-induced lupus nephritis via activating Nrf2/HO-1 in myeloid-derived suppressor cells. Arthritis Res Ther. 2019; 21(1): 105, doi: 10.1186/s13075-019-1876-0, indexed in Pubmed: 31023362.
4. Kudose S, Santoriello D, Bomback A, et al. Sensitivity and specificity of pathologic findings to diagnose lupus nephritis. Clin J Am Soc Nephrol. 2019; 14(11): 1605–1615, doi: 10.2215/cjn.01570219, indexed in Pubmed: 31653670.
5. Chalmers SA, Chitu V, Ramanujam M, et al. Therapeutic targeting of macrophages in lupus nephritis. Discov Med. 2015; 20(108): 43–49, indexed in Pubmed: 26321086.
6. Yung S, Cheung KF, Zhang Q, et al. Anti-dsDNA antibodies bind to mesangial annexin II in lupus nephritis. J Am Soc Nephrol. 2010; 21(11): 1912–1927, doi: 10.1681/ASN.2009080805, indexed in Pubmed: 20847146.
7. Anders HJ, Saxena R, Zhao MH, et al. Lupus nephritis. Nat Rev Dis Primers. 2020; 6(1): 7, doi: 10.1038/s41572-019-0141-9, indexed in Pubmed: 31974366.
8. Fu J, Wu H. Structural mechanisms of NLRP3 inflammasome assembly and activation. Annu Rev Immunol. 2023; 41: 301––316, doi: 10.1146/annurev-immunol-081022-021207, indexed in Pubmed: 36750315.
9. Latz E, Xiao TS, Stutz A. Activation and regulation of the inflammasomes. Nat Rev Immunol. 2013; 13(6): 397–411, doi: 10.1038/nri3452, indexed in Pubmed: 23702978.
10. Huang T, Yin H, Ning W, et al. Expression of inflammasomes NLRP1, NLRP3 and AIM2 in different pathologic classification of lupus nephritis. Clin Exp Rheumatol. 2020; 38(4): 680–690, indexed in Pubmed: 31694740.
11. Honarpisheh M, Desai J, Marschner JA, et al. Regulated necrosis-related molecule mRNA expression in humans and mice and in murine acute tissue injury and systemic autoimmunity leading to progressive organ damage, and progressive fibrosis. Biosci Rep. 2016; 36(6): doi: 10.1042/BSR20160336, indexed in Pubmed: 27811014.
12. Bonomini F, Dos Santos M, Veronese FV, et al. NLRP3 Inflammasome Modulation by Melatonin Supplementation in Chronic Pristane-Induced Lupus Nephritis. Int J Mol Sci. 2019; 20(14), doi: 10.3390/ijms20143466, indexed in Pubmed: 31311094.
13. Fu R, Guo C, Wang S, et al. Podocyte activation of NLRP3 inflammasomes contributes to the development of proteinuria in lupus nephritis. Arthritis Rheumatol. 2017; 69(8): 1636–1646, doi: 10.1002/art.40155, indexed in Pubmed: 28544564.
14. Fu R, Xia Y, Li M, et al. Pim-1 as a therapeutic target in lupus nephritis. Arthritis Rheumatol. 2019; 71(8): 1308–1318, doi: 10.1002/art.40863, indexed in Pubmed: 30791224.
15. Wu CY, Hua KF, Chu CL, et al. Tris DBA ameliorates accelerated and severe lupus nephritis in mice by activating regulatory t cells and autophagy and inhibiting the NLRP3 inflammasome. J Immunol. 2020; 204(6): 1448–1461, doi: 10.4049/jimmunol.1801610, indexed in Pubmed: 32060137.
16. Zhao J, Zhang H, Huang Y, et al. Bay11-7082 attenuates murine lupus nephritis via inhibiting NLRP3 inflammasome and NF-κB activation. Int Immunopharmacol. 2013; 17(1):

116–122, doi: 10.1016/j.intimp.2013.05.027, indexed in Pubmed: 23770281.

17. Li Q, Verma IM. NF-kappaB regulation in the immune system. Nat Rev Immunol. 2002; 2(10): 725–734, doi: 10.1038/nri910, indexed in Pubmed: 12360211.

18. Williams LM, Gilmore TD. Looking down on NF-κB. Mol Cell Biol. 2020; 40(15), doi: 10.1128/MCB.00104-20, indexed in Pubmed: 32393609.

19. Zheng L, Sinniah R, Hsu SIH. Pathogenic role of NF-kappaB activation in tubulointerstitial inflammatory lesions in human lupus nephritis. J Histochem Cytochem. 2008; 56(5): 517–529, doi: 10.1369/jhc.7A7368.2008, indexed in Pubmed: 18285351.

20. Li X, Wang M, Hong H, et al. Sophocarpine attenuates murine lupus nephritis via inhibiting NLRP3 inflammasome and NF-κB activation. Immunol Res. 2018; 66(4): 521–527, doi: 10.1007/s12026-018-9012-9, indexed in Pubmed: 30047025.

21. Su B, Ye H, You X, et al. Icariin alleviates murine lupus nephritis via inhibiting NF-κB activation pathway and NLRP3 inflammasome. Life Sci. 2018; 208: 26–32, doi: 10.1016/j.lfs.2018.07.009, indexed in Pubmed: 30146016.

22. Tao X, Yin L, Xu L, et al. Dioscin: A diverse acting natural compound with therapeutic potential in metabolic diseases, cancer, inflammation and infections. Pharmacol Res. 2018; 137: 259–269, doi: 10.1016/j.phrs.2018.09.022, indexed in Pubmed: 30315966.

23. Qi M, Zheng L, Qi Y, et al. Dioscin attenuates renal ischemia/reperfusion injury by inhibiting the TLR4/MyD88 signaling pathway via up-regulation of HSP70. Pharmacol Res. 2015; 100: 341–352, doi: 10.1016/j.phrs.2015.08.025, indexed in Pubmed: 26348276.

24. Wang Y, Liu P, Ma G, et al. Mechanism of dioscin ameliorating renal fibrosis through NFκB signaling pathwaymediated inflammatory response. Mol Med Rep. 2023; 27(4), doi: 10.3892/mmr.2023.12980, indexed in Pubmed: 36960871.

25. Cai S, Chen J, Li Y. Dioscin protects against diabetic nephropathy by inhibiting renal inflammation through TLR4/NF-κB pathway in mice. Immunobiology. 2020; 225(3): 151941, doi: 10.1016/j.imbio.2020.151941, indexed in Pubmed: 32359778.

26. Zhang P, Lei X, Ou L, et al. Dioscin ameliorates silica-aggravated systemic lupus erythematosus via suppressing apoptosis and improving LC3-associated phagocytosis in MRL/lpr mice. Int Immunopharmacol. 2023; 116: 109814, doi: 10.1016/j.intimp.2023.109814, indexed in Pubmed: 36773568.

27. Jiang X, Ding X, Wei J, et al. Dioscin alleviates periodontitis by inhibiting NLRP3 inflammasome activation via regulation of k homeostasis and mitochondrial function. Int J Biol Sci. 2024; 20(4): 1375–1388, doi: 10.7150/ijbs.85851, indexed in Pubmed: 38385066.

28. Liang CL, Lu W, Qiu F, et al. Paeoniflorin ameliorates murine lupus nephritis by increasing CD4Foxp3 Treg cells via enhancing mTNFα-TNFR2 pathway. Biochem Pharmacol. 2021; 185: 114434, doi: 10.1016/j.bcp.2021.114434, indexed in Pubmed: 33513343.

29. Qi Q, Li H, Lin ZM, et al. (5R)-5-hydroxytriptolide ameliorates anti-glomerular basement membrane glomerulonephritis in NZW mice by regulating Fcγ receptor signaling. Acta Pharmacol Sin. 2018; 39(1): 107–116, doi: 10.1038/aps.2017.88, indexed in Pubmed: 28880016.

30. Jia Y, He J, Wang L, et al. Dapagliflozin aggravates renal injury via promoting gluconeogenesis in db/db mice. Cell Physiol Biochem. 2018; 45(5): 1747–1758, doi: 10.1159/000487783, indexed in Pubmed: 29495021.

31. Kökény G, Fang L, Révész C, et al. The Effect of Combined Treatment with the (Pro)Renin Receptor Blocker HRP and Quinapril in Type 1 Diabetic Rats. Kidney Blood Press Res. 2017; 42(1): 109–122, doi: 10.1159/000471915, indexed in Pubmed: 28359068.

32. Livak KJ, Schmittgen TD. Analysis of relative gene expression data using real-time quantitative PCR and the 2(-Delta Delta C(T)) Method. Methods. 2001; 25(4): 402–408, doi: 10.1006/meth.2001.1262, indexed in Pubmed: 11846609.

33. Tektonidou MG, Dasgupta A, Ward MM. Risk of end-stage renal disease in patients with lupus nephritis, 1971–2015: a systematic review and Bayesian meta-analysis. Arthritis Rheumatol. 2016; 68(6): 1432–1441, doi: 10.1002/art.39594, indexed in Pubmed: 26815601.

34. Qiao Y, Xu L, Tao X, et al. Protective effects of dioscin against fructose-induced renal damage via adjusting Sirt3-mediated oxidative stress, fibrosis, lipid metabolism and inflammation. Toxicol Lett. 2018; 284: 37–45, doi: 10.1016/j.toxlet.2017.11.031, indexed in Pubmed: 29197622.

35. Tsokos GC. Systemic lupus erythematosus. N Engl J Med. 2011; 365(22): 2110–2121, doi: 10.1056/NEJMra1100359, indexed in Pubmed: 22129255.

36. Richoz N, Tuong ZK, Loudon KW, et al. Distinct pathogenic roles for resident and monocyte-derived macrophages in lupus nephritis. JCI Insight. 2022; 7(21), doi: 10.1172/jci.insight.159751, indexed in Pubmed: 36345939.

37. Ma C, Xia Yu, Yang Q, et al. The contribution of macrophages to systemic lupus erythematosus. Clin Immunol. 2019; 207: 1–9, doi: 10.1016/j.clim.2019.06.009, indexed in Pubmed: 31255802.

38. Kurts C, Panzer U, Anders HJ, et al. The immune system and kidney disease: basic concepts and clinical implications. Nat Rev Immunol. 2013; 13(10): 738–753, doi: 10.1038/nri3523, indexed in Pubmed: 24037418.

39. Lin L, Shen J, Wu X, et al. Dioscin mediated IgA nephropathy alleviation by inhibiting B cell activation in vivo and decreasing galactose-deficient IgA1 production in vitro. J Vis Exp. 2023(200), doi: 10.3791/65719, indexed in Pubmed: 37902367.

40. Wu MM, Wang QM, Huang BY, et al. Dioscin ameliorates murine ulcerative colitis by regulating macrophage polarization. Pharmacol Res. 2021; 172: 105796, doi: 10.1016/j.phrs.2021.105796, indexed in Pubmed: 34343656.

41. Shi L, Zhang P, Jin R, et al. Dioscin ameliorates inflammatory bowel disease by up-regulating miR-125a-5p to regulate macrophage polarization. J Clin Lab Anal. 2022; 36(6): e24455, doi: 10.1002/jcla.24455, indexed in Pubmed: 35524480.

42. Li C, Lu Y, Du S, et al. Dioscin exerts protective effects against crystalline silica-induced pulmonary fibrosis in mice. Theranostics. 2017; 7(17): 4255–4275, doi: 10.7150/thno.20270, indexed in Pubmed: 29158824.

43. Kahlenberg JM, Carmona-Rivera C, Smith CK, et al. Neutrophil extracellular trap-associated protein activation of the NLRP3 inflammasome is enhanced in lupus macrophages. J Immunol. 2013; 190(3): 1217–1226, doi: 10.4049/jimmunol.1202388, indexed in Pubmed: 23267025.

44. Liu X, Bao C, Hu D. Elevated interleukin-18 and skewed Th1:Th2 immune response in lupus nephritis. Rheumatol Int. 2012; 32(1): 223–229, doi: 10.1007/s00296-010-1609-9, indexed in Pubmed: 20963419.

45. Ding Yi, Chen Q. The NF-κB Pathway: a Focus on Inflammatory Responses in Spinal Cord Injury. Mol Neurobiol. 2023; 60(9): 5292–5308, doi: 10.1007/s12035-023-03411-x, indexed in Pubmed: 37286724.

46. Han J, Shi G, Li W, et al. Preventive effect of dioscin against monosodium urate-mediated gouty arthritis through inhibiting inflammasome NLRP3 and TLR4/NF-κB signaling pathway activation: an in vivo and in vitro study. J Nat Med. 2021;

75(1): 37–47, doi: 10.1007/s11418-020-01440-7, indexed in Pubmed: 32761488.

47. Ran X, Yan Z, Yang Y, et al. Dioscin improves pyroptosis in LPS-induced mice mastitis by activating AMPK/Nrf2 and inhibiting the NF-κB signaling pathway. Oxid Med Cell Longev. 2020; 2020: 8845521, doi: 10.1155/2020/8845521, indexed in Pubmed: 33488936.

48. Cai J, Liu J, Fan P, et al. Dioscin prevents DSS-induced colitis in mice with enhancing intestinal barrier function and reducing colon inflammation. Int Immunopharmacol. 2021; 99: 108015, doi: 10.1016/j.intimp.2021.108015, indexed in Pubmed: 34339962.

49. Lu Z, Yao Y, Wang J, et al. Dioscin ameliorates diabetes cognitive dysfunction via adjusting P2X7R/NLRP3 signal. Int Immunopharmacol. 2021; 101(Pt B): 108314, doi: 10.1016/j.intimp.2021.108314, indexed in Pubmed: 34785142.

50. Qi M, Yin L, Xu L, et al. Dioscin alleviates lipopolysaccharide-induced inflammatory kidney injury via the microRNA let-7i/TLR4/MyD88 signaling pathway. Pharmacol Res. 2016; 111: 509–522, doi: 10.1016/j.phrs.2016.07.016, indexed in Pubmed: 27431331.

51. Perry D, Sang A, Yin Y, et al. Murine models of systemic lupus erythematosus. J Biomed Biotechnol. 2011; 2011: 271694, doi: 10.1155/2011/271694, indexed in Pubmed: 21403825.